ABSTRACT

COMPUTATIONAL STUDIES OF VISCOELASTIC MULTIPHASE FLOWS

by

Shriram B. Pillapakkam

A finite element code based on the level set method is developed for performing two and three dimensional direct numerical simulations (DNS) of viscoelastic two-phase flow problems. The Oldroyd-B constitutive equation is used to model the viscoelastic liquid. The code is used to study transient and steady state shapes of Newtonian and viscoelastic drops in simple shear and buoyancy driven flows. The roles of the governing dimensionless parameters: Capillary number (Ca), Deborah Number (De) and the polymer concentration parameter *c,* in determining deformation of drops and bubbles, are also analyzed.

The numerical code permits us to vary Ca, De and *c* independently, which is difficult to achieve experimentally. This capability is used to isolate the roles of these parameters on the nature of viscoelastic stress near the drop surface and their effect on drop deformation. Results for simple shear flows indicate that when the drop phase is Newtonian and the matrix phase viscoelastic, the viscoelastic stresses pull the ends of the drop near the tips of the major axis and near the tips of the minor axes they are tangential, and thus have the net effect of increasing drop deformation. Viscoelastic stresses have the opposite effect when the drop phase is viscoelastic and the matrix phase is Newtonian. Additionally, due to the extensional nature of viscoelastic stresses, drops sheared by

viscoelastic fluids develop pointed ends, a phenomenon observed experimentally and popularly known as tip-streaming.

For buoyancy driven bubbles rising in quiescent viscoelastic fluids, simulations show that the rise velocity oscillates before reaching a steady value. The shape of the bubble, the magnitude of velocity overshoot and the amount of damping depend mainly on c and the bubble radius. Simulations show that there is a critical bubble volume range in which there is a sharp increase in the terminal velocity with increasing bubble volume similar to the behavior observed in experiments. An explanation for this phenomenon is offered based on the transient oscillations and shape change.

The structure of the wake of a bubble rising in a Newtonian fluid is strikingly different from that of a bubble rising in a viscoelastic fluid. In addition to the two recirculation zones at the equator of the bubble rising in a Newtonian fluid, two more recirculation zones exist in the wake of a bubble rising in viscoelastic fluids which influence the shape of a rising bubble. Also, the direction of motion of the fluid a short distance below the trailing edge of a bubble rising in a viscoelastic fluid is in the opposite direction to the direction of motion of the bubble. The wake is 'negative' in the sense that the direction of fluid velocity behind the bubble is the opposite of that for a Newtonian fluid.

COMPUTATIONAL STUDIES OF VISCOELASTIC MULTIPHASE FLOWS

by

Shriram B. Pillapakkam

A Dissertation
Submitted to the Faculty of
New Jersey Institute of Technology
in Partial Fulfillment of the Requirements for the Degree of
Doctor of Philosophy in Mechanical Engineering

Department of Mechanical Engineering

January 2005

APPROVAL PAGE

COMPUTATIONAL STUDIES OF VISCOELASTIC MULTIPHASE FLOWS

Shriram B. Pillapakkam

Dr. Pushpendra Singh, Thesis Advisor — Date
Associate Professor, Department of Mechanical Engineering, NJIT

Dr. Nadine Aubry, Committee Member — Date
Distinguished Professor, Department of Mechanical Engineering, NJIT

Dr. Anthony Rosato, Committee Member — Date
Professor, Department of Mechanical Engineering, NJIT

Dr. Denis L. Blackmore, Committee Member — Date
Professor, Department of Mathematical Sciences, NJIT

Dr. I. Joga Rao, Committee Member — Date
Assistant Professor, Department of Mechanical Engineering, NJIT

BIOGRAPHICAL SKETCH

Author: Shriram B. Pillapakkam

Degree: Doctor of Philosophy

Date: January 2005

Undergraduate and Graduate Education:

- Doctor of Philosophy in Mechanical Engineering,
  New Jersey Institute of Technology, Newark, NJ, 2005

- Bachelor of Science in Mechanical Engineering,
  Manipal Institute of Technology, Manipal, India, 1997

Major: Mechanical Engineering

Publications:

1. S. B. Pillapakkam, D. Blackmore and P. Singh, Transient and steady state motion of a Bubble rising in a viscoelastic fluid, manuscript in preparation.
2. Arun Kadakasham, S. B. Pillapakkam and P. Singh, Permeability of periodic arrays of sphere, Accepted for publication in Mechanics Research Communications, 2004
3. S. B. Pillapakkam and P. Singh, Negative wake and velocity of a bubble rising in a viscoelastic fluid American Society of Mechanical Engineers 2003, Washington, D.C.
4. S. B. Pillapakkam and P. Singh, Transient and steady state analysis for a Bubble rising in a viscoelastic fluid, Society of Rheology, 2003, Pittsburgh, PA.
5. S. B. Pillapakkam, P. Singh, A Level-Set method for computing solutions to two phase viscoelastic flows, Journal of Computational physics 174, 2001, Pages 552-57.
6. S. B. Pillapakkam and P. Singh, Numerical Simulations of drops and bubbles in three-dimensional viscoelastic flows, Society of Rheology, 2001, Washington, D.C.
7. S. B. Pillapakkam and P. Singh, Advances in numerical simulations of dynamics of drops and bubbles in viscoelastic flows, American Society of Mechanical Engineers 2000, New Orleans, LA.
8. P. Singh, S.B. Pillapakkam and A. Narh, Direct numerical simulations of drops and bubbles in viscoelastic shear and pressure driven flows, Society of petroleum Engineers, 1999, Annual Technical Conference and Exhibition, Houston, Texas.

9. S. B. Pillapakkam and P. Singh, Dynamic of drops and bubbles in viscoelastic flows, American Society of Mechanical Engineers, 1999, Nashville, TN.

Conference Presentations:

1. S.B. Pillapakkam, D. Blackmore, Singh, P., Instabilities of a bubble rising in viscoelastic fluid, Frontiers in Applied and Computational Mathematics, 2004, Newark, NJ.
2. S. B. Pillapakkam and P. Singh, Transient and steady state analysis for a Bubble rising in a viscoelastic fluid, Society of Rheology, 2003, Pittsburgh, PA.
3. S. B. Pillapakkam and P. Singh, Negative wake and velocity of a bubble rising in a viscoelastic fluid, American Society of Mechanical Engineers 2003, Washington, D.C.
4. S. B. Pillapakkam and P. Singh, Direct numerical simulation of drops in three dimensional viscoelastic shear flows, American Society of Mechanical Engineers 2000, New York, NY.
5. S. B. Pillapakkam and P. Singh, Dynamic of drops and bubbles in viscoelastic flows, American Society of Mechanical Engineers, 1999, Nashville, TN.

Honors and Awards

1. Society of Rheology, 2003, Pittsburgh, PA, Student Fellowship award for original contribution by graduate student.
2. American Society of Mechanical Engineers, 1999, Nashville, TN., Young Engineer award for best research work by a first year graduate student.

To

Linda Marie Montgomery, Richard A. Bonifazi

and

my beloved quadrupeds

Button, Debbie and Maggie

ACKNOWLEDGEMENT

I would like to express my thanks and appreciation to Dr. Pushpendra Singh, Associate Professor, Department of Mechanical Engineering at NJIT, for all his help over the duration of my graduate program.

I would like express my gratitude to Dr. Denis Blackmore, Professor at the Department of Mathematical Sciences at NJIT for his contribution towards my dissertation and for setting very high standards of didactic excellence.

I also extend my thanks to Dr. Nadine Aubry, Distinguished Professor and Chair of the Department of Mechanical Engineering, Dr. Anthony D. Rosato, Professor, Department of Mechanical Engineering and Dr. I. Joga Rao, Assistant Professor, Department of Mechanical Engineering for their contribution towards my education and research.

This research was supported by the National Science Foundation KDI Grand Challenge grant (NSF/CTS-98-73236).

TABLE OF CONTENTS

TABLE OF CONTENTS
(Continued)

Chapter **Page**

TABLE OF CONTENTS
(Continued)

Chapter **Page**

CHAPTER 1

INTRODUCTION

The aim of this work is to develop a stable and efficient numerical method for the direct numerical simulation (DNS) of viscoelastic multiphase flows and to use it to investigate the following problems: Analysis of deformation of neutrally buoyant drops in shear flows and the transient behavior of bubbles rising in viscoelastic fluids due to buoyancy and to examine the reason for the discontinuity observed in the velocity-volume plot.

Before proceeding with the details of these two problems, it behooves me to introduce the reader to the key fundamental properties of viscoelastic liquids. Broadly speaking, matter can be categorized into elastic solids, viscous fluids and everything in between. For linear elastic solids, the stress is related to the strain via a constant of proportionality known as the modulus of elasticity. For viscous Newtonian liquids, the stress is related to the rate of change of strain through a constant of proportionality known as dynamic viscosity. In the in-between category, lies a class of matter for which viscosity changes with applied shear force, known as non-Newtonian fluids. We encounter such fluids in our everyday life; honey, mayonnaise and ketchup are typical examples. There are many subcategories within the non-Newtonian category such as power law fluids, plastic solids, viscoelastic fluids etc. Viscoelastic fluids exhibit both elastic characteristics of solids as well as viscous properties of fluids. Polymeric liquids and solutions containing long chained molecules are classical examples of viscoelastic liquids.

Before introducing the properties of non-Newtonian fluids, it seems appropriate at this stage to review the governing equations, the mass and momentum conservation of fluids and to understand the role of viscoelastic stresses which, as will be discussed later, alter the velocity field from that for a Newtonian liquid.

The mass conservation law states that mass can neither be created nor destroyed, and hence the total mass of fluid within an arbitrary volume V increases only due to net influx across the surface S

$$\frac{\partial}{\partial t}\int_V \rho \, dV = \int_S (\mathbf{n}\cdot\rho\mathbf{v})\, dS \qquad (1.1)$$

Rate of change of mass of fluid in V = Rate of change of mass across the surface S

Here t is the time, ρ is the density and $\mathbf{v}$ is the velocity with which the fluid is crossing the surface of an arbitrary volume V.

According to the law of momentum conservation, or Newton's second law applied to an arbitrary volume V, the total momentum of the fluid within V will increase because of a net influx of momentum across the bounding surface–both by bulk flow and by molecular motions–and because of body forces acting on the fluid:

$$\frac{\partial}{\partial t}\int_V \rho\mathbf{v}\, dV = -\int_S [\mathbf{n}\cdot\rho\mathbf{v}\mathbf{v}]\, dS - \int_S [\mathbf{n}\cdot\boldsymbol{\sigma}]\, dS + \int_V \rho\mathbf{g}\, dV \qquad (1.2)$$

Rate of change of momentum of fluid within V	Rate of change of momentum due to convection across S	Rate of change of momentum due to surface forces acting on S	Rate of change of momentum due to body force

The integral $\int_S [\mathbf{n}\cdot\boldsymbol{\sigma}]dS$ in the above equation can be interpreted as the force of the fluid outside V acting on the fluid inside V across S, where $\boldsymbol{\sigma}$ is the the stress tensor. There is a wealth of information in the term $\boldsymbol{\sigma}$, and one of the greatest challenges in the field of non-Newtonian fluid dynamics is to come up with model that gives the closest approximations to the relationship between stress and strain for the fluid under examination. The notion of a relation between stress and strain will be explored in detail in Chapter 2 while discussing constitutive equations.

With this cursory overview of equations governing fluid flow, we are sufficiently equipped to explore some properties that make non-Newtonian fluids so strikingly different from Newtonian fluids through many illustrative examples that bring out these properties.

1.1 Shear Dependent Viscosity

One of the key features that distinguish a non-Newtonian fluid from a Newtonian one is that the viscosity of Newtonian fluid does not change upon external loading while the viscosity of a non-Newtonian fluid varies upon shearing.

For a Newtonian incompressible fluid in simple steady shear flow, the term $\boldsymbol{\sigma}$ in equation (1.2) is, $\boldsymbol{\sigma} = -pI+\boldsymbol{\tau} = -pI+ 2\mu\mathbf{D}$, where $\boldsymbol{\tau} = 2\mu\mathbf{D}$ is the simple constitutive equation for such fluids where $\mathbf{D}$ is the rate of strain tensor, or the symmetric part of the velocity gradient tensor, $\mathbf{D}=\frac{\nabla\mathbf{v}+(\nabla\mathbf{v})^T}{2}$. The viscosity μ for Newtonian fluids is defined by Newton's law of viscosity, $\tau_{yx} = -\mu\frac{dv_x}{dy}$. For a non-Newtonian

fluid, the stress $\tau_{yx} = -\eta(\dot{\gamma})\dot{\gamma}_{yx}$ and the viscosity η which depends on the shear rate $\dot{\gamma}$, is called non-Newtonian viscosity or shear-rate dependent viscosity.

The viscosity of non-Newtonian fluids either increases or decreases with shear rates. Fluids for which viscosity increases with shear rate are called shear thickening fluids and for those for which viscosity decreases with shear rate are called shear thinning fluids as illustrated in a Figure 1.1.

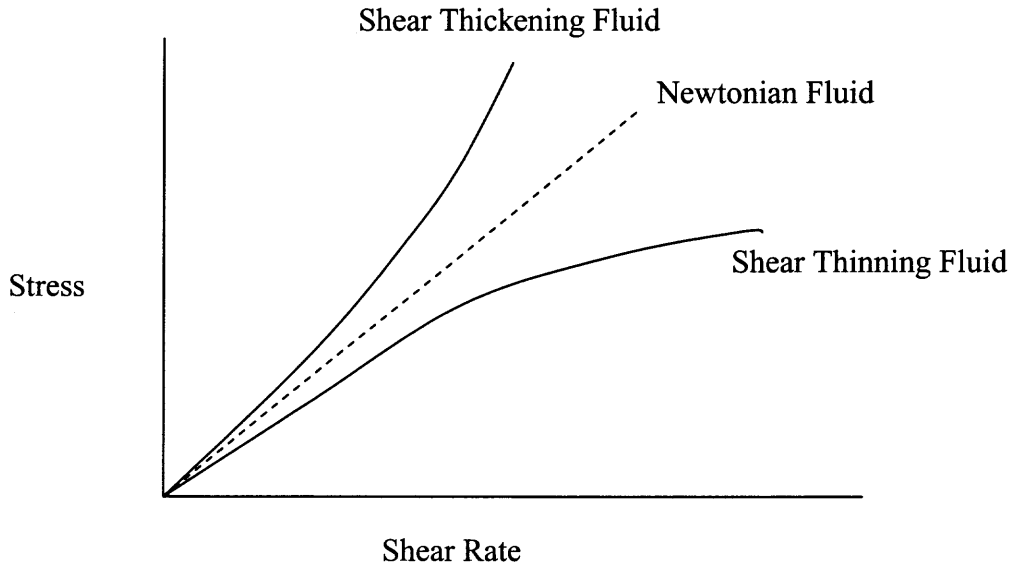

Figure 1.1 Stress vs. Shear Rate for non-Newtonian shear thickening and shear thinning fluid. The dashed line is the linear stress-shear rate relationship for a Newtonian fluid.

1.2 Normal Stress Difference

Consider the simple shear flow of a Newtonian fluid, with the components of velocity given by:

$$u = \frac{U}{h}y, \quad v = w = 0, \tag{1.3}$$

where U is the velocity of the upper plate and h is the height of fluid below the plate (See Figure 1.2). The axial components of the stress tensor are then:

$$\sigma_{xx} = -p + \mu \partial u/\partial x = -p$$

$$\sigma_{yy} = -p + \mu \partial v/\partial y = -p \qquad (1.4)$$

$$\sigma_{zz} = -p + \mu \partial w/\partial z = -p$$

Therefore for a Newtonian fluid the normal stress difference coefficients, $N_1 = \sigma_{xx} - \sigma_{yy} = 0$ and $N_2 = \sigma_{yy} - \sigma_{zz} = 0$. But, experiments show that non-Newtonian fluids have non-zero normal stress difference coefficients. $\sigma_{xx} - \sigma_{yy} = N_1(\dot{\gamma})$ and $\sigma_{yy} - \sigma_{zz} = N_2(\dot{\gamma})$. Non-zero normal stress coefficients indicate that non-Newtonian fluids exhibit longitudinal extensional stress along streamlines.

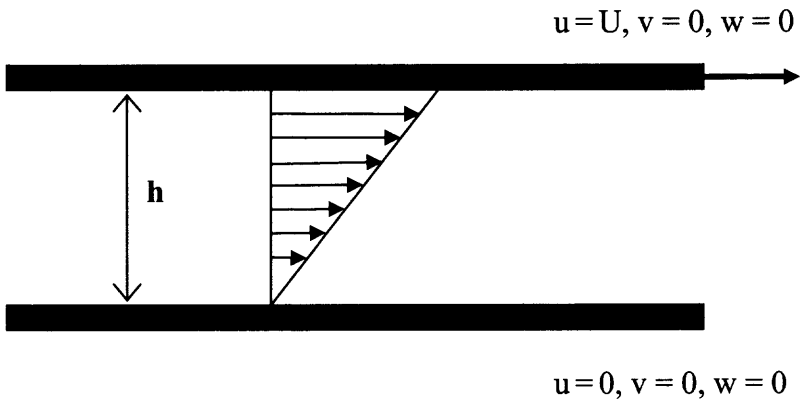

Figure 1.2 An illustrative sketch of shearing flow between two parallel plates. The top plate is moving at velocity U (u = U, v = 0, w = 0) and the bottom plate is stationary.

The normal stress difference is responsible for several striking differences between the behavior of viscoelastic and Newtonian liquids. One such example is the rod-climbing experiment (See Figure 1.3). When a rod is rotated in a beaker containing a Newtonian liquid the liquid is pushed outward due to centrifugal force and the liquid level near the rod falls. In a viscoelastic fluid on the other hand the fluid is drawn closer to the rod and even overcomes gravitational force as the fluid level near the rod rises. The fluid climbs the rod because of non-zero normal stress difference coeffecients. "*In the rod-climbing experiment, the streamlines are in closed circles and the extra tension along these lines "strangulates" the fluid and forces it inwards against the centrifugal force and upwards against the gravitational force.*" [Bird et al. (1987)]

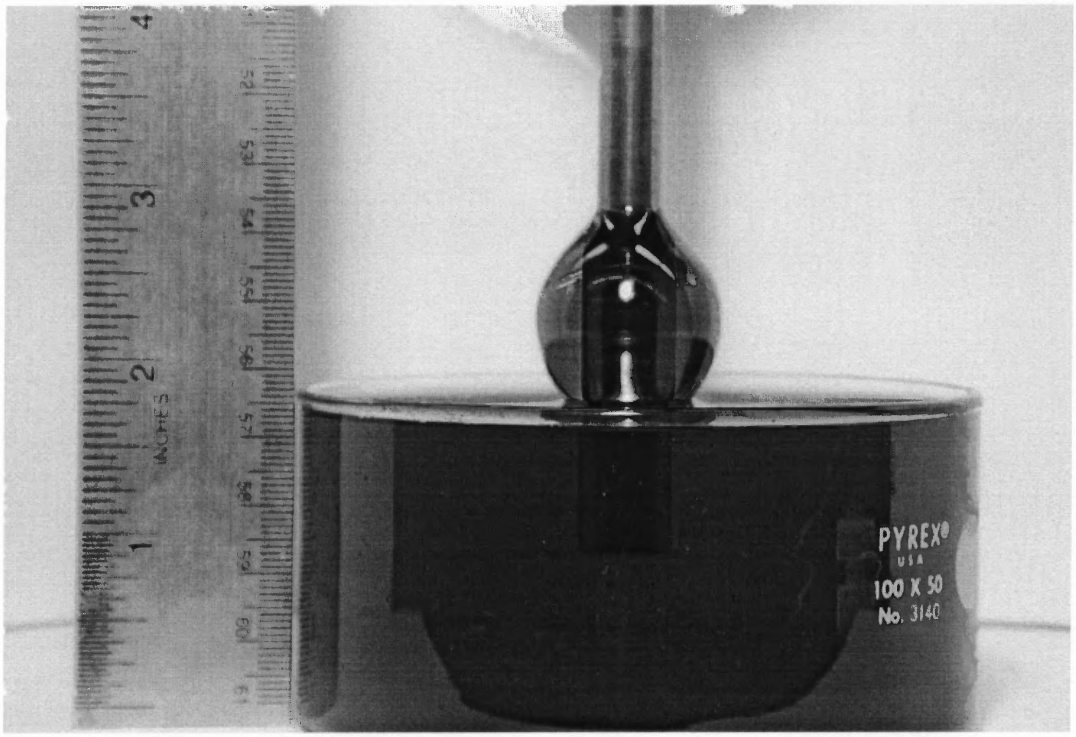

Figure 1.3 Rod-climbing experiment–when the rod is rotated in a non-Newtonian fluid, the fluid climbs up the rod. Such behavior is unique to viscoelastic fluid. Image taken by Dr. J Bico, Mr. R. Welsh and Prof. G. H. McKinley, MIT Non-Newtonian Fluids Laboratory.

1.3 Fading Memory Effect

Another behavioral aspect of non-Newtonian fluids which fascinates a wide-eyed kid as much as it does a rational adult is the recoil effect: Why the last bit of maple syrup touches the pancake and retracts back to the spoon in a hurry? This is because non-Newtonian fluids, filament of syrup in this case, has "fading memory effect," an ability to remember its past state. It is called "fading memory," because it does not always recover fully to its original condition before it was set to deform. This idea of fluid having memory leads us to an important property of a viscoelastic fluid called the relaxation time, which will be discussed in detail in Chapter 2.

In summary, the features that distinguish a Newtonian fluid from a non-Newtonian fluid are:

- The viscosity of a Newtonian fluid depends on temperature and pressure, but is independent of the shear rate. The viscosity of a non-Newtonian fluid is shear-dependent. For certain fluids, viscosity decreases with an increase in shear rate, commonly referred to as shear-thinning fluid. A fluid whose viscosity increases with increasing shear rate is called shear-thickening or dilatant.

- In simple shear flow, Non-Newtonian fluids have non-zero normal stress difference coefficients. Newtonian fluids have zero first and second normal stress difference coeffocients.

- Non-Newtonian fluids also exhibit extensional viscosity.

- An important property of a non-Newtonian fluid is its ability to partially remember its past state of strain, a property better known as the fading memory effect. The stress at a present time t depends the rate of strain at time t as well as the rate of strain at all past times t^1, with a weighting factor (the relaxation modulus) that decays exponentially as one goes back in time. This leads us to concept of relaxation time of a material that quantifies the delayed response of a viscoelastic molecule to externally applied force. Polymer solutions typically have relaxation time of the order of 10^{-2} – 10^2 seconds, while the relaxation time for a Newtonian fluids ~ 0 (The relaxation time for water is 10^{-13} seconds).

This brief introduction to the nature and properties of non-Newtonian fluids sets up the stage to present the two problems around which this dissertation is centered--the shape of a neutrally buoyant drop in simple shear flows and the shape and velocity of a buoyant bubble rising in a viscoelastic fluid.

The shape of a neutrally buoyant drop in a shear flow of a Newtonian fluid is determined by the balance of forces at the interface, between the flow-induced viscous stresses which deform the drop and the interfacial tension which resists deformation. This equilibrium is however multifaceted when either phase is viscoelastic and the mechanism of shape change is quite complicated.

For many years, analysis of the behavior of drops immiscible with the surrounding fluid in simple shear flows has been used as a starting point to understand the effects of many parameters that influence the shape of a fluid-fluid interface. Until the 1970s, research was predominantly focused on the study of Newtonian fluids, governed by Navier-Stokes equations. In the 1980s, and more so in the last decade, the analysis of deformation of drops involving viscoelastic fluids has been used to understand the role of viscoelasticity, such as on tip streaming.

The problem of a bubble rising due to buoyancy in a column of viscoelastic fluid is very interesting for several reasons. A casual investigation of a shampoo bottle turned upside down will reveal that the air bubble rising in the shampoo (a viscoelastic liquid) is initially spherical and changes shape to resemble an inverted tear drop with a cusp like trailing end. If the shampoo bottle were to be rotated 90^{o}, one can notice that the shape of the trailing end of the bubble is markedly different and resembles a knife edge. The above is just one of the peculiarities of this problem where a perfectly symmetrical bubble looses its symmetry. The other aspect of the problem that makes this problem quite interesting is that when bubbles of different volumes are allowed to rise in a column filled with a viscoelastic fluid and their terminal velocities are recorded and plotted against their volume, a striking discontinuity is seen at a critical volume, at which the velocity suddenly increases by a large amount. Another facet to an already interesting problem is the direction of the velocity vectors in the wake of the bubble. Contrary to what is seen for a bubble rising in a Newtonian liquid such as water, the velocity vectors in the wake of the bubble are in a direction opposite to the direction of motion of the bubble. All of the above mentioned aspects make this problem a very interesting study,

both from a point of view of satisfying human inquisitiveness as well as thorough scientific investigation.

It is not a simple task to numerically model deformation of a drop when either fluid phase is viscoelastic, given the existence of jump in fluid properties such as density and viscosity across the interface that poses severe mathematical restrictions. Complications also arise because the interface position is a priori unknown and must be tracked as the drop deforms with time. The direct numerical simulation (DNS) technique for solving problems in fluid dynamics has made rapid progress in recent years and has become increasingly sophisticated and reliable. It is invaluable in the context of analyzing viscoelastic flows since it is difficult to extract dynamical data through experimental observations. Direct simulations give us definitive insight into transient aspects of viscoelastic stresses which are difficult to measure experimentally.

There is substantial interest in modeling viscoelastic fluids because processing flows involving viscoelastic fluids are very commonly encountered in the polymer industry. For example, to model operations such as emulsification, which involves dispersing droplets of one medium in another, we must account for the stretching of droplets, as well as stresses in the viscoelastic fluid in the immediate vicinity of each droplet. Additionally, complexity rises due to the lack of symmetry, the unsteady nature of the problem and the presence of stagnation points in flow near where the flow is highly extensional and the polymer molecules highly stretched. The first and the logical step in modeling a problem as complex as this, is to model the effect of viscoelasticity on a single droplet in deforming flows. A comprehensive understanding of the rheology of an isolated drop will help in generalizing the effect of many such drops in processing flows.

The goal of my work therefore is to develop a stable and efficient numerical method for simulating multi-phase viscoelastic flows involving a single drop. This dissertation is organized as follows: Chapter 2 provides a quick overview of the deforming flows and fundamental concepts of non-Newtonian fluid dynamics. The theory behind deformation of drops, shape and velocity of bubbles, including literature review is presented in Chapter 3. The finite element discritization, numerical scheme and interface tracking method are discussed in Chapter 4. In Chapters 5 and 6 the results of numerical simulations of the drop deformation problem and buoyant bubble problem will be discussed, which will be followed by the concluding section.

At many instances in this document, computational results are compared both quantitatively with experimental results and published numerical data. However, since the choice of constitutive model is ad hoc and the relation between experimental parameters and those of the model is not precise, quantitative comparison is not possible.

CHAPTER 2

PROBLEM DESCRIPTION AND GOVERNING EQUATIONS

2.1 Drop Deformation in Simple Shear Flow

2.1.1 Problem Description

The velocity field in a simple shear flow is given by

$$u_x = \gamma_{yx} y,\ u_y = 0, u_z = 0 \tag{2.1}$$

where γ_{yx} is the shear rate or strength of the shear flow. Simple steady shear flow can be generated experimentally by moving the upper plate of a parallel plate apparatus at a constant velocity.

A simple shear flow has equal components of shear and vorticity. The velocity gradient tensor $\nabla\mathbf{u}$, the rate of strain tensor $\mathbf{D}$, and vorticity tensor $\boldsymbol{\Omega}$ for simple shear flow are as indicated below:

$$\nabla\mathbf{u} = G\begin{bmatrix} 0 & 0 & 0 \\ 1 & 0 & 0 \\ 0 & 0 & 0 \end{bmatrix};\ \mathbf{D} = G\begin{bmatrix} 0 & 1 & 0 \\ 1 & 0 & 0 \\ 0 & 0 & 0 \end{bmatrix};\ \boldsymbol{\Omega} = G\begin{bmatrix} 0 & -1 & 0 \\ 1 & 0 & 0 \\ 0 & 0 & 0 \end{bmatrix}$$

where $G = \gamma_{yx}$ is the shear rate. In simulations, simple shear flow is generated by moving a pair of opposite walls of the domain in opposite direction as shown in Figure 2.1. The velocity on the remaining side walls varies linearly, as shown in Figure 2.1.

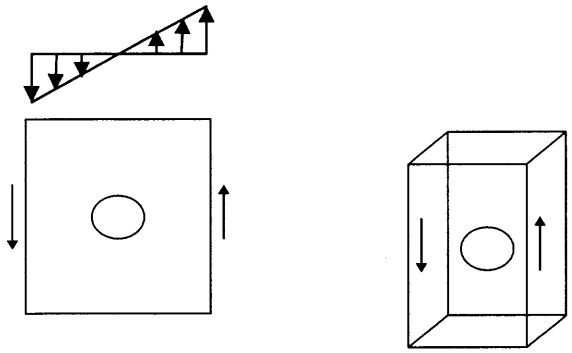

Figure 2.1 A two-dimensional and three-dimensional depiction of a drop subjected to simple shear flow. Moving the opposite walls of the domain generates shear flow in each case.

The parameters affecting deformation are the drop radius a, the interfacial tension γ, G, and the viscosity ratio $\lambda = \frac{\eta_L}{\eta_d}$, where η_L is the viscosity of the matrix fluid (fluid outside the drop) and η_d is the viscosity of the fluid inside the drop. The parameters G, η_L, γ and a can be combined to form a dimensionless group called the capillary number $Ca = G\eta_L a/\gamma$. The Deborah number, a dimensionless measure of viscoelastic stresses is defined as $De = \lambda_r G$, where λ_r is the relaxation time

When the densities of the drop and matrix fluid are equal, in the absence of imposed flow, the drop would remain spherical due to the interfacial tension. When a shear flow is imposed, the equilibrium is altered in the following ways:

1. If both phases are Newtonian, the imposed velocity field gives rise to viscous stresses that deform the drop while the interfacial force resists deformation. The final shape of the drop is a balance between these two effects.
2. In the event of either phase being viscoelastic, the viscoelastic stresses affect the drop shape in two ways

a) The viscoelastic contribution at the interface affects the normal stress balance at the interface and consequently the shape of the drop.
b) The viscoelastic stresses in the vicinity of the interface alter the strain rate and consequently the stresses on the interface.

Upon imposing flow, the drop shape changes and either attains equilibrium at a deformed shape or continues to deform until breakup, depending on whether the deforming forces are strong enough to overcome the effect of interfacial tension forces which keep the drop spherical.

The parameters that affect the drop shape can be classified into dimensionless groups. The dimensionless parameters that will be analyzed in this work are, Capillary number (Ca), Deborah Number (De) and viscosity ratio (λ). The capillary number is defined to be $Ca = G\mu a/\gamma$, where G is the flow strength, μ the viscosity of the matrix or continuous phase and a is the radius of the undeformed drop. The capillary number may be interpreted as the ratio of viscous stresses exerted on the drop to the interfacial tension force that resists deformation. The Deborah number is a dimensionless measure of viscoelastic stresses. The viscosity ratio, defined as the ratio of viscosity of the drop to the viscosity of the matrix fluid, plays a critical role in determining the shape of the drop and modes of breakup. However, the effect of the viscosity ratio will not be analyzed as the focus is on the effect of viscoelasticity. For all cases discussed in this document the viscosity ratio $\lambda = 1$.

2.1.2 Governing Equations and Dimensionless Parameters

The governing equations are the same for both the drop deformation problem and the buoyant bubble problems. However, the characteristic velocity scales are different for the

two problems; the velocity scale for the drop problem is the wall velocity and for the bubble problem it is the terminal velocity of the bubble U.

The domain containing the drop (or a bubble) is denoted by Ω, and the domain boundary by Γ. The upstream part of Γ will be denoted by Γ^-. The governing equations for the two fluid system are:

$$\nabla \cdot \mathbf{u} = 0 \tag{2.2}$$

$$\rho \left[\frac{\partial \mathbf{u}}{\partial t} + \mathbf{u} \cdot \nabla \mathbf{u} \right] = \rho \mathbf{g} - \nabla p + \nabla \cdot \left(\frac{c}{\lambda_r} \mathbf{A} \right) + \nabla \cdot (2\eta_s \mathbf{D}) + \gamma \kappa \delta(\phi) \mathbf{n} \tag{2.3}$$

$$\mathbf{u} = \mathbf{u}_L \text{ on } \Gamma \tag{2.4}$$

The evolution of the configuration tensor **A** is given by

$$\frac{\partial \mathbf{A}}{\partial t} + \mathbf{u} \cdot \nabla \mathbf{A} = \mathbf{A} \cdot \nabla \mathbf{u} + \nabla \mathbf{u}^T \cdot \mathbf{A} - \frac{1}{\lambda_r} (\mathbf{A} - \mathbf{I}) \tag{2.5}$$

$$\mathbf{A} = \mathbf{A}_L \qquad \text{on } \Gamma^-.$$

Equation 2.2 is the continuity equation and Equation 2.3 is the momentum conservation equation which must be solved using the boundary condition of Equation 2.4. Equation 2.5 is the constitutive equation for the Oldroyd-B model. The constitutive equation is discussed in detail later in this chapter. Here **u** is the velocity, p is the pressure, η_s is the solvent viscosity, ρ is the density, **D** is the symmetric part of the velocity gradient tensor, c is a measure of polymer concentration in terms of the zero shear viscosity, **n** is the outer normal, γ is the surface tension, κ is the surface curvature, ϕ is the scalar distance from the interface, δ is the delta function, and λ_r is the relaxation time. The zero shear viscosity $\eta = \eta_s + \eta_p$, where $\eta_p = c\eta_s$ is the polymer contribution to viscosity. The fluid retardation

time is equal to $\frac{\lambda_r}{1+c}$. The surface tension force acts only along the interface where the level set function ϕ is zero. Also note that in the Newtonian region since the relaxation time is zero, $\mathbf{A} = \mathbf{I}$ and the viscoelastic stress term in Equation 2.5 drops out because $\nabla \cdot \mathbf{A}$ is zero.

2.2 Gravity Driven Flow

2.2.1 Problem Description

A drop of a fluid with viscosity η_d and density ρ_d is placed in an ambient fluid with viscosity η_L and density ρ_L (the outside fluid will be referred to as the matrix fluid). The drop is immiscible with the matrix fluid. If the densities of the drop and the matrix fluid are equal, in the absence of an imposed flow the drop assumes a spherical shape due to the interfacial tension force. If the density of the drop is smaller than that of the matrix fluid, due to the buoyancy effect, the drop will rise (See Figure 2.2).

In buoyancy driven flows, it is assumed that there is no externally imposed velocity field and the bubble (immiscible with the bulk fluid), rises in the bulk fluid due to differences in densities. Simulations were started by releasing the bubble at a distance of 1 cm from the bottom of the domain and the transient velocities and shape changes were monitored. At start the viscoelastic stresses are assumed to be zero.

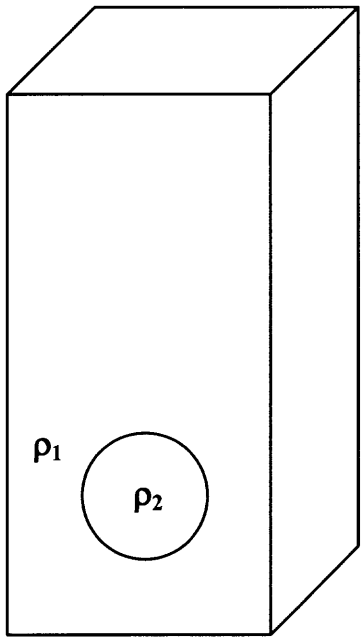

Figure 2.2 A bubble placed at the bottom rises up due to buoyancy.

2.2.2 Governing Equations and Dimensionless Parameters

The governing Equations 2.2–2.5 are non-dimensionalized using the following length, time, velocity, pressure and stress scales: a, a/U, U, ρU^2 and ρU^2, respectively.

Using this scaling, the dimensionless equations, written using the same symbols for the dimensional variables are:

$$\left[\frac{\partial \mathbf{u}}{\partial t}+\mathbf{u}\cdot\nabla\mathbf{u}\right]=\frac{\mathbf{g}}{\mathrm{Fr}}-\nabla p+\frac{1}{\mathrm{De}}\frac{1}{\mathrm{Re}}\nabla\cdot(c\mathbf{A})+\frac{1}{\mathrm{Re}}\nabla\cdot(2\mathbf{D})+\frac{1}{\mathrm{Re}}\frac{1}{\mathrm{Ca}}\kappa\delta(\phi)\mathbf{n} \tag{2.6}$$

$$\nabla\cdot\mathbf{u}=0 \tag{2.7}$$

$$\frac{\partial \mathbf{A}}{\partial t}+\mathbf{u}\cdot\nabla\mathbf{A}=\mathbf{A}\cdot\nabla\mathbf{u}+\nabla\mathbf{u}^{\mathrm{T}}\cdot\mathbf{A}-\frac{1}{\mathrm{De}}(\mathbf{A}-\mathbf{I}) \tag{2.8}$$

The above equations contain the following dimensional parameters: $De = \frac{U\lambda_r}{a}$, the Deborah number, which is a dimensionless measure of relaxation time; $Re = \frac{Ua}{\eta_o}$, the Reynolds number, which is the ratio of inertial and viscous forces; $Ca = \frac{U\eta_o}{\gamma}$, the capillary number, which is the ratio of viscous and surface tension forces, and $Fr = \frac{U}{\sqrt{ga}}$, the Froude number, which is the ratio of inertial and gravitational forces. The other useful parameter which gives the relative importance of the inertial and the surface tension force is the Weber number, $We = Re\,Ca$.

2.3 Constitutive Equations

The fundamental assumptions of Newtonian fluid dynamics, upon which the Navier-Stokes equations are based, are that the fluid is isotropic and the stress is linearly related to the strain rate. When a Newtonian fluid is subjected to a simple shear flow, as indicated by Equation 2.9, the shear stress is given by

$$\tau_{yx}(t) = -\mu \frac{\partial u_x}{\partial y} = -\mu \dot{\gamma}_{yx}(t) \qquad (2.9)$$

The shear stress at time t is proportional to the velocity gradient at the same time t. The flow of many naturally occurring fluids, such as water, air, etc., is governed by Equation 2.9.

If, instead of Newtonian fluid, a Hookean solid was placed between the plates and the upper plate moved by an infinitesimal distance $U(t_o, t)$, the shear stress for the Hookean solid is given by

$$\tau_{yx}(t_o,t)=-G\frac{\partial u_x}{\partial y}=-G\gamma_{yx}(t_0,t) \qquad (2.10)$$

where G is the elastic modulus (not to be confused with shear rate G). The stress at time t is proportional to the strain at time t, referred to the isotropic stress at time t_o. The Hookean solid remembers its state at time t_o, in contrast to the Newtonian fluid, which has no memory of past events.

There are some fluids that exhibit both viscous and elastic properties and are hence referred to as viscoelastic fluids. And for such fluids the governing constitutive equation is one that combines the elastic as well as viscous response exhibited by these fluids.

The term constitutive equation refers to an equation relating the stress in some fluid to its past state of motion. The constitutive equation for an ideal fluid is, $\tau = - p \mathbf{I}$, and for a Newtonian fluid is $\tau = - p \mathbf{I} + 2\mu\mathbf{D}$, where $\mathbf{D}$ is the symmetric part of the deformation gradient tensor. A constitutive equation should satisfy coordinate invariance, material objectivity and it should be deterministic, i.e., the state of stress should depend only past states.

In dealing with constitutive equations for viscoelastic fluids, linear viscoelastic models will be considered first. The idea is to combine Newton's law of viscosity and the Hooke's law of elasticity, and arrive at a stress-strain relationship to represent a viscoelastic fluid.

2.3.1 Linear Viscoelastic Models

If the stress $\sigma(t)$ and the strain $\gamma(t)$ are assumed to be linearly related, then

$$\left(1+a_1\frac{\partial}{\partial t}+a_2\frac{\partial^2}{\partial t^2}+\cdots\cdots+a_n\frac{\partial^n}{\partial t^n}\right)\sigma(t)=\left(b_o+b_1\frac{\partial}{\partial t}+b_2\frac{\partial^2}{\partial t^2}+\cdots\cdots+b_n\frac{\partial^n}{\partial t^n}\right)\gamma(t) \quad (2.11)$$

where a_0, a_1, a_2 and b_0, b_2, b_3 are material constants.

Let us consider some special cases:

1) When $b_o \neq 0$, and all other a's and b's are zeros, $\sigma = b_o\gamma$, which implies $\sigma = G\gamma$ This is Hooke's law for elastic solids, where G is the elasticity modulus.

2) When $b_1 \neq 0$, and all other a's and b's are zeros, $\sigma = b_1\frac{\partial\gamma}{\partial t} = b_1\dot{\gamma}$. This is Newton's law of viscosity, where μ is the viscosity.

3) When $b_o = G$ and $b_1 = \mu$, and all other a's and b's are zeros, $\sigma = G\gamma + \mu\dot{\gamma}$. This is called **Kelvin's** model and is one of the simplest models of viscoelasticity.

4) When $a_1 = \tau_m$ and $b_1 = \mu$ and all other a's and b's are zeros,

$$\sigma + \tau_m(\dot{\sigma}) = \mu\dot{\gamma}_s \quad (2.12)$$

This is called **Maxwell's** model, the solution to which is of the form

$$\sigma(t) = \int_{-\infty}^{T}\left\{\frac{\mu}{\tau_m}e^{-(t-t^1)/\tau_m}\right\}\dot{\gamma}(t^1)\,dt^1 \quad (2.13)$$

The quantity within parenthesis is called the relaxation modulus for Maxwell's fluid. Equation 2.13 states that the stress at the present time t depends on the rate of strain at the present time as well as on the rate of strain at all past times t^1 with a weighting factor 'relaxation modulus' that decays exponentially as one goes backward in time (fading memory). [Bird et. al. (1987)]

5) When a_1, b_1, $b_2 \neq 0$ and all other a's and b's are set to be equal to zero, the model obtained is called **Jeffery's model**:

$$\left(1+a_1\frac{\partial}{\partial t}\right)\sigma=\left(b_1\frac{\partial}{\partial t}+b_2\frac{\partial^2}{\partial t^2}\right)\gamma \quad (2.14)$$

2.3.2 Retarded Motion Expansion

The idea behind this approach is to obtain an expansion about the Newtonian fluid in which subsequent higher order terms correspond to deviation from Newtonian behavior towards elastic behavior.

The velocity gradient tensor when split into its symmetric and anti-symmetric part gives us the rate of strain tensor and the vorticity tensor. Higher order strain rate tensors are defined by the recurrence relationship:

$$\mathbf{D}(1) = \mathbf{D}$$

$$\mathbf{D}(n+1) = \frac{d}{dt}\mathbf{D}(n) - (\nabla \mathbf{v})^{T} \cdot \mathbf{D}(n) + \mathbf{D}(n) \cdot (\nabla \mathbf{v}) \tag{2.15}$$

In order to construct constitutive equation that describe small departure from Newtonian behavior, the stress tensor is written as a function of the rate of strain tensor and higher order rate of strain tensors.

$$\boldsymbol{\sigma} = f\left(\mathbf{D}(1), \mathbf{D}(2), \cdots\cdots \mathbf{D}(n)\right) \tag{2.16}$$

Rearranging the terms in polynomial order,

$$\boldsymbol{\sigma} = \left[b_1 \mathbf{D}(1)\right] + \left[b_2 \mathbf{D}(2) + b_{11} \mathbf{D}(1) \cdot \mathbf{D}(1)\right] - \begin{bmatrix} b_3 \mathbf{D}(3) + b_{12} \left\{\mathbf{D}(1) \cdot \mathbf{D}(2) + \mathbf{D}(2) \cdot \mathbf{D}(1)\right\} \\ + b_{1:11} \left\{\mathbf{D}(1) \cdot \mathbf{D}(1)\right\} \mathbf{D}(1) + \ldots\ldots \end{bmatrix} \tag{2.17}$$

Note:

1) If only $b_1 = \mathbf{u}$ and all the other b's are zero, the resulting fluid is a Newtonian fluid.
2) If all terms in the second parenthesis are included, it results in a second order fluid and including the third parenthesis produces a third order fluid, and so forth.

The retarded motion expansion is a purely theoretical model. Though it is limited in use, it still gives some valuable insight about behavior of elastic molecules and structure of wakes in rising bubbles or falling spheres [Joseph (1995)].

2.3.3 Differential Form of Constitutive Equations

In the previous sections two forms of constitutive equations were considered that were useful in a limited way, but those models are not sufficiently robust to fully describe these complex fluids in different flows.

One of the requirements of a constitutive equation is that it must be frame invariant, i.e. frame invariance ensures that one will not obtain a new law every time a new coordinate system is chosen.

Oldroyd proposed that frame invariance could be recovered by writing the constitutive equation in the frame of reference that is convected or deformed with the material elements. This can be done by redefining the time derivative in a convected co-ordinate system. There are two convected coordinate systems, contravariant and covariant.

Contravariant: The base vectors are parallel to the material lines. They stretch and rotate with the material lines. This is also called the upper convected derivative

$$\frac{\delta \boldsymbol{\sigma}}{\delta t} = \overset{\nabla}{\boldsymbol{\sigma}} = \frac{d\boldsymbol{\sigma}}{dt} - \nabla \mathbf{u}^{T} \cdot \boldsymbol{\sigma} - \boldsymbol{\sigma} \cdot \nabla \mathbf{u} \tag{2.18}$$

Covariant: The base vectors are normal to the material planes. The base vectors rotate to remain normal and stretch so that their lengths remain proportional to the area of the material planes to which they are normal. This is also the lower convected derivative.

$$\frac{\delta \boldsymbol{\sigma}}{\delta t} = \overset{\Delta}{\boldsymbol{\sigma}} = \frac{d\boldsymbol{\sigma}}{dt} - \nabla \mathbf{u} \cdot \boldsymbol{\sigma} - \boldsymbol{\sigma} \cdot \nabla \mathbf{u}^{T} \tag{2.19}$$

Using the upper and lower convected derivates in the Maxwell model, Equation 2.12, and applying tensorial generalization yields:

$$\sigma + \tau_m \overset{\nabla}{\sigma} = \mu \dot{\gamma} \text{ -- The upper convected Maxwell Model} \tag{2.20}$$

$$\sigma + \tau_m \overset{\Delta}{(\sigma)} = \mu \dot{\gamma} \text{ -- The lower convected Maxwell Model} \qquad (2.21)$$

2.3.4 Oldroyd-B Fluid

For an Oldroyd-B fluid, the stress σ is given by:

$$\sigma = \sigma_S + \sigma_P \qquad (2.22)$$

where, $\sigma_S = 2\mu \mathbf{D}$ is the solvent contribution to stress (purely viscous) and σ_P is the polymeric contribution to stress, and it is given by (2.20).

The evolution of the configuration tensor is given by [Oldroyd (1958)]

$$\frac{\partial \mathbf{A}}{\partial t} + \mathbf{u} \cdot \nabla \mathbf{A} = \mathbf{A} \cdot \nabla \mathbf{u} + \nabla \mathbf{u}^T \cdot \mathbf{A} - \frac{1}{\lambda r}(\mathbf{A}-\mathbf{I}) \qquad (2.23)$$

Constitutive equations have been generated in several ways and in addition to the few discussed there are several constitutive models to choose between like the FENE-CR dumbell-based model of Chilcott and Rallison (1988) to name one. The Oldroyd-B model is used in this analysis; it is popularly accepted and has been used to model flow of viscoelastic fluid past spheres [Tiefenbruck and Leal (1982)] and is somewhat closer to experimental facts [Bodart and Crochet (1992)].

2.4 Relaxation Time and Deborah Number

When a Newtonian fluid, such as water is subjected to shear stress, it responds instantaneously and begins to flow. Contrary to what is seen in Newtonian fluids, viscoelastic fluids have memory of their past state and their response to shear stress is not instantaneous. Similarly, the relaxation time also quantifies the amount of time a viscoelastic fluid takes to regain equilibrium zero stress state after the flow stops. In a

time dependent flow, the stress in a material element depends on the past strain history over the time interval of λ_r. Though no fluid response is perfectly instantaneous, a fluid such as water with $\lambda_r \approx 10^{-11}$s and can be considered Newtonian. Lubricating oils have relaxation time $\approx 10^{-6}$s, while polymeric melts typically have relaxation time of 0.1 – 10s. The nature of the fluid response depends both on the relaxation time as well as the time scale of observation. "Silly Putty" is a good example of a viscoelastic fluid which behaves like an elastic ball when thrown to the floor (exhibits elastic response), but when left in a container for a long period of time it takes the shape of the container (viscous behavior). The difference between the two experiments described above is the time scale of observation. The same material shows elastic response when force is applied for time durations shorter than λ_r, but behaves like a viscous liquid when the force is applied for time durations longer than λ_r.

To quantify the relative importance of the viscous and elastic responses, Reiner (1964) introduced a new dimensionless parameter called the Deborah number (De), which is defined to be the ratio of the fluid relaxation time to the characteristic time of the flow

$$De = \frac{\lambda_r}{t_{flow}} \tag{2.24}$$

In the limit of De$\rightarrow$ 0, the fluid behaves like a Newtonian liquid and behaves like an elastic Hookean solid when De $\rightarrow \infty$. The elastic effects becomes significant when De $\cong$ 1.

At small values of De, the thermal motions keep the polymer molecules more or less in equilibrium configuration, and thus the response of polymeric fluids are approximately

the same as that of a Newtonian fluid. But, when De is large the polymer molecules that are highly stretched and hence the stress at a material point is related to the past strain rate history at that point.

In this document, the characteristic time scale of flow depends on the nature of the flow. For simple shear flows, it is defined based on the shear rate G, and for the buoyancy driven flow it is defined based on the terminal velocity of the bubble and its undeformed radius. In a simple shear flow, the time scale of the flow is the reciprocal of the strain rate, and thus Deborah number is defined as,

$$De = \lambda_r G \tag{2.25}$$

Notice that in this definition De does not depend on the drop radius. For buoyancy driven flow of a bubble in a quiescent liquid, the time scale of the flow is $\frac{U}{a}$ where U is the terminal rise velocity of the bubble and a is the undeformed bubble radius. The Deborah number for a rising bubble is defined as

$$De = \frac{\lambda_r U}{a} \tag{2.26}$$

CHAPTER 3

LITERATURE REVIEW

3.1 Drop Deformation in Simple Shear Flow

Using a parallel band apparatus to generate simple shear flows, Taylor (1932) was one of the first to study the deformation of drops. Over the last seventy years different aspects of drop deformation have come into focus. While analysts have come up with higher order schemes to model large deformations from spherical shapes, experimentalists have studied different aspects of deformation – critical capillary number, modes of break-up, effect of viscosity ratio, effect of surfactants, etc. It was not until the early 70's that research on the influence of viscoelasticity on drop deformation gained prominence. In the last two decades, direct numerical schemes have also been developed for investigating the dynamics of drop deformation. While greater emphasis in this document is on the effect of viscoelasticity on drop deformation, the effects of drop deformation in Newtonian flows are be briefly touched upon.

Taylor (1934) was the first to observe experimentally that in the absence of inertial effects the shape of the drop of radius a, subjected to a simple shear flow of strength G in a matrix fluid of viscosity μ is a function of two dimensionless groups. The capillary number $Ca = G\mu a/\gamma$, the ratio of viscous stress exerted on the drop to the interfacial tension force that resist deformation and the viscosity ratio λ. Here γ is the interfacial tension. He observed that for a fixed λ, the deformation parameter which he defined as $D = \frac{L-B}{L+B}$ is a linear function of Ca for small values of the shear rate G. But

beyond a certain range the slope of the curve increased rapidly and until no steady state shape could be obtained and the drop burst rapidly. Rumscheidt and Mason (1961) extended Taylor's experimental work and dealt with deformation and break-up of drops in shear flows while Grace (1971) studied the deformation of drops for a wide range of viscosity ratios.

Theoretically, the deformation of drops in shear flows was approached in two ways – one that modeled small deformations from sphericity [Taylor (1934), Barthes-Biesel and Acrivos (1973a)] and the slender body theory [Taylor (1964), Acrivos and Lo (1978), Hinch and Acrivos (1979, 1980)] that modeled large deformation from spherical shapes. For a greater overview of Newtonian effects on drop deformation the reader is referred to reviews that elaborate on different aspects of deformation of a drop in Newtonian simple shear flows [Rallison (1984) and Stone (1994)].

Fulmerfelt (1972) reported one of the first experimental observations on the effect of elasticity on drop deformation. For Newtonian drops sheared by viscoelastic fluid, he obtained the value for D_{min}, the minimum diameter below which no break-up was possible, for different matrix elasticities. He observed that D_{min}, as well as the critical shear rate required to cause breakup increased with an increase in matrix elasticity. In the same year, Tavgac (1972) published experimental results for deformation of viscoelastic drops in viscoelastic shear flows. He observed that the elastic forces due to the matrix phase either inhibits or initiates break-up depending on the viscosity ratio.

Elmendorp and Maalcke (1985) established a relation between the deformation and normal stress contribution to the stress balance at the interface. They concluded that for a drop of viscoelastic fluid placed in a simple shear flow of a Newtonian fluid, the

drop having higher normal stress appeared to be more stable. They further noted that normal stress of the viscoelastic matrix phase destabilized a Newtonian droplet in a simple shear flow when the matrix fluid is viscoelastic. Ramaswamy and Leal (1999) later showed that though this argument seemed logical and reasonable, such an agreement is merely fortuitous. The relationship between the viscoelastic stresses and deformation was found to be far more complicated and a simple picture based on the normal stress balance at the interface.

Another behavioral aspect of drop deformation, when one or both fluid are viscoelastic which is strikingly different from that involving Newtonian fluids is the process of breakup. For Newtonian fluids, break-up occurs either via drop fracture or due to the onset of capillary wave instabilities. When either phase is viscoelastic, the drop loses fluid from the ends, a phenomenon better known as tip streaming. De Bruijn (1989, 1993) analyzed the break-up of droplets in simple shear flows. He observed that at higher shear rates the drops were ellipsoidal in shape while at lower shear rates, the drops were sigmoidal in shape.

Varanasi et al. (1994) characterized the deformation of viscoelastic drops in Newtonian simple shear flows. They noted for any given value of viscosity ratio, Ca_c-the critical capillary number required for breakup increased with increasing shear rate unlike Newtonian fluids for which Ca_c is independent of shear rate. Further, when both viscosity ratio and shear rate are held fixed, Ca_c was found to increase with increase in weight fraction of the polymer in the solution (elasticity of the dispersed phase). Levitt and Macosko (1996) carried out drop deformation studies in which both the drop phase and the matrix fluid were viscoelastic. They observed that for high matrix elasticities, the

drops stretched perpendicular to the flow direction. They also established an analytical relation between the second normal stress difference of the phases and the degree of drop widening. Guido and Villone (1998) also noted that cross-sections of ellipsoidal drops were not circular. The short axis measured in the shearing plane was slightly shorter than that measured in the perpendicular plane.

Deformation and break-up mechanisms of viscoelastic drops in Newtonian simple shear flows at large capillary numbers were studied by Tsakalos et al. (1998). It can be observed from their results that the viscoelastic drops in Newtonian shear flows are consistently less deformed than Newtonian drops in Newtonian shear flows. In an experimental set up in which the matrix as well as the drop phase were viscoelastic, Mighri et al. (1998) showed that drop resistance to deformation increases as elasticity ratio increases (defined as the ratio of relaxation time of the drop to that of the fluid). They showed that the deformation decreases with increasing drop elasticity while deformation increases with increase in matrix elasticity.

One fact that stands out consistently from all of the above published results is that when one phase is viscoelastic and the other Newtonian, the net effect of viscoelasticity is a reduction in deformation when the drop phase is viscoelastic and an increase in deformation when the matrix phase is viscoelastic. In the event of both the drop and matrix phases being viscoelastic, the behavior is governed by the ratio of elasticity of the two fluids. The reasons for these observations however are not well understood. Moreover, since in experiments, elasticity of the fluid is controlled by increasing or decreasing the polymer concentration, the relaxation time also changes. It is difficult to generate a range of fluids having the same level of polymer concentrations with varying

relaxation times, which clouds our ability to draw a distinction between the effect of varying concentration and varying relaxation time. Numerically, it is much easier to study the effects of polymer concentration at constant relaxation time and vice versa. This ability to vary one parameter while keeping the other fixed helps us isolating the effect of contributions to fluid elasticity and their role in deformation of drops.

3.2 Buoyant Bubble Rising in a Viscoelastic Fluid

The motion of a bubble rising in a viscoelastic fluid is one of the fundamental research problems in the field of non-Newtonian fluid mechanics. This problem is interesting in more than one way due the presence of a negative wake at the trailing edge, the loss of fore-aft symmetry due to the formation of a cusp shaped trailing end and an apparent discontinuity in the plot of the steady state velocity vs. bubble volume.

The wake behind a bubble rising in a viscoelastic fluid is called negative wake because the velocity in the wake, very close to the trailing end, is in the direction of motion of the bubble, but, a short distance away from the trailing end, the velocity reverses direction. (For a bubble rising in a Newtonian liquid, the wake is normal, as the velocity in the wake is in the same direction as the motion of the bubble). Hassagar (1979) was the first to observe this behavior and coined the term *negative wake.* Negative wake is also observed for spheres falling in viscoelastic liquids [see Arigo and McKinley (2001) and references therein].

Funfschilling and Li (2001) using particle image velocimetry (PIV) and Bisgaard (1983) using laser doppler anemometry (LDA), investigated the detailed flow field behind rising bubbles. From the PIV plots, Funfschilling and Li (2001) noted the

presence of three distinct zones around a rising bubble: a central downward flow zone behind the bubble or negative wake, a conical upward flow surrounding the negative wake zone and an upward flow zone in front of the bubble. Bisgaard (1983) analyzed the flow around a rising bubble and a falling sphere, and observed that the negative wake is much closer to the trailing end of a bubble than it is to the trailing end of a sphere, i.e., the distance from the trailing end where the velocity reverses direction is smaller for a bubble.

The second interesting feature of a bubble rising in a viscoelastic fluid is the cusp like shape of trailing end of the bubble for volumes larger than a critical value. Philippoff (1937) was the first to notice this phenomenon [also see Chabra and DeKee (1992), Chhabra (1993), and references listed therein). Liu, Liao and Joseph (1995) performed experiments for bubbles rising in viscoelastic fluids, inside columns of different cross-sections and found that the trailing end is not axisymmetric. Specifically when the bubble is viewed from a side a cusp can be observed in the wide window and a broad trailing edge appears in the narrow window.

Astarita and Apuzzo (1965) noted that in addition to the aforementioned shape change, "*the steady state velocity-volume curve in highly elastic liquids shows a striking peculiarity: a critical volume exists corresponding to an abrupt increase in the velocity.*" They studied terminal velocities of bubbles rising in four different liquids – aqueous solutions of carbopol which is a purely viscous highly pseudo plastic liquid, aqueous solutions of carboxy methyl cellulose - CMC which is slightly elastic, aqueous solution of ET497 which is highly elastic and aqueous solution of J100 a fluid rheologically similar to ET497. The gas bubbles rising in viscous carbopol and slightly elastic CMC

solutions, deform from spherical to oblate ellipsoidal shape and then to spherical cap with increasing volume, qualitatively similar to bubbles rising in Newtonian liquids. Bubbles rising in highly elastic ET497 and J100 deform from spherical to prolate shapes with marked cusp shaped trailing edges with increasing volume. Moreover, at a critical volume v_c, there is an abrupt increase in the rise velocity, which varies between 2.2 to 5.86 times the velocity before the onset of this sudden increase, depending on the percentage of polymer additives ET497 or J100 added. They further noted that "*The shape of the bubble also undergoes a transition at v_c, although not very marked at critical volume when $v < v_c$, although the rear pole is cuspidal, the whole bubble surface appears to be convex. In contrast to this, when $v > v_c$, the protruding tip at the rear pole is more marked and the bubble surface appears to be concave along an horizontal circle slightly above the protruding tip.*" They explained that this abrupt increase in the velocity is due to the transition from the Stokes regime† to the Hadamard regime†. Since a similar transition in Newtonian liquid is not accompanied by an abrupt increase in rise velocity, they concluded that viscoelasticity is responsible for this transition.

Following the work of Astarita and Apuzzo (1965), several researchers investigated this phenomenon experimentally-Barnett and Humphrey (1966), Calderbank, Johnson and London (1970) and Leal, Skoog and Acrivos (1971). Leal et al. (1971) compared the terminal velocities for rising bubbles and falling glass spheres in a Separan-AP30 solution ranging in concentration from 0.04 to 1% by weight. The density

† According to Astarita and Apuzzo (1965) , "A gas bubble moves in the Stokes regime when the liquid is in creeping flow, the bubble is spherical, and the interface is rigid. A gas bubble moves in the Hadamard regime when the liquid is in creeping flow, the bubble is spherical, and the interface is free."

of the sphere was conveniently chosen to match the terminal rise velocity of an air bubble. Since they did not observe any velocity transition for the sphere, they concluded that the observed velocity discontinuity for a bubbles at the critical volume is due to a change in the boundary condition at the interface from no-slip to shear free. They also analyzed the relative importance of the contributions of shear dependent viscosity and elasticity to the discontinuity and suggested that a "relatively modest elastic contribution to force balance at the interface would be sufficient to explain the experimentally observed discontinuity."

Liu, Liao and Joseph (1995) proposed a new explanation for the discontinuity in the rise velocity at the critical volume for the bubbles rising in 1.5% aqueous polyox solution inside channels with rectangular, square and circular cross-sections. They argued that the jump in the rise velocity is due to a reduction in the drag which happens due to a change in the bubble shape. They noticed that the bubbles below the critical volume were prolate and those above the critical volume were pointed with a cusp-like trailing edge. Interestingly, a few years later, Belmonte (2000), observed experimentally that the discontinuity in the velocity-volume plot occurred at the same volume at which the cusp appeared for a bubble rising in a standard weakly elastic power law fluid.

Wagner, Giraud and Scott (2002) developed a two-dimensional Lattice-Boltzmann scheme for two phase flows and used this method to simulate bubbles rising in viscoelastic fluids. They did not observe a significant discontinuity as observed in experiments by Liu et al. (1995) and concluded that "the discontinuity observed in experiments was due to the presence of impurities or surfactant molecules that were absent in their numerical simulation."

Hererra-Velarge, Zenit, Chehata and Mena (2003) analyzed the flow around bubbles using the PIV technique (Particle Image Velocimetry) for bubbles with volume close to the critical volume at which the discontinuous change in rise velocity occurs. They reported that when the bubble volume is smaller than the critical volume, the flow resembled that of a bubble rising in a Newtonian fluid, i.e., the velocity in the wake of the rising bubble was *positive*. For bubbles with volumes greater than the critical volume, they observed a markedly modified velocity distribution and a *negative* wake.

The presence of surface active agents affects the surface tension and consequently the rise velocity and the jump in velocity at a certain critical volume. Rodrigue, DeKee and Chan Man Fong (1996) experimentally investigated the effects of surfactants on the velocity of a bubble rising in a viscoelastic fluid. They analyzed the effects of various concentrations of sodium dodecyl sulphate (SDS), an ionic surfactant on four different viscoelastic fluids – 1 mass% CMC, 1 mass % gellan gum (GEL) in distilled water, 3 mass % polyethylene oxide, and ployacrylamide AP-237 (concentration varying between 0.075 and 0.25). They concluded that surface active agents as well as elastic forces must be simultaneously present in order to modify the surface and generate a sudden jump in the velocities. A summary of published results concerning the discontinuous jump at critical volume is presented in Table 1.

In the past few years, considerable advances have been made in understanding the transient motion and the presence of negative wake behind spheres falling in viscoelastic liquids. Detailed numerical simulations as well as experimental results and elegant explanations have been reported for the falling sphere problem. A review of the articles published on the settling sphere problem can be found in McKinley (2001). The transient

motion of a bubble rising in a viscoelastic fluid however, has not been investigated as rigorously as the falling sphere problem.

Name	Magnitude of jump	Conclusions
Astarita & Apuzzo (1965)	~ 6	Discontinuity is due to transition from Stokes to Hadamard regime.
Liu, et al. (1995)	~10	Discontinuity is due to a sharp reduction in the drag due to cusping.
Belmonte (2000)	~ 4	Discontinuity coincides with cusp formation.
Hererra-Velarge, et al.(2003)	~ 2.4	Only for bubbles with volumes greater than the critical volume, was the negative wake observed. They argue that the discontinuity is due to the presence of the negative wake.

Table 1. Summary of the magnitude of jump and the reasons given for the jump.

Handzy and Belmonte (2003) analyzed the transient oscillatory motion of air bubbles rising in micellar system consisting of an aqueous solution of cetylpyridinium chloride (CPCl) and sodium salicylate (NaSal). For a fixed ratio of [NaSal]/ [CPCl] and concentrations from 4 to 40 mM, they analyzed the transient behavior of bubbles with volumes ranging from 14 mm^3 to 110 mm^3 in cylindrical tanks. They observed that when the concentration of [NaSal]/ [CPCl] is between 5mM – 15mM, bubbles form a cusp shaped tails which lengthen as the bubbles rise during which the velocity of the leading end remains constant. However, the tail suddenly retracts and the bubble jumps upward and then decelerates to a constant velocity and these oscillations persisted for a rise distance of over one meter. For higher concentrations between 25mM - 40mM, the shape of the entire bubbles changes, in contrast to the lower concentrations when only the tail shape changes. Additionally, for intermediate concentrations, no oscillations were observed. They noted that since falling spheres also oscillate [Jayaraman and Belmonte

(2003)] in wormlike micellar fluids, it was unlikely that the surface tension played a role in bubble oscillations, and that "the common aspect to all these oscillations is the nonpermanence of the macromolecular structures which are responsible for the fluid stress and therefore the drag."

Though the rise of a bubble in a viscoelastic fluid has been analyzed via two-dimensional numerical simulations in the past [Wagner, Giraud and Scott (2002) and references therein], a three-dimensional analysis is necessary to understand the nuances of this asymmetrical problem.

CHAPTER 4

INTERFACE TRACKING AND NUMERICAL METHOD

4.1 Interface Tracking

The problem of computing the motion of two-phase flows with interfaces is difficult even for Newtonian fluids because the interface shape changes in response to fluid motion. Across the interface the fluid properties change suddenly and an interfacial force acts along the interface of the two fluids. When one or both phases are viscoelastic the numerical problem is even more complex, as one must also solve for the viscoelastic stresses.

Tracking the interface shape that changes in response to fluid motion is the first step to obtaining a numerical solution to the problem of deformation of drops. Once the position of the interface is known, the equations of flow must be solved in both phases. The level set method [Sussman et al. (1998)] is used to track the interface and the governing equations are discretized using the finite element method. Operater splitting is used to decouple the governing equation into simpler sub-problems.

Another issue requiring numerical dexterity is the discretization of the convection term $\mathbf{u}\cdot\nabla\mathbf{A}$ that appears in the constitutive equation. Numerical errors at higher De occur primarily because of poor approximation of the convection term in the governing equation of the configuration tensor. In this numerical scheme, the third order upwinding developed by Singh and Leal (1993) is used to overcome this difficulty. Additionally, a common observation for both Maxwell's and Oldroyd type model, a De exists at which det$\mathbf{A}$ becomes negative [King et al. (1988), Marachal and Crochet (1986, 1987)). This De

delineates the upper limit for which reasonably smooth numerical solutions can be obtained. It can be shown in an analytical solution that the configuration tensor cannot become negative [Singh and Leal (1993)]. The fact that it does become negative in a numerical scheme is therefore a consequence of numerical error. A technique used to overcome the above mentioned difficulty will be discussed in this chapter.

The study of deformation of drops falls into a well-known category of problem known as free-boundary problems, wherein the interface shape at which the boundary conditions must be applied is not a priori known. Boundary conditions are available at the solid wall in contact with the matrix fluid. It is the boundary condition at the moving interface that is of concern. In this work the real interfacial region, in which physical properties vary rapidly but continuously, is replaced by a macroscopic surface, with properties such as density and viscosity that are modeled as retaining their bulk values right up to the surface and then changing discontinuously [Leal (1992)]. The interface is characterized by interfacial tension and the boundary conditions prescribed at the interface are continuity of velocity and shear stress across the interface, normal component of velocity is continuous and the normal stress suffers a jump across the interface which equals the surface tension force.

There are several numerical approaches available for tracking the interface between two immiscible Newtonian liquids such as the surface tracking method [Unverdi and Tryggvason (1992)], volume of fluid method [Fatemi and Odeh (1992), Hirt and Nichols (1982)], the mapping method [Ryskin and Leal (1984)] and the level set method [Sussman et al. (1998), Osher and Sethian (1988), Sussman et. al. (1994), Sussman and Smereka (1997)]. These methods have been used extensively to simulate viscous and

inviscid two-phase flows. Due to the inherent complexity of viscoelastic flows, there are relatively fewer numerical schemes such as the moving grid method [Bousfield et al. (1988)], the mapping method [Noh et al. (1993), Ramaswamy and Leal (1999)], and the references listed in these papers. In this study the level set method is used to track the interface.

In the level set method [Sussman et al. (1998)], the interface position is not explicitly tracked, but is defined to be the zero level set of a smooth function ϕ, which is assumed to be the signed distance from the interface. In implementing the level set method, ϕ is assumed to be negative inside the drop surface and positive outside. Along the interface ϕ is assumed to be zero. In order to track the interface, the level set function is advected according to the velocity field, i.e.,

$$\frac{\partial \phi}{\partial t} + \mathbf{u} \cdot \nabla \phi = 0 \tag{4.1}$$

Clearly, if ϕ satisfies the above equation and $\phi = 0$ at $t = 0$ along the interface, the zero level set of ϕ marks the interface for all $t > 0$. When ϕ is advected according to Equation 4.1 it will not remain the distance function for the points away from the interface, and therefore it must be reinitialized to be a distance function. But, since only the zero level set is physically relevant, as noted in [Chang et al. (1996)], "we have a lot of freedom in extending the level set function outside the interface."

It is worth noting that since an explicit scheme is used to advect the interface according to Equation 4.1, the CFL criterion is pertinent to calculations and thus when the time step is too large the numerical method fails.

Re-initialization of ϕ

The level set function ϕ is reinitialized to be a distance function after each time step by solving the following equation obtained in [Sussman et al. (1994)], to the steady state

$$\frac{\partial \phi}{\partial t} + \mathbf{w}.\nabla\phi = S(\phi_0) \tag{4.2}$$

where ϕ_0 is the distribution to be reinitialized and

$$\mathbf{w} = S(\phi_0)\frac{\nabla\phi}{|\nabla\phi|} \tag{4.3}$$

Here $S(\phi_0)$ is the sign function, i.e., $S(\phi_0) = 1$ if $\phi_0 > 0$ and $S(\phi_0) = -1$ if $\phi_0 < 0$. In order to avoid discontinuities, the following smoothed sign function is used

$$S(\phi_0) = \frac{\phi_0}{\sqrt{\phi_0^2 + h^2}} \tag{4.4}$$

where h is equal to one and half times the element size. Equation 4.2 is a first order hyperbolic partial differential equation which is solved using a positive only upwinding scheme described in [Glowinski et al. (1999)]. Clearly, the characteristics of Equation 4.2 point in the direction of **w**. Therefore, for the points outside the drop **w** points away from the drop and for the points inside the drop it points inwards. Thus, Equation 4.2 can be solved by specifying the boundary condition $\phi = \phi_0$ at the two-fluid interface $\phi = 0$.

4.2 Variation of Density, Viscosity, and Relaxation Time Across The Interface

In the finite element scheme the fluid viscosity is assumed to take a jump across the interface, i.e.,

$$\eta = \begin{cases} \eta_D & \text{if } \phi < 0 \\ 0.5(\eta_D + \eta_L) & \text{if } = 0 \\ \eta_L & \text{if } \phi > 0 \end{cases} \tag{4.5}$$

Here η_d and η_L are the viscosities of the fluids inside and outside the drop, respectively. In other words, the nodes that are inside the drop have the drop viscosity and the nodes that are outside have the fluid viscosity. The fluid density, on the other hand, is assumed to vary smoothly across the interface

$$\rho = \begin{cases} \rho_D & \text{if } \phi < -h \\ \rho_L & \text{if } \phi > h \\ 0.5(\rho_D + \rho_L) + 0.5(\rho_D - \rho_L)\sin\left(\dfrac{\pi\phi}{2h}\right) & \text{otherwise} \end{cases} \tag{4.6}$$

where h is equal to one and half times the element size, and ρ_d and ρ_L are the densities of the fluids inside and outside the drop, respectively. This smoothing of the density is similar to that in [Sussman et al. (1994)], and is needed for avoiding numerical instabilities for relatively large density ratio ρ_d/ρ_L. The fluid relaxation time is assumed to jump across the interface

$$\lambda_r = \begin{cases} \lambda_{rd} & \text{if } \phi < 0 \\ 0.5(\lambda_{rd} + \lambda_{rL}) & \text{if } \phi = 0 \\ \lambda_{rL} & \text{if } \phi = 0 \end{cases} \tag{4.7}$$

Here λ_{rd} and λ_{rL} are the relaxation times of the fluids inside and outside the drop, respectively. If the fluid inside (or outside) the drop is Newtonian its relaxation time is set to zero. A relaxation time of zero ensures that the fluid relaxes instantaneously and thus behaves like a Newtonian fluid. This permits the use of the same equations for both Newtonian and viscoelastic liquids.

The surface tension force is smoothed and acts only on the elements for which ϕ is smaller than h. This is done by approximating $\delta(\phi)$ in Equation 3.2 by a mollified delta function $\delta_h(\phi)$ using the approach described in [Sussman et al. (1994)]:

$$\delta_h(\phi) = \begin{cases} \dfrac{\left(1+\cos\left(\dfrac{\pi\phi}{h}\right)\right)}{2h} & \text{for} \mid \phi \mid < h \\ 0 & \text{otherwise} \end{cases} \tag{4.8}$$

For the two-dimensional approach an unstructured mesh is used, while a structured mesh is used for the three-dimensional case. The element size is constant for the three-dimensional case but for the two-dimensional case the element size near the drop is kept approximately constant which is used to define h to be one and half times the average element size near the drop, where the element size is equal to the side of a square whose area is two times that of a triangle.

The error introduced by smoothing of the surface tension force is O(h) [See Brackbill et al. (1992)] for a detailed discussion). Also note that Equations 4.7 and 4.8 require that ϕ be maintained as a distance function which is done by reinitializing ϕ after each time step.

One of the attractive features of this approach is that it is relatively easy to implement in both two and three dimensions. In fact, an algorithm developed for two dimensions can be easily generalized to three dimensions. The level set function can be represented using the same finite element basis functions as that for the velocity field. Also, the method does not require any special treatment when a front splits into two or when two fronts merge.

4.3 Numerical Method

In this method the governing equations are solved simultaneously everywhere, i.e., both inside and outside the drops/bubbles in the domain. This approach is different from the methods where the flow fields inside and outside the drop are decoupled and solved separately [Ramaswamy and Leal (1999)]. In a decoupled approach one must apply suitable boundary conditions at the interface, i.e., impose the continuity of velocity and shear stress across the interface, and the jump in the normal stress across the interface is set to be equal to the surface tension force. Since in this approach the governing equations are solved in a coupled manner, the method is stable and allows us to take relatively large time steps.

The finite element scheme uses the Marchuk-Yanenko operator-splitting technique to decouple the difficulties associated with the incompressibility constraint, the nonlinear convection term, the interface motion, and the viscoelastic term [Marchuk (1990), Glowinski et al. (1999), and Singh et al. (2000)]. The operator splitting scheme gives rise to the following four sub-problems: A Stokes like problem for the velocity and pressure; a non-linear convection-diffusion problem for the velocity; an advection problem for the configuration tensor; and an advection problem for the interface. The first problem is solved by using a conjugate gradient (CG) method [Glowinski et al. (1992)] and the second problem is solved using a least square conjugate gradient method [Bristeau et al. (1987)]. The third problem is a hyperbolic partial differential equation for the configuration tensor. As mentioned earlier while discussing the Oldroyd-B constitutive model, the convection term $\mathbf{u}\cdot\nabla\mathbf{A}$ poses certain numerical difficulties. The two key features of the numerical method used for solving this problem are: a scheme

that ensures the positive definiteness of the configuration tensor, and a third order upwinding scheme for discritizing the advection term in the constitutive equation [Singh and Leal (1993)]. These two features are important for obtaining a split scheme that is stable at relatively large Deborah numbers. The fourth problem is for the advection of the level set function ϕ, which is solved using a third order upwinding scheme [Glowinski and Pironneau (1992)]. The advected ϕ is then reinitialized to be a distance function, which, as noted in [Sussman et al. (1994)], is essential for ensuring that the scheme accurately conserves mass. Also note that the linear systems in the Stokes-like and nonlinear problems are symmetric, and hence can be solved by using the conjugate gradient algorithm. The product of the global matrix and vectors, required in the conjugate gradient algorithm, is computed directly without assembling the global matrix of the linear system. This reduces the memory requirement of the computer program.

4.4 Weak Form

The weak form of the governing equations is obtained by multiplying Equations 3.1, 3.2, 3.4 and 3.5 by the test functions, and integrating the second order term by parts. This is a straightforward procedure with an additional complication that the fluid properties are not constant in the domain. Furthermore, since the fluid is viscoelastic, the constitutive Equation 3.4 also needs to be solved along with the momentum and continuity equations. In obtaining this weak form, the hydrodynamic stresses acting at the interface are completely eliminated.

To state the combined weak form for the equation of motion need the following spaces are needed:

$$W_u = \{\mathbf{v} \in H^1(\Omega)^2 \mid \mathbf{v} = \mathbf{u}_\Gamma(t) \quad \text{on} \quad \Gamma\},$$

$$W_{u0} = \{\mathbf{v} \mid \mathbf{v} \in H^1(\Omega)^2 \text{ and } \quad \mathbf{v} = 0 \text{ on } \Gamma\}$$

$$W_A = \{\mathbf{A} \in H^1(\Omega)^3 \mid \mathbf{A} = \mathbf{A}_L(t) \quad \text{on} \quad \Gamma^-\},$$

$$W_{A0} = \{\mathbf{A} \in H^1(\Omega)^3 \mid \mathbf{A} = 0 \quad \text{on} \quad \Gamma^-\},$$

$$W_\phi = \{\phi \in H^1(\Omega) \mid \phi = \phi_0(t) \quad \text{on} \quad \Gamma^-\},$$

$$W_{\phi 0} = \{\phi \in H^1(\Omega) \mid \phi = 0 \quad \text{on} \quad \Gamma^-\},$$

$$L_0^2(\Omega) = \{q \in L^2(\Omega) \mid \int_\Omega q \, d\mathbf{x} = 0 \} \tag{4.9}$$

where Γ^- is the upstream part of Γ. It is easy to show that the following weak formulation of the problem holds for the two-phase system:

For a.e. $t>0$, find $\mathbf{u} \in W_u$, $\mathbf{A} \in W_A$, $p \in L_0^2(\Omega)$ and $\phi \in W_\phi$, satisfying

$$\int_\Omega \rho\left(\frac{d\mathbf{u}}{dt} - \mathbf{g}\right) \cdot \mathbf{v} d\mathbf{x} - \int_\Omega p \nabla . \mathbf{v} \, d\mathbf{x} + \int_\Omega 2\eta_s \mathbf{D}[\mathbf{u}] : \mathbf{D}[\mathbf{v}] d\mathbf{x} - \int_\Omega \mathbf{v} . \nabla . \left(\frac{c}{\lambda_r}\mathbf{A}\right) d\mathbf{x}$$
$$- \int_\Omega \gamma \kappa \delta(\phi) \mathbf{n} \cdot \mathbf{v} \, d\mathbf{x} = 0$$

$$\text{for all } \mathbf{v} \in W_{u0}, \tag{4.10}$$

$$\int_\Omega q \nabla . \mathbf{u} \, d\mathbf{x} = 0$$

$$\text{for all } q \in L^2(\Omega), \tag{4.11}$$

$$\mathbf{u}|_{t=0} = \mathbf{u}_o \text{ in } \Omega, \tag{4.12}$$

$$\int_\Omega \left(\frac{\partial \mathbf{A}}{\partial t} + \mathbf{u} \cdot \nabla \mathbf{A} - \mathbf{A} \cdot \nabla \mathbf{u} - \nabla \mathbf{u}^T \cdot \mathbf{A} + \frac{1}{\lambda_r}(\mathbf{A} - \mathbf{I})\right) \cdot \mathbf{s} \, d\mathbf{x} = 0$$

$$\text{for all } \mathbf{s} \in W_{A0}, \tag{4.13}$$

$$\mathbf{A}|_{t=0} = \mathbf{A}_o \qquad \text{in } \Omega, \tag{4.14}$$

$$\int_\Omega \left(\frac{\partial \phi}{\partial t} + \mathbf{u} \cdot \nabla \phi \right) g \, d\mathbf{x} = 0 \tag{4.15}$$

$$\text{for all } g \in W_{\phi 0},$$

$$\phi|_{t=0} = \phi_0 \qquad \text{in } \Omega.$$

4.5 Finite-Element Approximation

In order to solve the above problem numerically, the domain is discretized using a regular finite element triangulation T_h for the velocity and configuration tensor, where h is the mesh size, and a regular triangulation T_{2h} for the pressure. The following finite dimensional spaces are defined for approximating W_u, W_{u0}, W_A, W_{A0}, $L^2(\Omega)$, $L^2_0(\Omega)$, W_ϕ and $W_{\phi 0}$:

$$W_{u,h} = \{\mathbf{v}_h \in C^0(\overline{\Omega})^2 \mid \mathbf{v}_h|_T \in P_1 \times P_1 \text{ for all } T \in T_h, \mathbf{v}_h = \mathbf{u}_{\Gamma,h} \text{ on } \Gamma\}$$

$$W_{0,h} = \{\mathbf{v}_h \in C^0(\overline{\Omega})^2 \mid \mathbf{v}_h|_T \in P_1 \times P_1 \text{ for all } T \in T_h, \mathbf{v}_h = 0 \text{ on } \Gamma\} \tag{4.16}$$

$$L^2_h = \{q_h \in C^0(\overline{\Omega}) \mid q_h|_T \in P_1 \text{ for all } T \in T_{2h}\}$$

$$L^2_{0,h} = \{q_h \in L^2_h \mid \int_\Omega q_h \, d\mathbf{x} = 0\} \tag{4.17}$$

$$W_{A,h} = \{\mathbf{s}_h \in C^0(\overline{\Omega})^3 \mid \mathbf{s}_h|_T \in P_1 \times P_1 \times P_1 \text{ for all } T \in T_h, \mathbf{s}_h = \mathbf{A}_{L,h} \text{ on } \Gamma^-\}$$

$$W_{A0,h} = \{\mathbf{s}_h \in C^0(\overline{\Omega})^3 \mid \mathbf{s}_h|_T \in P_1 \times P_1 \times P_1 \text{ for all } T \in T_h, \mathbf{s}_h = 0 \text{ on } \Gamma^-\} \tag{4.18}$$

$$W_{\phi,h} = \{g_h \in C^0(\overline{\Omega}) \mid g_h|_T \in P_1 \text{ for all } T \in T_h, g_h = \phi_{0,h} \text{ on } \Gamma^-\}$$

$$W_{\phi 0,h} = \{g_h \in C^0(\overline{\Omega}) \mid g_h|_T \in P_1 \quad \text{for all } T \in T_h, g_h = 0 \text{ on } \Gamma^-\} \tag{4.19}$$

$$W_{\phi R,h} = \{g_h \in C^0(\overline{\Omega}) \mid g_h|_T \in P_1 \quad \text{for all } T \in T_h, g_h = 0 \text{ on the interface}\} \tag{4.20}$$

Using these finite dimensional spaces, the following finite-element approximation to the Equations (4.10) - (4.14) is obtained:

Find $\mathbf{u}_h \in W_{u,h}$, $\mathbf{A}_h \in W_{A,h}$, $\phi_h \in W_{\phi,h}$ and $p_h \in L^2_{0,h}$, satisfying

$$\int_\Omega \rho_L \left(\frac{d\mathbf{u}_h}{dt} - \mathbf{g} \right) . \mathbf{v}_h d\mathbf{x} - \int_\Omega p_h \nabla . \mathbf{v}_h \, d\mathbf{x} + \int_\Omega 2\eta_s \mathbf{D}[\mathbf{u}_h] : \mathbf{D}[\mathbf{v}_h] d\mathbf{x} - \int_\Omega \mathbf{v}_h . \nabla . \left(\frac{c}{\lambda_r} \mathbf{A}_h \right) d\mathbf{x}$$
$$- \int_\Omega \gamma \kappa \delta(\phi) \mathbf{n} \cdot \mathbf{v} \, d\mathbf{x} = 0$$

$$\text{for all } \mathbf{v}_h \in W_{0,h},$$

$$\int_\Omega q_h \nabla . \mathbf{u}_h \, d\mathbf{x} = 0 \qquad \text{for all } q_h \in L^2_h,$$

$$\int_\Omega \left(\frac{\partial \mathbf{A}_h}{\partial t} + \mathbf{u}_h . \nabla \mathbf{A}_h - \mathbf{A}_h . \nabla \mathbf{u}_h - \nabla \mathbf{u}_h^T . \mathbf{A}_h + \frac{1}{\lambda_r} (\mathbf{A}_h - \mathbf{I}) \right) . \mathbf{s}_h \, d\mathbf{x} = 0$$

$$\text{for all } \mathbf{s}_h \in W_{A0,h},$$

$$\int_\Omega \left(\frac{\partial \phi_h}{\partial t} + \mathbf{u}_h . \nabla \phi_h \right) g_h d\mathbf{x} = 0$$

$$\text{for all } g_h \in W_{\phi 0,h},$$

$$\mathbf{u}|_{t=0} = \mathbf{u}_{0,h} \qquad \text{in } \Omega,$$

$$\mathbf{A}_h|_{t=0} = \mathbf{A}_{0,h} \text{ in } \Omega,$$

$$\phi|_{t=0} = \phi_{0,h} \text{ in } \Omega. \tag{4.21}$$

4.6 Time Discretization Using the Marchuk-Yanenko Operator Splitting Scheme

The initial value problem (Equation 4.21) is solved by using the Marchuk-Yanenko operator splitting scheme which allows us to decouple its four primary difficulties:

1. The incompressibility condition, and the related unknown pressure p_h,

2. The nonlinear advection term,

3. The interface problem, and the related unknown level set distribution ϕ_h

4. The equation for the configuration tensor, and the viscoelastic stress tensor which appears in the momentum equation.

The Marchuk-Yanenko operator splitting scheme can be applied to an initial value problem of the form

$$\frac{d\phi}{dt} + A_1(\phi) + A_2(\phi) + A_3(\phi) + A_4(\phi) = f$$

where the operators A_1, A_2, A_3, and A_4 can be multiple-valued. Let Δt be the time step, and α, β and γ be three constants: $0 \le \alpha, \beta, \gamma \le 1$ and $\alpha + \beta + \gamma = 1$. We use the following version of the Marchuk-Yanenko operator splitting to simulate the motion of particles in a viscoelastic fluid:

$$\text{Set } \mathbf{u}^0 = \mathbf{u}_{0,h},\ \mathbf{A}^0 = \mathbf{A}_{0,h}, \text{ and } \phi^0 = \phi_{0,h}.$$

For n=0,1,2,... assuming $\mathbf{u}^n$, $\mathbf{A}^n$, and ϕ^n are known, find the values for n+1 using the following:

STEP 1:

Find $\mathbf{u}^{n+1/4} \in W_{u,h}$ and $p^{n+1/4} \in L^2_{0,h}$, by solving

$$\int_\Omega \rho \frac{\mathbf{u}^{n+1/4} - \mathbf{u}^n}{\Delta t}.\mathbf{v}\,dx - \int_\Omega p^{n+1/4} \nabla.\mathbf{v}\,dx + \alpha \int_\Omega 2\eta_s \mathbf{D}[\mathbf{u}^{n+1/4}] : \mathbf{D}[\mathbf{v}]dx$$
$$= \int_\Omega \mathbf{v}.\nabla.\left(\frac{c}{\lambda_s}\mathbf{A}^n\right)dx + \int_\Omega \gamma\kappa\delta(\phi)\mathbf{n}\cdot\mathbf{v}\,dx$$

for all $\mathbf{v} \in W_{0,h}$,

$$\int_\Omega q\nabla.\mathbf{u}^{n+1/4}dx = 0 \qquad \text{for all } q \in L^2_h, \tag{4.22}$$

STEP 2:

Find $\mathbf{u}^{n+2/4} \in W_{u,h}$, by solving

$$\int_\Omega \rho \frac{\mathbf{u}^{n+2/4} - \mathbf{u}^{n+1/4}}{\Delta t}.\mathbf{v}dx + \int_\Omega \rho_L(\mathbf{u}^{n+2/4}.\nabla\mathbf{u}^{n+2/4}).\mathbf{v}\,dx + \beta\int_\Omega 2\eta_s \mathbf{D}[\mathbf{u}^{n+2/4}] : \mathbf{D}[\mathbf{v}]dx = 0$$

for all $\mathbf{v} \in W_{0,h}$, (4.23)

STEP 3:

Find $\mathbf{A}^{n+3/4} \in W_{A,h}$, by solving

$$\int_\Omega \left(\frac{\mathbf{A}^{n+3/4} - \mathbf{A}^n}{\Delta t} + \mathbf{u}^{n+2/4}.\nabla\mathbf{A}^{n+3/4} - \mathbf{A}^{n+3/4}.\nabla\mathbf{u}^{n+2/4} - (\nabla\mathbf{u}^{n+2/4})^T.\mathbf{A}^{n+3/4} + \frac{1}{\lambda_r}(\mathbf{A}^{n+3/4} - \mathbf{I})\right).\mathbf{s}dx = 0$$

for all $\mathbf{s} \in W_{A0,h}$, (4.24)

STEP 4:

Find $\phi^{n+4/4} \in W_{\phi,h}$, by solving

$$\int_\Omega \left(\frac{\phi^{n+4/4} - \phi^n}{\Delta t} + \mathbf{u}^{n+2/4}.\nabla\phi^{n+4/4}\right) g_h dx = 0$$

$$\text{for all } g_h \in W_{\phi 0,h}. \tag{4.25}$$

$$\text{Set } \mathbf{u}^{n+1} = \mathbf{u}^{n+2/4},\ \mathbf{A}^{n+1} = \mathbf{A}^{n+3/4},\ p^{n+1} = p^{n+1/4},\ \phi^{n+1} = \phi^{n+4/4}.$$

STEP 5:

Reinitialize ϕ^{n+1}

$$\text{Set } \phi_R^0 = \phi^{n+1}$$

$$\text{For } r = 0, 1, 2, \ldots$$

$$\mathbf{w}^r = S(\phi^{n+1}) \frac{\nabla \phi_R^r}{\left| \nabla \phi_R^r \right|}$$

$$\text{Find } \phi_R^{r+1} \in W_{\phi R,h}, \text{ by solving}$$

$$\int_\Omega \left(\frac{\phi_R^{r+1} - \phi_R^r}{\Delta t} + \mathbf{w}^r . \nabla \phi_R^r \right) g_h \, d\mathbf{x} = \int_\Omega S(\phi^{n+1})\, g_h \, d\mathbf{x}$$

$$\text{for all } g_h \in W_{\phi R,h}. \tag{4.26}$$

go back to the above for loop.

Set $\phi^{n+1} = \phi_R^{r+1}$ and go back to the first step.

Remarks:

1. The first step gives rise to a Stokes-like problem for the velocity and pressure distributions which is solved by using a conjugate gradient method [Glowinski et al. (1992)].

2. The second step is a nonlinear problem for the velocity, which is solved by using a least square conjugate gradient algorithm [Bristeau et al. (1987)].

3. The third step is a linearized hyperbolic problem for the configuration tensor or stress. This problem is solved by using a third order upwinded positive only scheme [Singh and Leal (1993)]. The two key features of this scheme are: a positive only scheme that guarantees the positive definiteness of the configuration tensor, and a third order upwinding scheme for discretizing the convection term in the constitutive equation. These two features are important for obtaining a scheme that is stable at relatively large Deborah numbers.

4. The fourth step is a hyperbolic problem for the scalar level set function ϕ. This problem is solved by using a upwinding scheme where the convection term is discretized using a third order scheme [Singh and Leal (1993)]. After advecting ϕ, the distance function is reinitialized to be a distance function near the interface by performing two iterations of Equation 4.26.

CHAPTER 5

RESULTS AND DISCUSSION-SIMPLE SHEAR FLOW

5.1 Introduction

Numerical simulations were carried out in two dimensions as well as three dimensions. The results of the two-dimensional simulation will be discussed first which will be followed by results of three-dimensional simulations. Though a two-dimensional analysis brings out many aspects of deformation of drops in viscoelastic flows, a three-dimensional analysis becomes imperative due to the asymmetric nature of the problem. Even when both fluids involved are Newtonian, the deformed drop shape is not symmetrical. When one or both of the liquids involved are viscoelastic the drop asymmetry is greater which is due to the development of viscoelastic stress boundary layers near the interface that are not symmetrically located about the major axis of the deformed drop. Therefore, strictly speaking, for understanding the deformation and breakup of drops in viscoelastic simple shear flows, simulations must be performed in three dimensions. The effect of different parameter on the shape of the drop will however be discussed in both two the three dimensions.

The deformation of a drop in both two and three-dimensional case is measured in terms of the Taylor deformation parameter $D=\frac{L-B}{L+B}$, where L is half the major axis and B is half the minor axis of the ellipsoidal drop. Before flow is imposed, the drop is spherical and the deformation parameter D = 0. The value of D ranges between zero and one depending on the extent of deformation.

Before discussing the results, it is worth repeating here that the Deborah number, a dimensionless measure of the viscoelastic stresses is defined as $De = \lambda_r G$, where λ_r is the relaxation time of the fluid and G is the shear rate (for simple shear flow). c is a measure of polymer concentration in terms of the zero shear viscosity. The zero shear viscosity $\eta_o = \eta_s + \eta_p$, where $\eta_p = c\eta_s$ is the polymer contribution to viscosity. The Capillary number $Ca = G\eta_L a/\gamma$, where a is the radius on the drop, η_L is the viscosity of the matrix liquid and γ is the interfacial tension.

The polymer response, as it travels on any of the streamlines will depend on the strain rate, flow type at each point in the flow and the strain rate history experienced prior to that point [Szeri, et al. (1988)]. To understand the polymer response to flow type, it is useful to define two quantities. The tr**A** i.e. the trace of the configuration tensor **A** is a measure of the extension of the polymer molecule. In its relaxed state when **A** = **I**, the tr**A** will be 2 for the two-dimensional case and 3 for the three-dimensional case. Another quantity that helps us visualize the effect of viscoelasticity is the component of viscoelastic force plotted along the outer normal. This is obtained by taking the normal component of the viscoelastic contribution to the momentum balance equation, i.e. $\mathbf{n}\cdot\left(\nabla\cdot\left(\frac{c}{\lambda_r}\mathbf{A}\right)\right)$, where **n** is the outer normal. A positive value of this quantity indicates that the forces act in the direction of the outer normal and a negative value indicated that the force acts in the opposite direction.

The orientation of the principle Eigen vector of **A** is another useful feature that helps understand the directional orientation of the polymer molecules. Each of the above feature will be used to provide a basis for comparing flows of different types.

5.2 Results of Two-Dimensional Simulations

5.2.1 Convergence with mesh refinement for two-dimensional simulations

The code was verified by performing a convergence study that shows that the steady state shape of the drop is independent of the mesh resolution and also of the time step used in calculations. The time step is varied between 0.001 and 0.0005.

Simulations are started by placing a circular drop of diameter 1 at t = 0 at the center of the computational domain where it is subjected to a viscoelastic simple shear flow of strength 0.4 /s. The fluid viscosity is 300 and $\lambda = 1$. The relaxation time of the fluid is 1, and the surface tension is 250. For the above parameters, Re = 0.0003, De = 0.4, and Ca = 0.24. As will be discuss later, for these parameter values the drop attains a steady state shape.

From Table 5.1 it is worth noting that when the number of nodes is increased from 9129 to 11567, and further to 17493, the steady state deformation as well as the drop area is comparable. The drop area for the finest mesh is ~1.5% smaller than the initial area. The mesh was refined such that in all three cases the elements near the interface were 4 times smaller than the elements farther away. For a mesh with 17493 nodes the drop area and deformation are shown in Table 5.2 for two different values of the time step. From the results presented above it is established that the steady state results are also approximately independent of the time step. The time evolution curves of the drop shape shown in Figure 5.1 for two different values of time step and mesh resolution are also approximately identical. From the aforementioned results and discussions it may be concluded that both the transient and the steady state solutions are independent of the mesh resolution and the time step used.

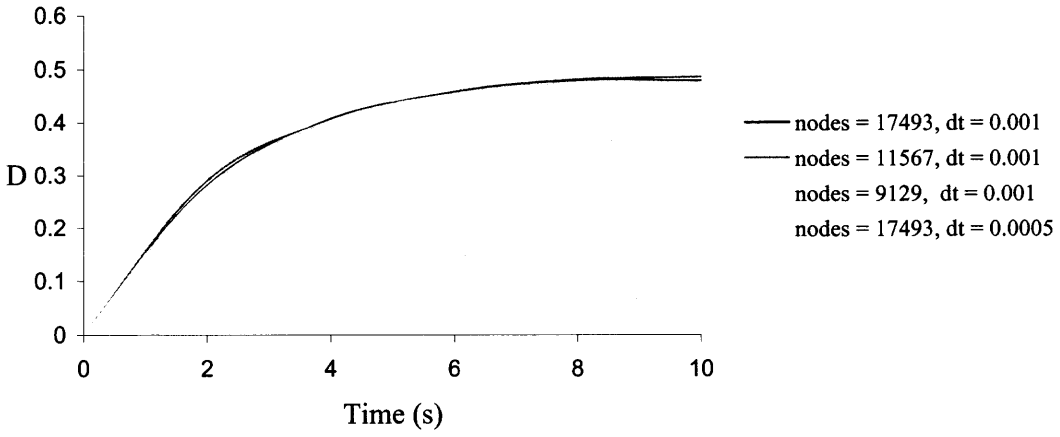

Figure 5.1 Transient deformation of a Newtonian drop in a viscoelastic shear flow for Ca = 0.24, De = 0.4 and Re = 0.0003. The drop attains a stable approximately elliptical shape. The figure shows that for varying resolution and time step the final deformations as well as transient deformations are approximately the same.

For the simple shear flow problem, simulations were convergent for flows up to De = 16. The method converges for Re < O(1000), including Stokes flow (Re = 0). The Reynolds number for most cases described in this paper is much smaller than one and is approximately of the same order as for results described in [Pillapakkam and Singh (2001)].

Number of nodes	Deformation D	Drop area
9129	0.4758	0.7387
11567	0.4863	0.7327
17493	0.4779	0.7694

Table 5.1 Drop deformation and area for a Newtonian drop subjected to viscoelastic simple shear flow for three different mesh resolutions. The time step size is 0.0001, Ca = 0.24, Re = 0.0003 and De = 0.4.

Time step	Deformation D	Drop area
0.0005	0.4749	0.7659
0.001	0.4779	0.7694

Table 5.2 Drop deformation and area for a Newtonian drop subjected to viscoelastic simple shear flow for two different values of time step. The number of nodes is 17493, Ca = 0.24, Re = 0.0003 and De = 0.4.

5.2.2 Deformation of a Newtonian Drop in a Simple Shear Flow of a Viscoelastic fluid

In this section results are presented for the case when the drop phase is Newtonian and the matrix phase is viscoelastic. To demonstrate the behavior of polymer molecules, a drop with initial diameter 1 is subjected to a simple shear flow of strength 0.4 s^{-1}. The fluid viscosity is 300 and the viscosity ratio $\lambda = 1$. For the above parameters, the dimensionless Ca = 0.4, De = 0.6 and the Reynolds number is 0.0003.

In simple shear flow, the polymer molecules experience considerable degree of stretch along the principle axis of deformation close to the interface as can be seen from the isovalues of tr**A** (See Figure 5.2). This is because for a fixed non-homogeneous

spatial distribution of velocity gradient tensor along a streamline, the spatial gradient of the velocity gradient tensor along a streamline, the spatial gradient of the configuration tensor increases as the transnational velocity of the polymer molecules decreases [Singh and Leal (1993)].

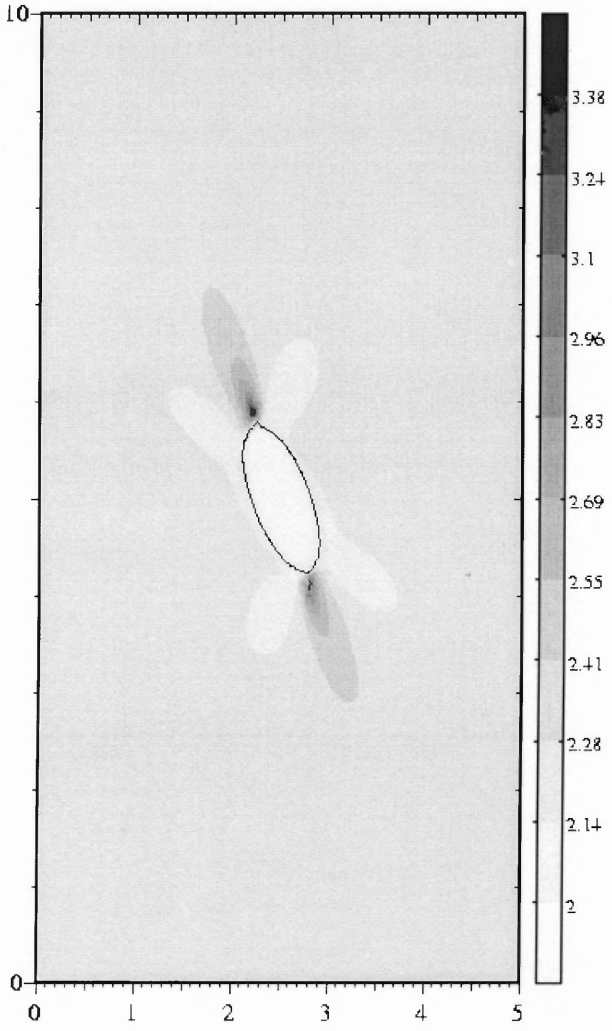

Figure 5.2 Isovalues of tr**A** are shown for the case of a Newtonian drop subjected to a viscoelastic shear flow with Ca = 0.24, De = 0.6 and Re = 0.0003. (a) The time step is 0.0001 and the number of nodes is 9129. The steady state deformation D = 0.4758.

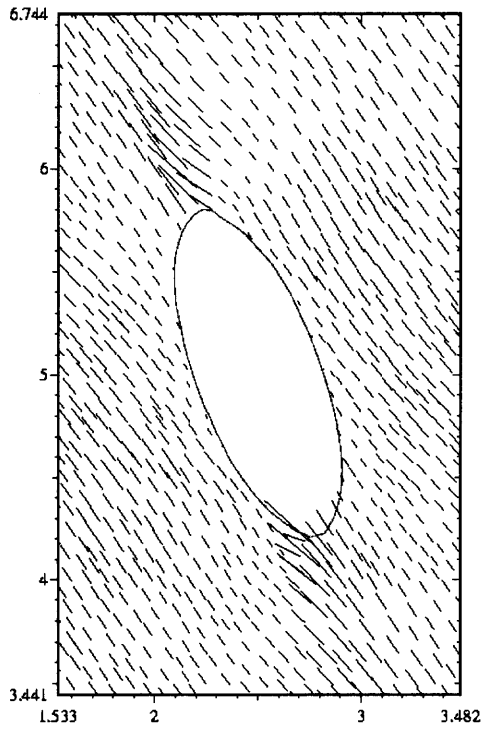

Figure 5.3 A magnified view of distribution of principal direction of **A** is shown. Notice that the viscoelastic stresses near the tip of major axis act in the direction approximately normal to the drop surface.

The orientation of the principal eigenvector of **A** is shown in Figure 5.3. Notice that the polymer molecules tend to align themselves along the principal axis of deformation that corresponds to a region of high strain. Also notice that the principal direction of viscoelastic stress is normal to the drop surface near the tips of the major axis and parallel to the drop surface at the tips of the minor axis. The viscoelastic polymer molecules have a tendency to align and stretch along regions in the flow that are extensional in nature. The normal component of viscoelastic stresses locally pull out the drop surface, leading to the formation of pointed edges.

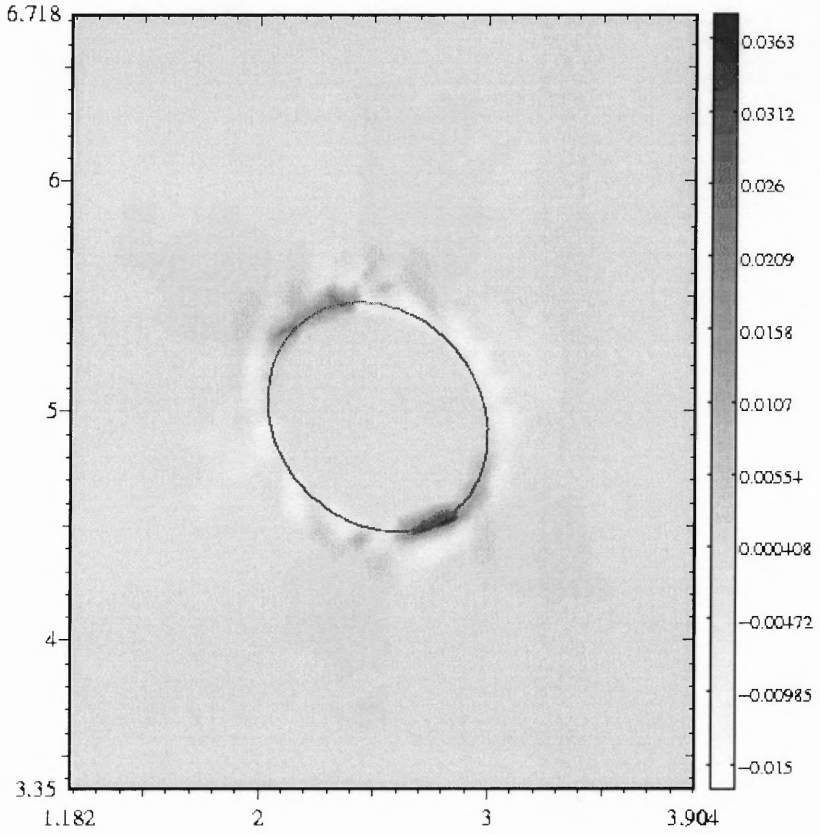

Figure 5.4 Isovalues of the normal component of viscoelastic stress are shown for a Newtonian drop subjected to viscoelastic shear flow. The normal component of the viscoelastic stresses is positive and extensional near the tip but negative near the equator.

Figure 5.4 shows isovalues of the normal component of viscoelastic stress for a Newtonian drop subjected to a viscoelastic simple shear flow. The dark region along the principal axis of the drop indicates that viscoelastic stresses in that region are positive and act away from the center. The lighter region in the direction normal to the principal axis of the drop indicates that the viscoelastic stresses act inwards. Clearly, the combined effect of the viscoelastic stress is to increase the drop deformation from that for the corresponding Newtonian case.

The effect of increase in De on drop deformation will be explained while discussing the results of three-dimensional simulation. However, it is worth noting that the contribution of the normal component of the viscoelastic stress increases with increase in De as can be seen from Figure 5.5.

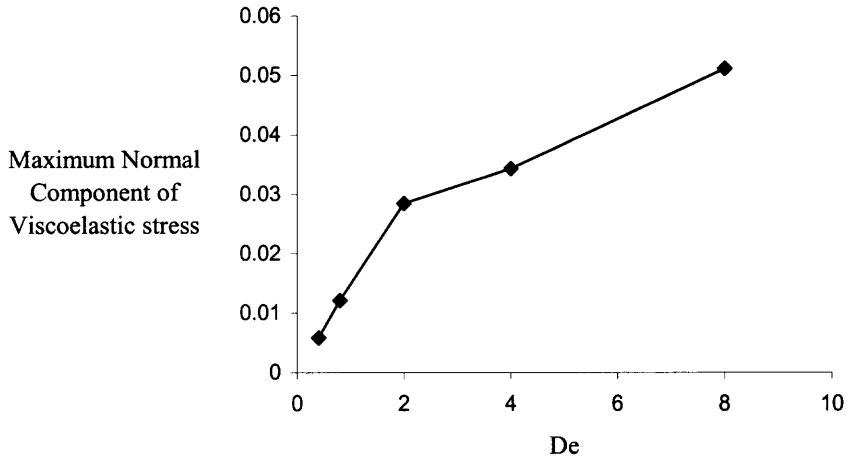

Figure 5.5 The maximum of the normal component of viscoelastic stress as a function of De at Ca = 0.24.

5.2.3 Deformation of a Viscoelastic Drop in a Simple Shear Flow of a Newtonian Fluid

In this section the behavior of a viscoelastic drop subjected to a simple shear flow of a Newtonian fluid is discussed. The drop diameter is 1 and the shear rate 0.4 /s. The fluid viscosity is 300 and $\lambda = 1$. The Reynolds number is 0.0016.

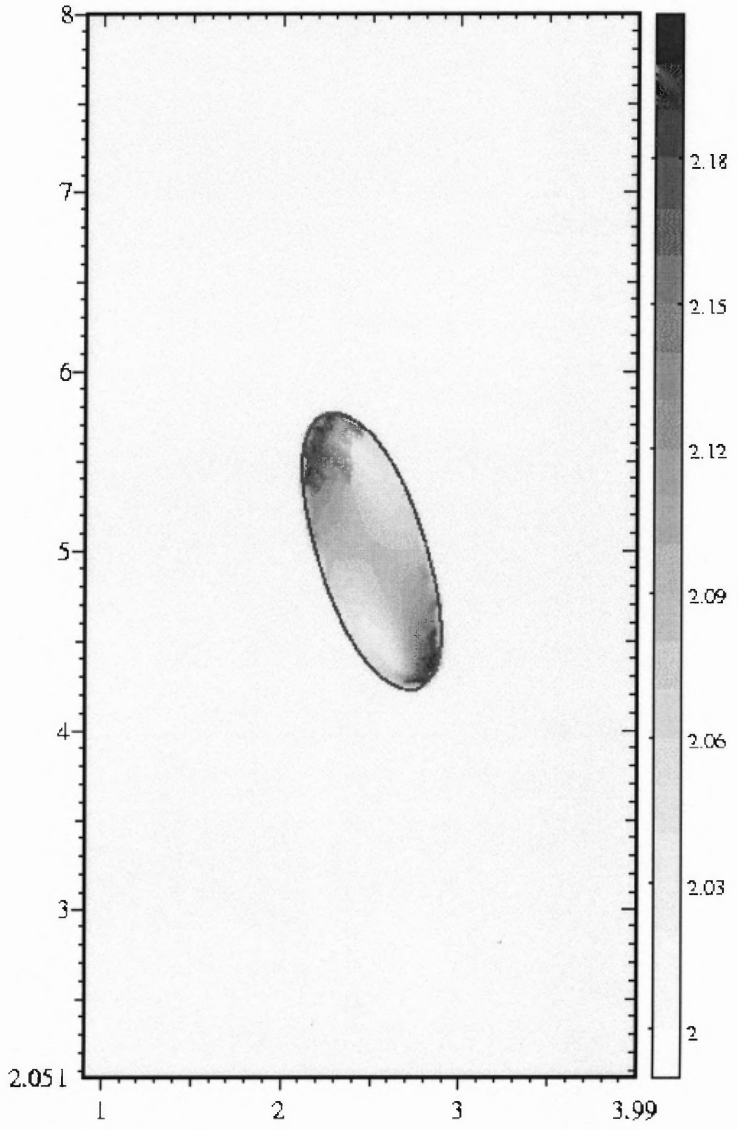

Figure 5.6 Isovalues of tr**A** for a viscoelastic drop in a simple shear flow of a Newtonian fluid at steady state. The time step used is 0.001. For Ca = 0.6, De = 0.4, and Re = 0.0003, deformation D = 0.4675.

From Figure 5.6 it can be seen that for Ca = 0.6 and De = 0.4, the distribution of tr**A** is not symmetrical about the major axis. The thin boundary layers of high velocity gradients exist inside the drop where tr**A** is relatively large. However it is not symmetrically located about the major axis. Due to this asymmetry of viscoelastic

stresses the deformed drop is not exactly symmetric about the major axis and therefore a two dimensional analysis is insufficient for a complete analysis of the deformation of drops involving viscoelastic fluids. Also notice that, just as in the case of Newtonian drop in viscoelastic shear flow, the maximum value of tr**A** is near the tip of the major axis.

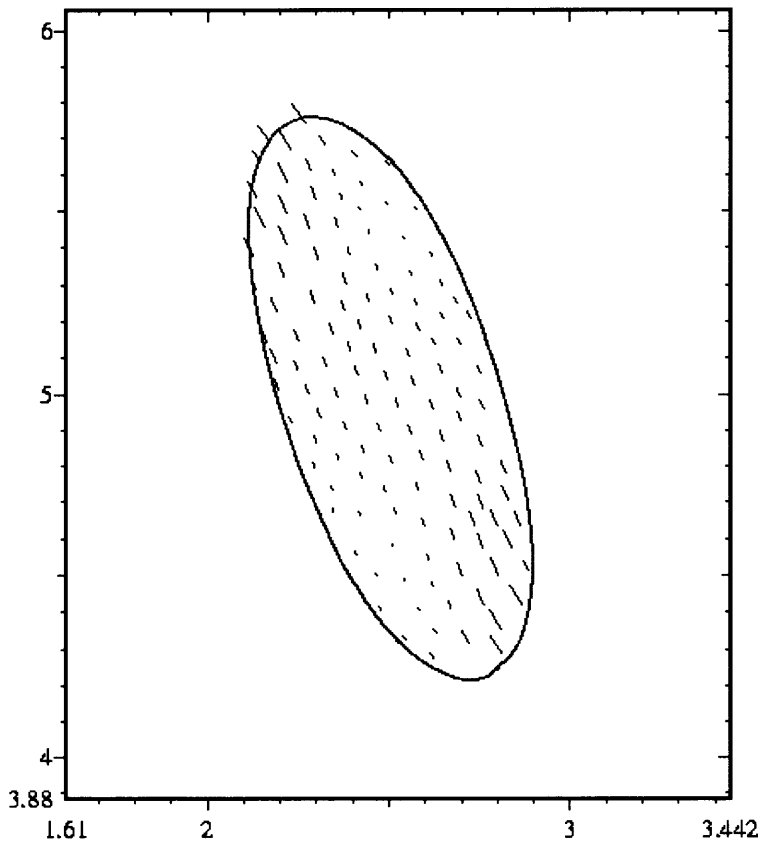

Figure 5.7 A magnified view of distribution of principal direction of **A** is shown for the case described in Figure 5.6.

As seen in Figure 5.7, the orientation of the principal eigenvector of **A** for the fluid inside the drop is normal to the drop surface near the tips of the major axis and this pulls the drop inwards as can be seen from Figure 5.8. The dark region along the normal to the principal axis of the drop indicates that the viscoelastic stresses in that region are

positive and act away from the center. The lighter region near the tip of the major axis indicates that the viscoelastic stresses are negative and this act inwards and the combined effect results in deformation that are smaller than for a corresponding Newtonian drop.

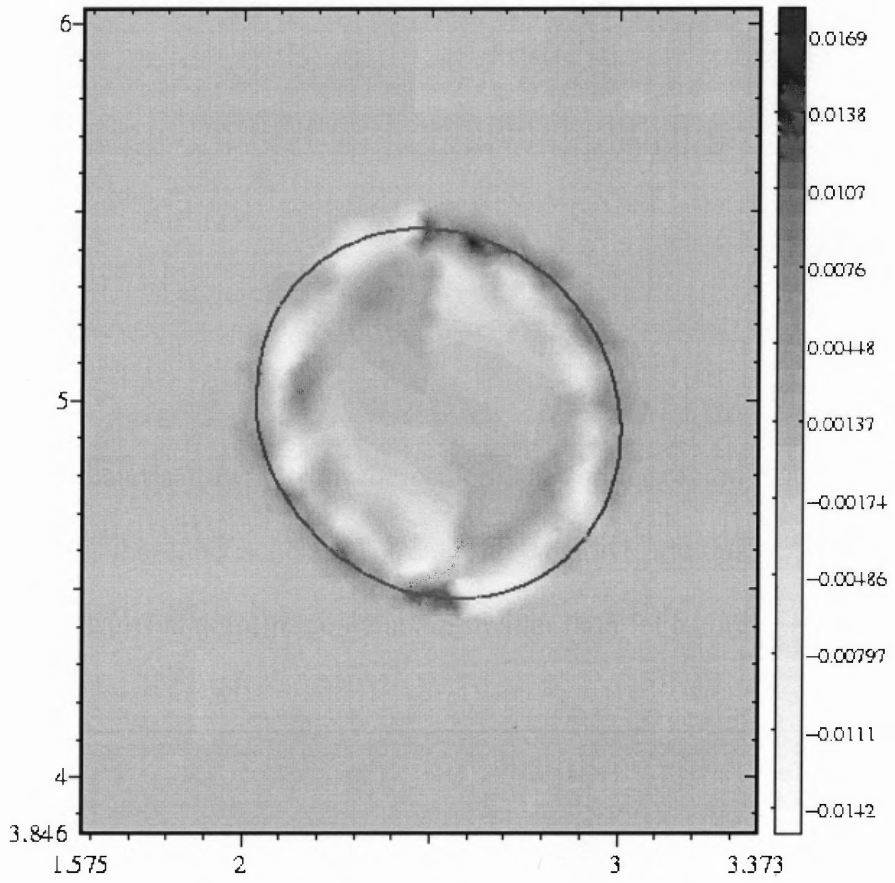

Figure 5.8 Iso-values of the normal component of viscoelastic stress near the interface. The dark region near the tip of the major axis of the deformed drop indicates that viscoelastic stress in this region is positive and acts away from the center. The lighter region near the tip of the minor axis of the deformed drop indicates negative viscoelastic stresses that act inwards.

Also note from Figure 5.9 that, as in the case of a Newtonian drop in a viscoelastic simple shear flow, the maximum value of the normal component of viscoelastic stress increases with increase in De.

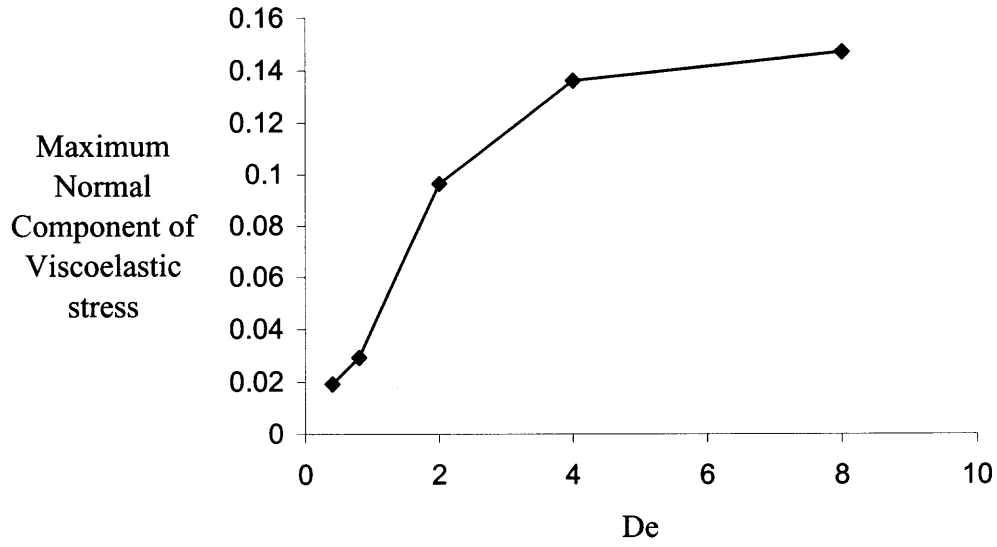

Figure 5.9 The maximum of the normal component of viscoelastic stress as a function of De at Ca = 0.6.

5.3 Results of Three-Dimensional Simulations

The primary goal of this analysis of drop deformation is to analyze the effect of viscoelastic stress on the in drop shape that result from independently varying the polymer concentration c and the polymer relaxation time λ_r.

Simulations were carried out for a range of Ca, De and *c*. Since only the steady state shapes are analyzed, the choice of Ca, De and *c* are restricted to values that yield steady state shapes. Even though the numerical code is capable of handling transient deformation and drop breakup, the results discussed are limited to steady state deformations since greater emphasis is on the effect of viscoelasticity on deformation and not on qualitative nature of deformation or modes of break up. The viscosity ratio will be

restricted to 1 throughout this chapter. Figure 5.10 shows an undeformed drop at the center of the domain before flow is imposed on the drop.

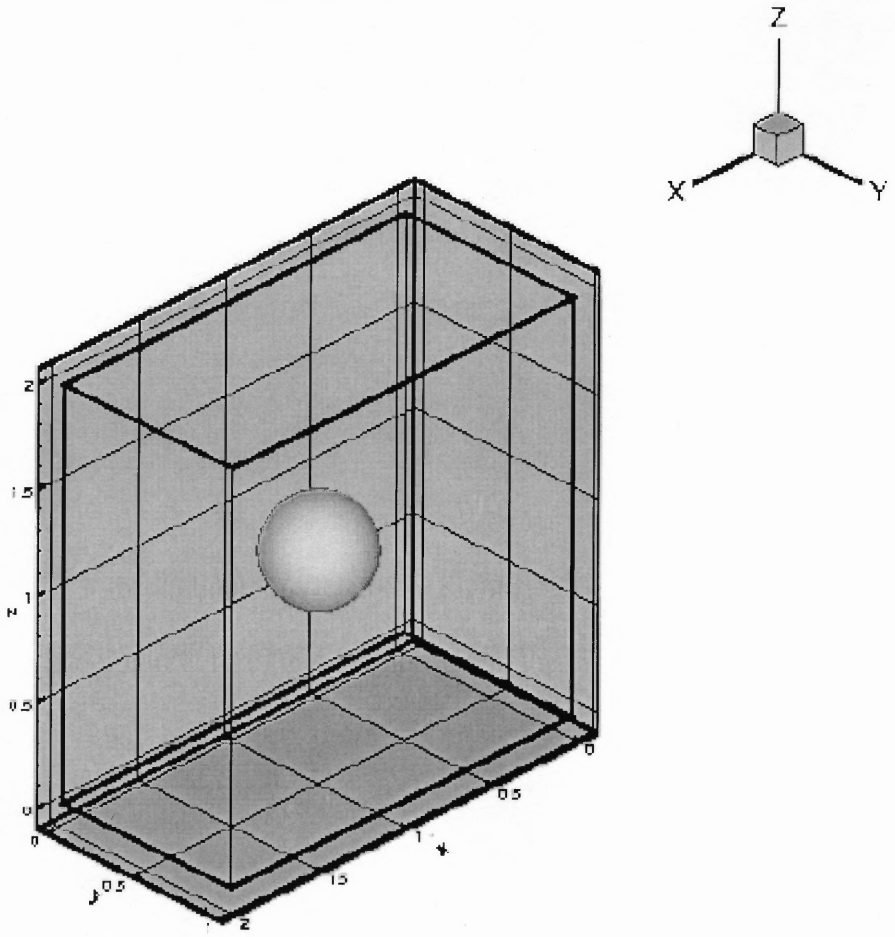

Figure 5.10 An undeformed drop of radius 0.25 in a domain of size 2 x 1 x 2. Simple shear flow is generated by moving the walls in the Y-Z plane in opposite directions.

5.3.1 Convergence and Comparison

The code was verified by performing a convergence study that shows that the steady state shape of the drop is independent of the mesh resolution and also of the time step used in calculations as shown in Figure 5.11. The time step is varied between 0.001 and 0.0005.

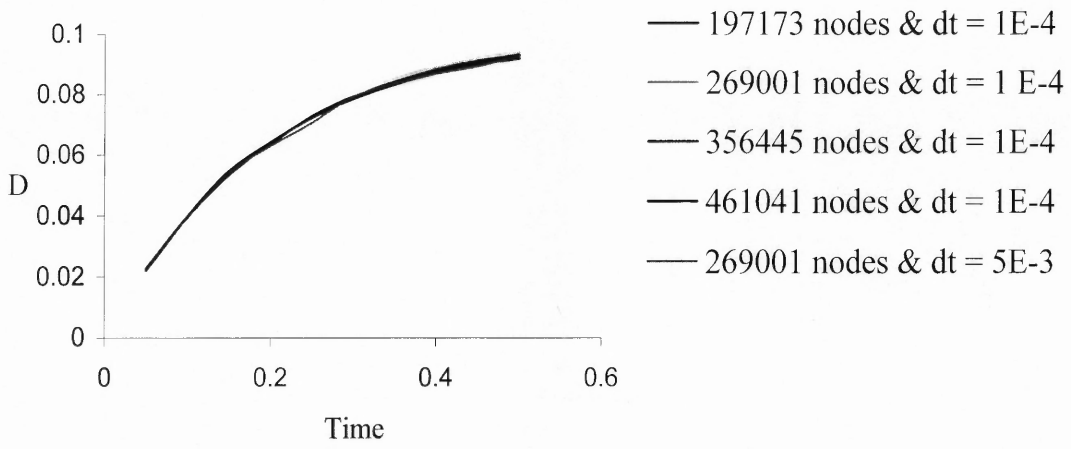

Figure 5.11 Transient deformation of a Newtonian drop subjected to viscoelastic simple shear flow for Ca = 0.1, De = 0.1, c = 0.1. The figure shows that for varying resolutions and time steps the transient deformations are approximately the same.

The result of the convergence test indicates that the three-dimensional numerical scheme is independent of resolution as well as time step sizes.

Since the deformation of drops when both phases involved are Newtonian is a problem that has been analyzed experimentally as well as numerically, comparisons could be drawn to verify accuracy of the numerical scheme as shown in Figure 5.12 where the steady state drop deformation parameter D is shown as a function of Ca. The above plot shows results obtained using the Volume of fluid method by Li, et al. (2000),

boundary integral computations of Rallison (1984), experimental results by Rumscheidt and Mason (1961) and boundary integral computations of Kwak, et al.(1998).

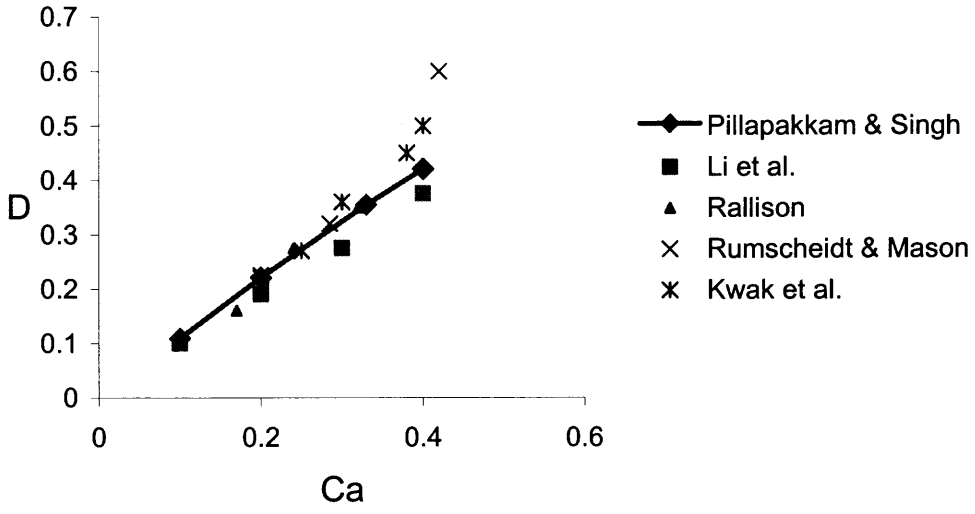

Figure 5.12 Deformation of a Newtonian drop in a Newtonian simple shear flow. The steady state drop deformation parameter D is shown for the volume of fluid method by Li, et al. (2000), boundary integral computations of Rallison (1984), experimental results by Rumscheidt and Mason (1961) and boundary integral computations of Kwak, et al. (1998).

5.3.2 Deformation of a Newtonian Drop in a Simple Shear Flow of a Viscoelastic Fluid

As already mentioned, the results are restricted to the parameter range for which the drops deform to steady state shapes. The parameters that will be varied are, Ca, De and c. In simulations, the capillary number is varied by varying the interfacial tension acting at the interface of the two fluids while keeping the shear rate a constant. Simulations were performed for Ca = 0.1 and 0.13, with polymer concentrations ranging from c = 0.01 to 1 and for a set of De between 0.01 and 3. The viscosity ratio is taken to be unity.

5.3.2.1 Effect of Polymer Concentration *c*

At extremely low concentration levels, even though the polymer molecules stretch in flow, the change in strain rates is not very significant. Therefore, at very low polymer concentration levels, the fluid behaves like a Newtonian fluid regardless of the fluid relaxation time.

In Figure 5.13, tr**A**, a dimensionless measure of the extent to which the polymer molecules are stretched relative to their equilibrium radius of gyration is plotted against De for two different values of polymer concentrations. For these calculations, Ca = 0.1.

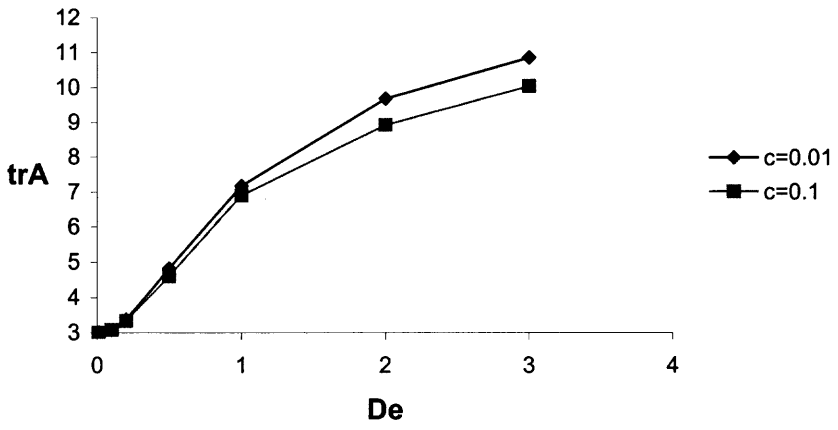

Figure 5.13 tr**A** is plotted against De for two different polymer concentrations, Ca = 0.1.

Notice that tr**A** is larger for the smaller concentration. As polymer concentration increases, the maximum value of tr**A** and thus also the maximum polymer extension decreases. At low *c*'s, though the polymer molecules exhibit a high degree of stretch, its effect on the flow and the drop deformation is not significant. For example, the deformation of a Newtonian drop in a simple Newtonian shear flow at Ca = 0.1 is

$D_{Newtonian}$ = 0.09730, while that of a Newtonian drop in a viscoelastic shear flow at c = 0.01 and Ca = 0.1 is $D_{viscoelastic}$ = 0.09926. It is justifiable to say that the viscoelastic contribution is not very significant as $c \rightarrow 0$. As c increases, the viscoelastic contribution to flow becomes significant and drop deformation increases as seen in Figure 5.14.

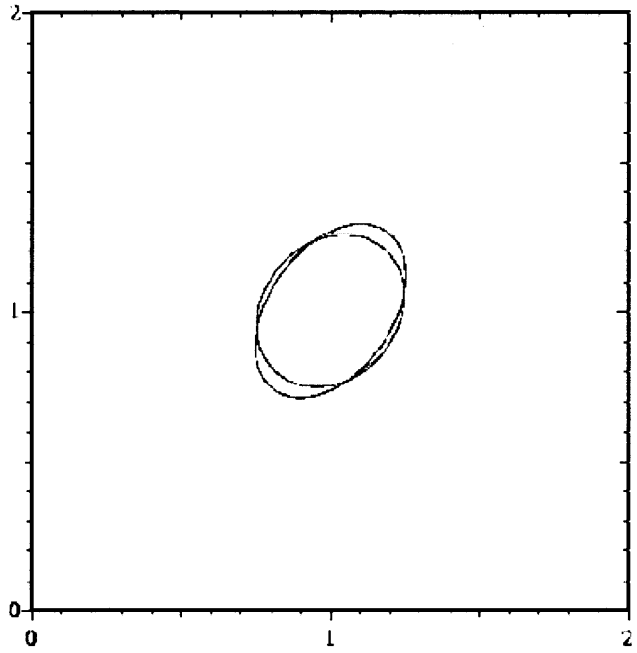

Figure 5.14 Steady state drop shapes for c = 0.01 and c = 1 at Ca = 0.1 and De = 0.01. The deformation parameter, $D_{c=1}$ = 0.2250, while $D_{c=0.01}$ = 0.09926.

5.3.2.2 Effect of Deborah Number De

It is known that in the limit of De$\rightarrow$ 0, the fluid behaves like a Newtonian liquid and that the viscoelastic effects become significant only when De $\cong$ 1.

To study the effect of De on the deformation of drops, simulations were performed for a range of De from 0.01 to 3 for Ca = 0.1 and 0.13. From Figure 5.13 it can be seen that tr**A** increases with increase in De, but decreases with increase in c. Though

the deformation of drops in viscoelastic shear flows is always greater than in Newtonian shear flow (for a given Ca), the deformation of a Newtonian drop in viscoelastic shear flow decreases with increase in De. When zero-shear viscosity is maintained constant, the deviation from Newtonian behavior varies as a function of c as can be seen from Figures 5.15 and 5.16.

A couple of interesting observations from the above results are that even at extremely low values of De the deviation from Newtonian behavior is very significant, provided the value of c is not small. Only in the limit of $c \rightarrow 0$ and $De \rightarrow 0$ does the drop deformation in a viscoelastic fluid approaches that in a Newtonian liquid. Secondly, the deviation from Newtonian behavior also increases with increase in Ca.

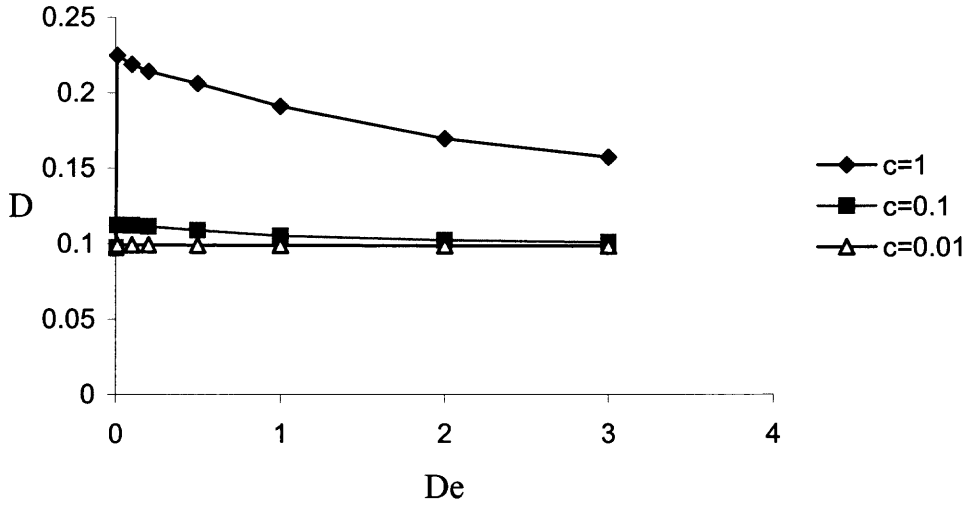

Figure 5.15 Drop deformation parameter D is shown as a function of De for different values of polymer concentration c. Ca = 0.1 and η_o = 10.25 Poise. The corresponding value of Newtonian deformation is a point on the y-axis $D_N = 0.0973$.

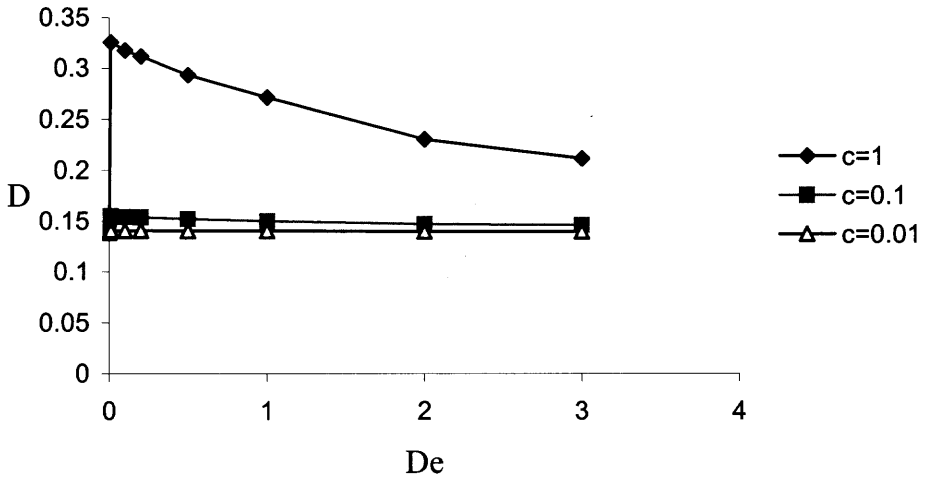

Figure 5.16 Drop deformation parameter D is shown as a function of De for different values of polymer concentration *c*. Ca = 0.13 and η_o = 10.25 Poise. The corresponding value of Newtonian deformation is a point on the y-axis, $D_N = 0.1386$

It was observed in the two-dimensional case (See Figure 5.5) that the normal component of viscoelastic stress increases with increase in De. If one were to base an explanation for deformation of a drop based on normal viscoelastic stresses alone, as noted by Elmendorp and Maalcke (1985), such reasoning would not be able to account for a decrease in drop deformation with an increase in De. Clearly the modification in velocity field due to a reduction in the velocity gradients also plays an important role in determining drop deformation.

Another interesting feature that merits explanation is that with an increase in De, the maximum value of tr**A** is no longer near the tip of the major axis of the deformed drop. A comparison of the isovalues of tr**A** at two different values of De will reveal the difference in alignment of the eigen directions of **A** (see Figure 5.17 and Figure 5.18).

This shift in the location of maximum of tr**A** away from the tip of the major axis, cause an asymmetric deformation of the drop.

Finally, it is worth noting that at small values of c, the drop attained an ellipsoidal steady shape (See Figure 15.19). However, at larger c's (See Figure 15.20), the drop developed pointed ends and in simulations lost volume from the tips. The drops continued to deform and lose fluid and thus no steady state shapes were possible.

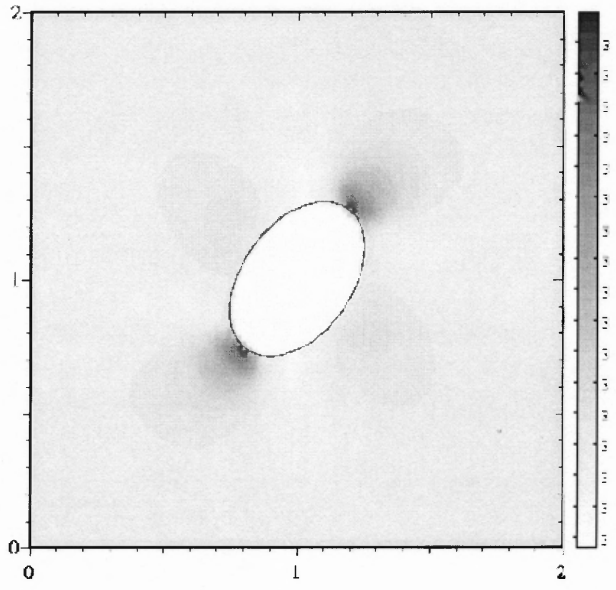

Figure 5.17 Isovalues of tr**A** at Ca = 0.1, De = 0.01 and c = 1. Note that the maximum value of trA is at the tip of the drop along the major axis of the drop.

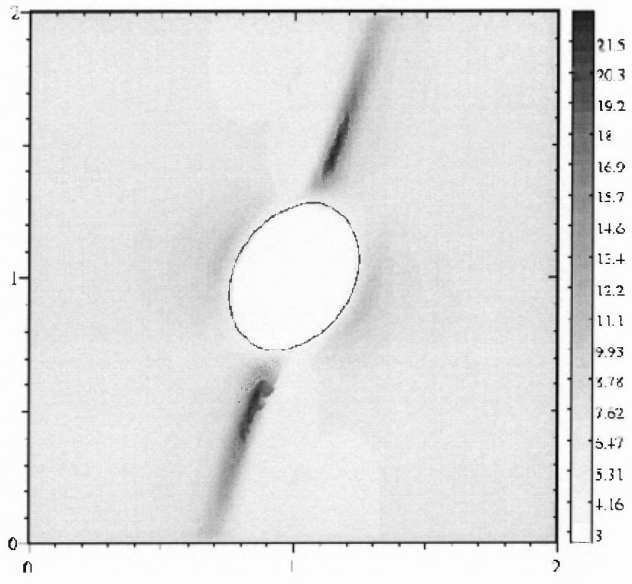

Figure 5.18 Isovalues of tr**A** at Ca = 0.1, De = 3 and c = 1. Note that the maximum value of trA is no longer along the major axis of the elliptical drop.

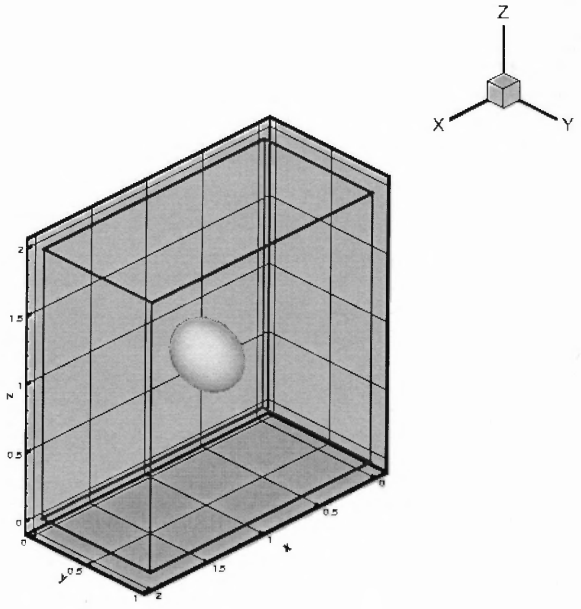

Figure 5.19 For small values of c, the drop attains a steady state shape. c = 0.1, Ca = 0.1, De = 1.

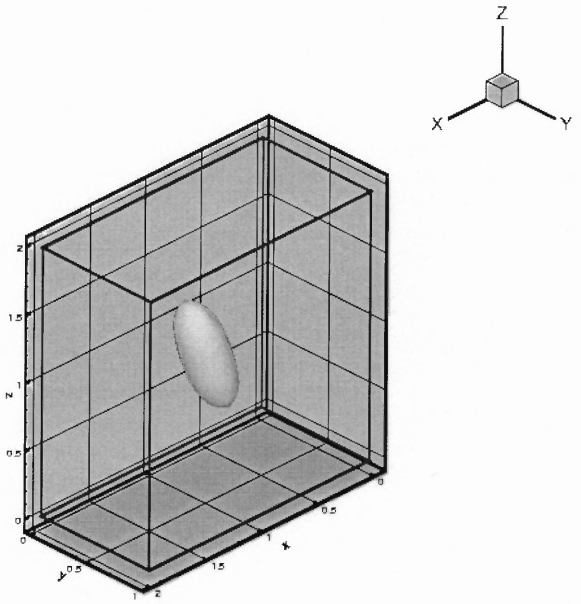

Figure 5.20 For large values of c, no steady state shapes were observed. The drop develops pointed ends and looses fluid from the tips. c = 5.0, Ca = 0.1 and De = 1.

5.3.3 Deformation of a Viscoelastic Drop in a Simple Shear Flow of a Newtonian Fluid

In this section we will look at the problem when drop phase is viscoelastic and matrix phase is Newtonian and analyze the variation in drop shape as a function of De and polymer concentration c. From discussions in previous sections it is known that viscoelasticity of the matrix phase results in drops that are more deformed than their Newtonian counterparts, but the effect of increase in elasticity does not always result in an increased deformation.

Simulations were performed for Ca = 0.1, c was varied between 0.01 and 1 and De was varied between 0.01 and 3. Deformation was analyzed as a function of De at constant c and vice versa to independently study the effect of each parameter on deformation of drop.

Effect of Polymer Concentration *c* and Deborah Number De

To understand the effect of De and *c* on the deformation of viscoelastic drops in Newtonian simple shear flows, the variation in the maximum values of trA was plotted as a function of *c* and De. From Figure 5.21, it can be seen that just as in the case of a Newtonian drop in viscoelastic shear flow, the trA increases with increase in De and decreases with increase in *c*.

However, their effect on the deformation of the drop is the opposite. While increasing *c* increases the deformation of a Newtonian drop in viscoelastic shear flow, it decreases the deformation of a viscoelastic drop. It can be noticed from Figure 5.22 that at higher value of *c* the drop deformation is smaller.

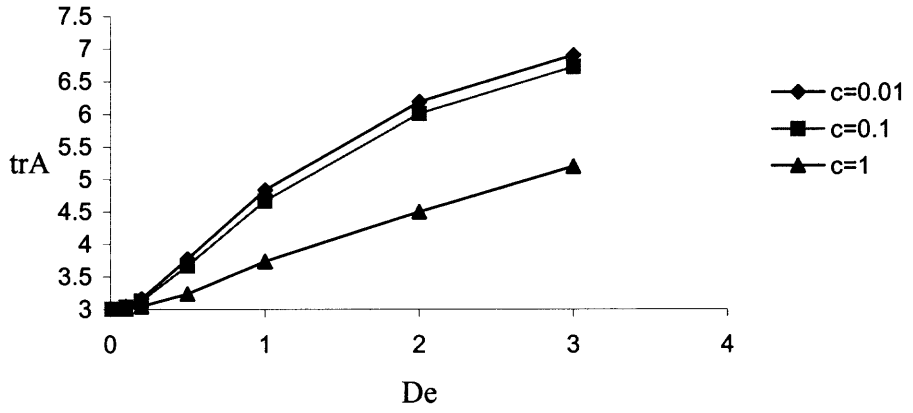

Figure 5.21 trA is plotted against De for c = 0.01, 0.1 and 1. Ca = 0.1, η_o = 10.25 Poise.

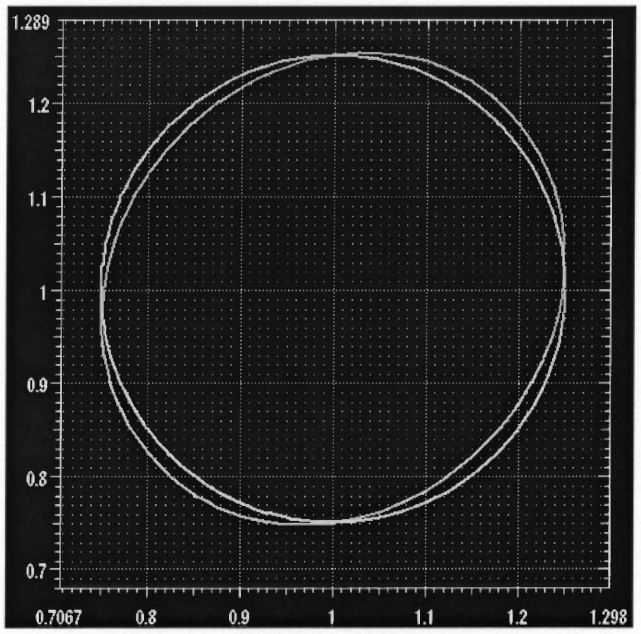

Figure 5.22 Steady state deformed drop shapes for c=0.01 and c=1. Ca = 0.1, η_o = 10.25 Poise and De = 0.01. The deformation parameter, $D_{c=1}$ = 0.07283, while $D_{c=0.01}$ = 0.09795.

To analyze the effect of De on the deformation of a viscoelastic drop in a Newtonian simple shear flow, numerical simulations were performed for De between 0.01 and De = 3. The value of Ca was held constant at Ca = 0.1. From Figure 5.21 it is known that for a constant value of Ca, the maximum value of tr**A** increases with increasing De. The extensional viscoelastic stresses pull the drop surface near the tip of the major axis inwards, and therefore the drop deformation decreases when De increases. This trend, however, reverses for the higher values of De for which the drop deformation increases with increasing De (See Figure 5.23). This behavior of viscoelastic liquids is not unexpected. For example, the drag coefficient for a cylinder placed in an Oldroyd-B fluid decreases with De for De < ~ O(1). But, for the higher values of De the drag coefficient increases with increasing De. This is a consequence of the memory, and

resulting nonlinearly, of the Oldroyd-B fluid. It has been suggested in [Bousfield et al. (1988)], that this reversal trend at higher De's is due to the modification of velocity field from that for a Newtonian liquid. Specifically, at higher De's the shear rate in the region where the polymer stretch is relatively large is smaller than that for a Newtonian fluid in the same flow geometry.

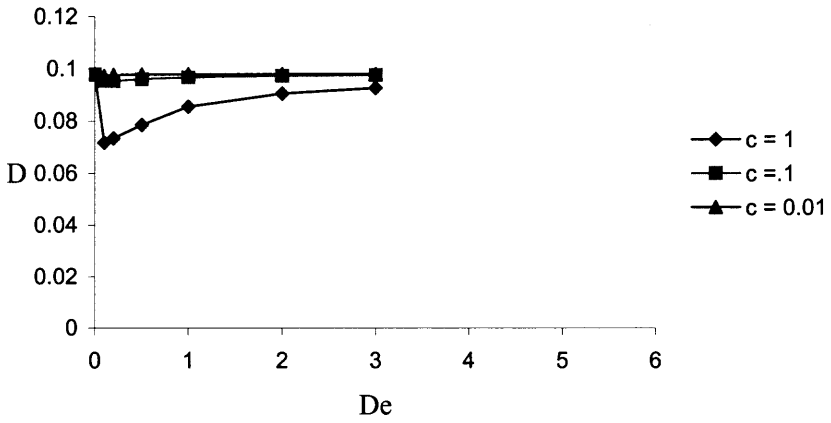

Figure 5.23 D is shown as a function of De for three different values of polymer concentration factor *c*. Ca = 0.1 and η_o = 10.25 Poise. The Newtonian deformation is a point of the y-axis corresponding to D_N = 0.0973

CHAPTER 6

RESULTS AND DISCUSSION – BUOYANCY DRIVEN BUBBLES

6.1 Introduction

The case of a Newtonian bubble rising in an Oldroyd-B fluid is studied in this chapter. The goal is to analyze the transient and the steady state velocity of the bubble and the effect of viscoelastic stresses on the shape of the bubble. Simulations were carried out for a range of bubble radii varying between 0.1 and 0.4 cm and relaxation times, between 0.1s and 0.2s sec. The interfacial tension was held constant at 10 dynes/cm and the zero-shear viscosity (η_o) was maintained at 10.25 Poise. Simulations were stopped when the bubble assumed a fixed shape and attained a constant rise velocity. Since the viscosity of the ambient fluid affects the rise velocity of the bubble, the zero-shear viscosity was maintained constant and only the relative magnitudes of viscous and elastic contribution to the zero-shear viscosity were varied. This was achieved by varying the polymer concentration factor c in the Oldroyd-B model, which controls the polymer contribution to zero-shear viscosity. By choosing this approach, it is easier to focus on the effect of the elastic and viscous components of the ambient viscoelastic fluid on the behavior of the rising bubble, without having to worry about additional complications introduced by the change in viscosity ratio.

The variation in rise velocity with bubble volume was investigated for different values of polymer concentration parameter c = 19.5, 12.667, 9.25, 5.8375 and 4.125. The relative magnitudes of polymer (η_p) and solvent (η_s) contributions to zero shear viscosity

(η_o) for different values of c are shown in Table 2. For the range of λ_r, a, and c considered, De varies between $0.5 \leq De \leq 40$, $Re \leq 0.1$, $Fr < 0.6$ and $We < 4.6$.

c	η_o (Poise)	η_s (Poise)	η_p (Poise)
19.5	10.25	0.5	9.75
12.667	10.25	0.75	9.5
9.25	10.25	1	9.25
5.8375	10.25	1.5	8.75
4.125	10.25	2	8.25

Table 6.1. The magnitudes of η_s and η_p for different values of c. Notice that $\eta_o = 10.25$ for all cases.

Simulations were started with a spherical bubble placed at a distance of 0.5 cm from the bottom of the computational domain. The velocity on the domain boundary is set to zero. The initial velocities of the bubble and the ambient fluid are assumed to be zero and the configuration tensor $\mathbf{A} = \mathbf{I}$, which is the relaxed state of the Oldroyd-B fluid. . The bubble velocity u(t) is defined to be the volume averaged velocity of the fluid inside. When the bubble reaches a steady state, u(t) is a constant, and the shape is fixed.

Two computational domains with dimensions 2x2x4 cm (Domain A) and 1.5x1.5x3 cm (Domain B), were used in our simulations. The reason for choosing domains with two different cross sections is that for small bubbles, radius ≤ 0.125 cm, higher spatial resolution is necessary to obtain convergent results. It is computationally expensive to have high resolution for a big domain and hence a smaller domain was used for bubbles with radius ≤ 0.125 cm.

In order to be able to use two different sized domains, it is necessary to show that the bubble velocity is not affected by the proximity of the bubble to the domain wall. In

Figure 6.1, the transient velocity of bubbles of radii 0.125 cm and 0.2 cm rising in the above mentioned domains are plotted. When the radius is 0.2 cm, we see that the bubble velocity, both transient as well as steady state, is consistently higher for the bubble rising in the bigger domain. Clearly, for the bubble of radius 0.2 cm, the wall effects are significant. But, when the bubble radius is 0.125 cm, the transient and the steady state velocities of the bubble in the two domain are approximately equal which justifies the use of smaller domain for bubbles whose radius is 0.125 cm or smaller.

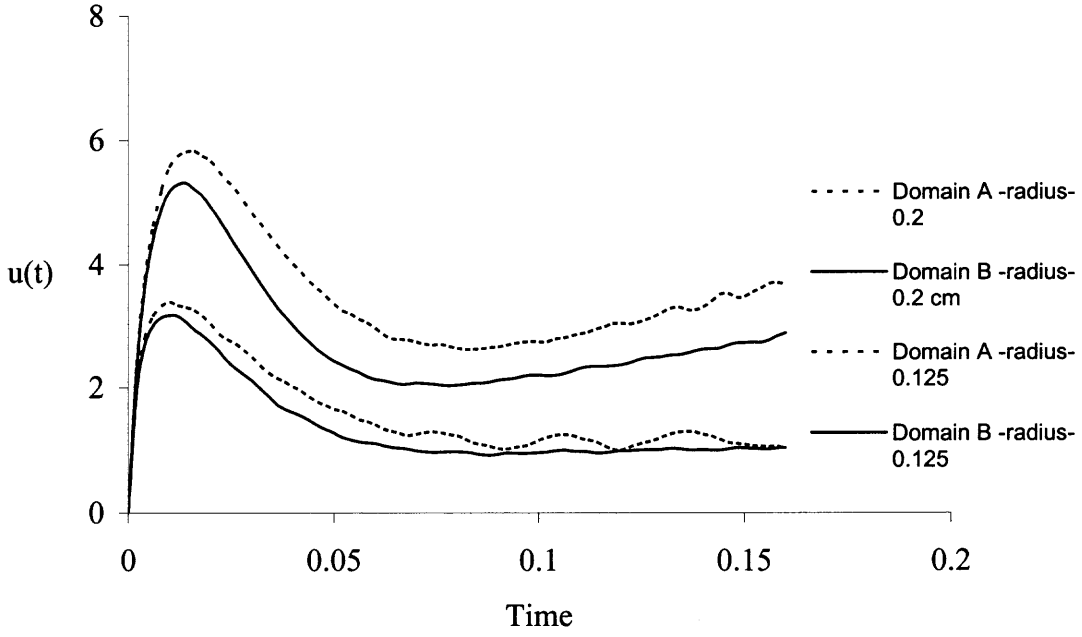

Figure 6.1 Transient velocity of bubbles of radii 0.125 cm and 0.2 cm rising in domains A and B. The parameters are $\eta_o = 10.25$ Poise, $c = 4.125$, $\lambda_r = 0.1$s, $\gamma = 10$ dynes/cm.

6.2 Oscillatory Transient Response

The transient behavior of buoyant bubbles accelerating from rest in a viscoelastic fluid depends on its volume, its initial shape, the magnitudes of the viscous and elastic stresses which depend on the fluid viscosity and the relaxation time. The bubble is driven by the force of buoyancy and the viscous and elastic forces resist its motion. The problem of a

rising bubbles differs from that of a falling sphere, since, in addition to these forces, the surface tension force acts on the bubble surface and the shape of the bubble does not stay spherical. If the deforming stresses at the interface are sufficiently smaller than the surface tension force, the bubble shape remains approximately spherical. But, when these deforming forces are significant the interface deforms and the bubble shape changes from spherical to either prolate or oblate shapes depending on the nature of the ambient fluid. Results of simulations indicate that a change in the bubble shape is accompanied by a change in the fluid velocity around the bubble which in turn affects the net drag force acting on the bubble. Given the transient interaction between the shape, velocity and drag, it is reasonable to expect that a rising bubble will experience a longer period of transience than a falling sphere for which the shape is fixed.

The transient velocity of a bubble of radius 0.25 cm rising in a viscoelastic fluid is shown in Figure. 6.2a:

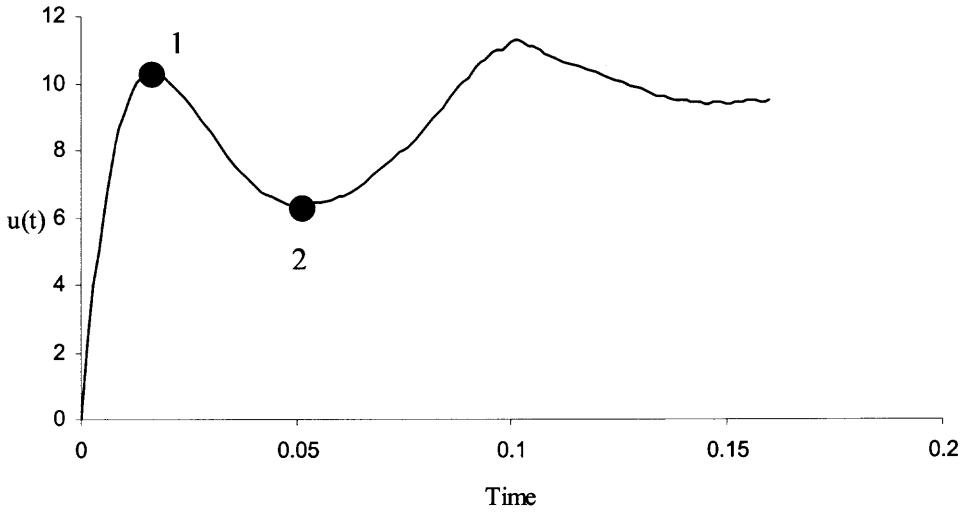

Figure 6.2a Rise velocity u(t) velocity of a bubble of radius = 0.25 cm rising in a viscoelastic fluid with $c = 12.667$, $\lambda_r = 0.1$s, $\gamma = 10$ dynes/cm.

Clearly, the initial motion of the bubble is dominated by the viscous effects, as the viscoelastic stresses take some time to build up. The velocity field and the tr**A** at the time marked 1 in Figure 6.2a are shown in 6.2b-c. After the viscoelastic stresses build up, the bubble velocity decreases and this causes the first overshoot in the velocity vs. time curve of Figure 6.2a.

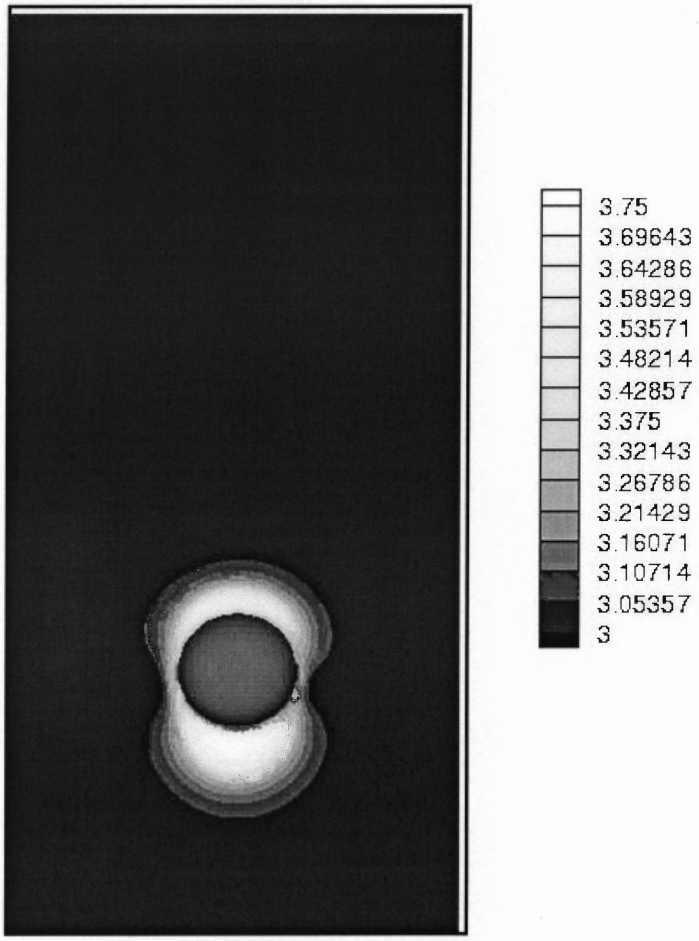

Figure 6.2b Isovalues of tr**A** at t ≈ 0.015s, corresponding to point 1 in Figure. 6.2a, the bubble radius = 0.25cm. The parameters are c = 12.667, λ_r = 0.1s, γ = 10 dynes/cm. At this time, the maximum value of tr**A** is 3.75, which occurs at the trailing end of the bubble. Since the maximum value is only slightly greater than 3.0, the viscoelastic stresses have are not important at this time.

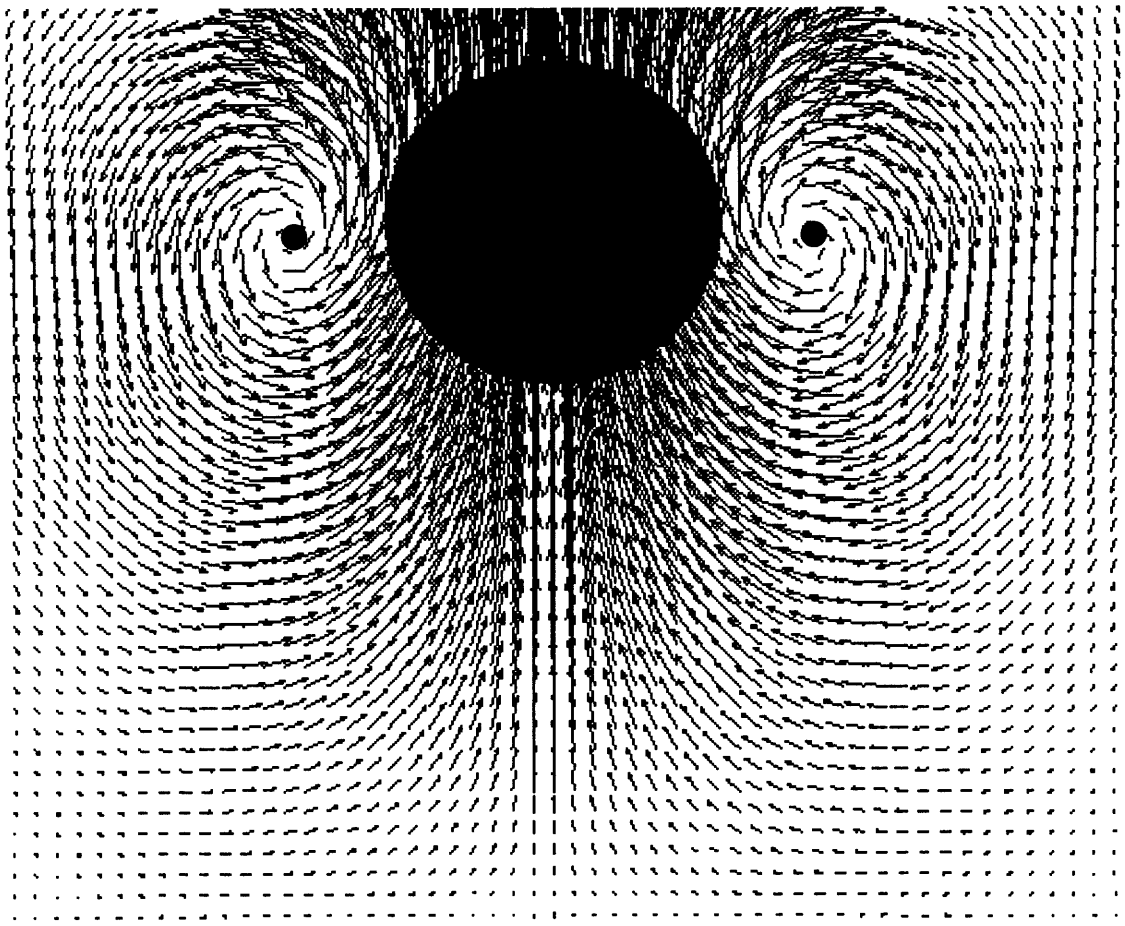

Figure 6.2c The velocity vectors around the bubble at t ≈ 0.015s. The bubble radius = 0.25cm. The parameters are c = 12.667, λ_r = 0.1s, γ = 10 dynes/cm. Note that at this stage, the velocity in the wake of the bubble is in the direction of motion of the bubble. The centers of the two recirculation zones are indicated by black dots.

Following this rapid initial acceleration, the viscoelastic effects start to become significant, and the bubble starts to decelerate. The distribution of tr**A** at stage 2 marked in Figure 6.2a is shown in Figure 6.2d. The maximum value of tr**A** has grown to 4.5. It is at this point in the rise of the bubble that the structure of the wake changes, i.e., the velocity vectors near the trailing end of the bubble now point in the direction opposite to the direction of motion of the bubble (see Figure 6.2e).

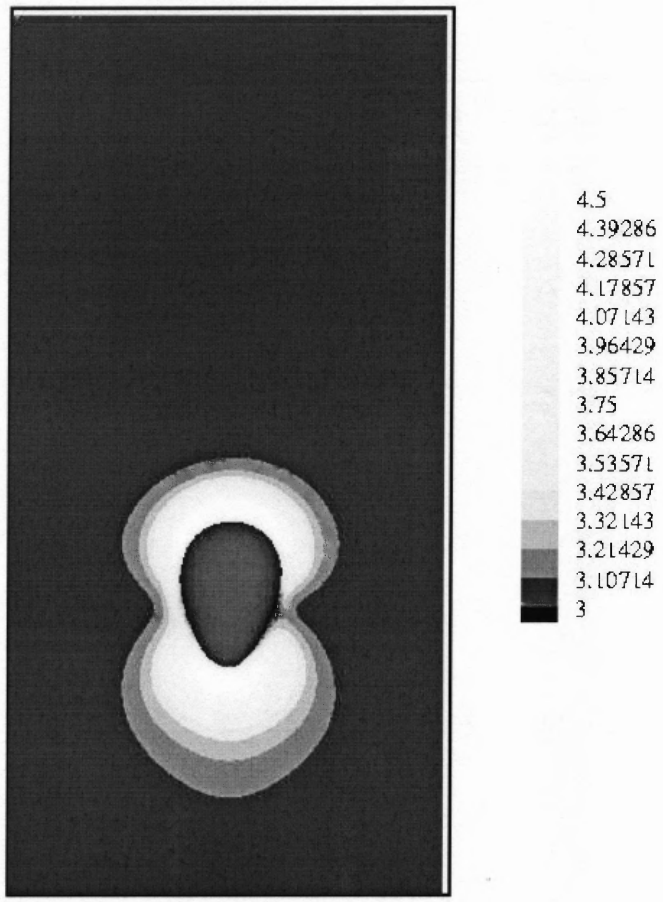

Figure 6.2d Isovalues of tr**A** at t ≈ 0.05s, corresponding to point 2 in Figure. 6.2a, the bubble radius = 0.25cm. The parameters are c = 12.667, λ_r = 0.1s, γ = 10 dynes/cm. At this time, the maximum value of tr**A** is 4.5, which occurs at the trailing end of the bubble.

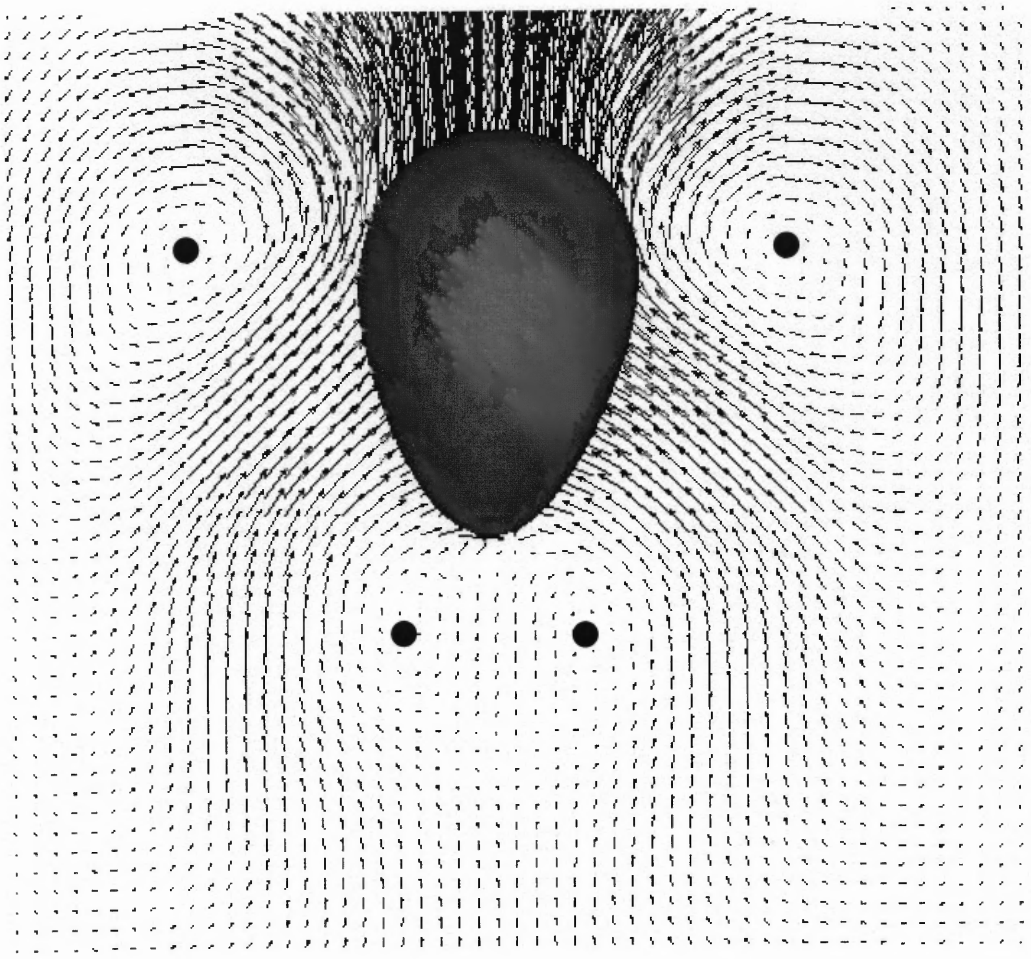

Figure 6.2e The velocity vector in the vicinity of a bubble with a = 0.25cm at t ≈ 0.05s, corresponding to point 2 in Figure 6.2a. The parameters are c = 12.667, λ_r = 0.1s, γ = 10 dynes/cm. Note that at this stage, the velocity in the wake of the bubble is in the direction opposite to the direction of motion of the bubble. The wake therefore is a negative wake. Note too that there are two additional recirculation zones in the wake which are indicated by black dots.

At the end of the deceleration phase, either of the two situations entail: the bubble attains terminal velocity and a steady state shape which is either prolate with a rounded trailing end (See bottom image in Figure 6.3, corresponding to a = 0.2 cm) or the bubble undergoes a shape change from prolate to one with a cusp like tail (top image in Figure 6.3 corresponding to a = 0.30 cm) and accelerates again to attain a higher terminal velocity. Thus, there appears to be a connection between the bubble shape and its rise

velocity, which will be discussed in detail while explaining the sharp increase in velocity-volume curve observed in a critical bubble volume range.

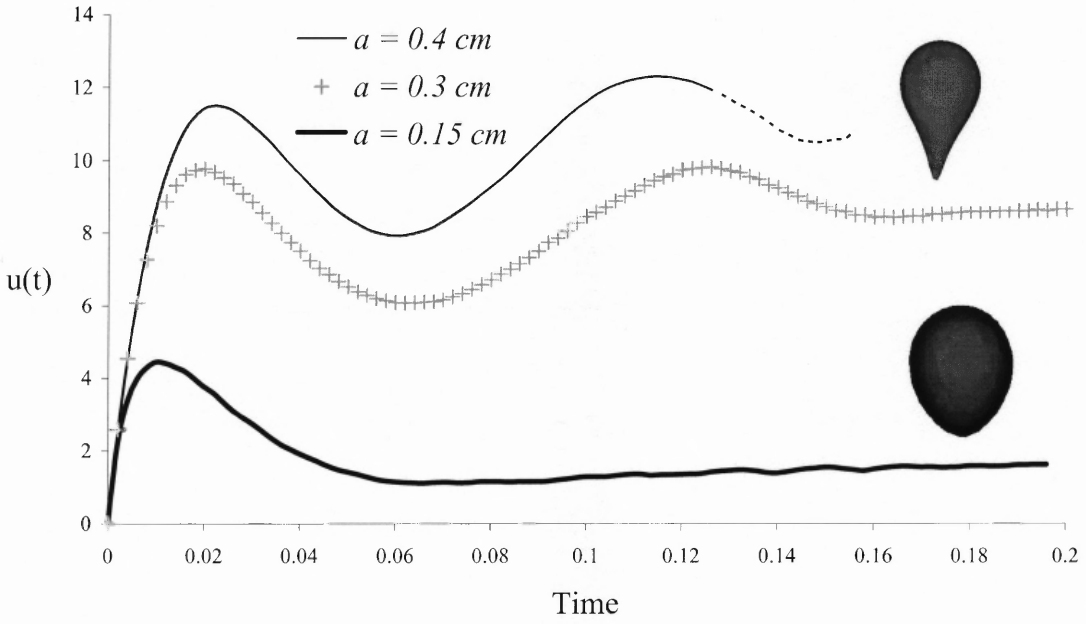

Figure 6.3 The transient velocity of bubbles of radii 0.15cm, 0.3cm and 0.4cm rising in a viscoelastic fluid with η_o = 10.25 Poise, c = 5.8375 and λ_r = 0.1s, γ = 10 dynes/cm. For a = 0.15cm, after the initial overshoot the bubble decelerates to a constant velocity and a steady shape that is either spherical or rounded prolate. For a = 0.30cm, the trailing end develops a cusp like trailing edge and velocity increases before reaching a higher terminal value. For a = 0.40cm, the bubble did not attain a steady shape or constant velocity within the length of the computational domain, but the oscillations appears to be decaying.

King and Walters [1972], in their analysis of unsteady motion of spheres in Elastico-viscous liquids noticed a similar behavior for falling spheres. They observed that the velocity overshoots the steady state velocity, and showed that the elastic contribution becomes significant, the sphere starts to decelerate.

The results of our simulation indicate a similar behavior up to the end of the deceleration stage. It is beyond this stage that the transient response of a bubble deviates from that of a sphere because the bubble starts to deform due to the extensional nature of

viscoelastic stresses near the trailing end of the bubble. When the interfacial forces dominate, the bubble attains a steady shape that is either spherical or prolate without a pronounced tail and the bubble attains a constant velocity. However, when the viscous and viscoelastic stresses at the interface overcome the interfacial tension, the bubble develops a cusp like trailing end and this change in the bubble shape is accompanied by an increase in the velocity as can be noticed from the upper two curves in Figure 6.3, corresponding to a = 0.3 cm and 0.4 cm.

6.2.1 Transient Response as a Function of *c*

In this section the transient response of a rising bubble is analyzed as a function of the c, and the other parameters are kept constant. Since η_o is kept constant, changing c merely changes η_p and η_s while keeping $\eta_p + \eta_s$ constant.

The transient response of a bubble with a = 0.35 cm rising in a viscoelastic fluid with ηo = 10.25 Poise, λ_r = 0.1s is shown in Figure 6.4 for three different values of c. We note from this figure that the magnitudes of velocity overshoot increase with increase in c and that the velocity is more oscillatory at higher values of c. From Figure 6.4 we also note that the amplitude of oscillations is higher when c is larger, as the viscoelastic stresses become stronger with increasing c. After the initial overshoot, the bubble starts to decelerate due to the build up of elastic stresses. After the deceleration phase, for c = 4.125, the bubble remains approximately spherical, and its rise velocity reaches a steady value without further oscillations. For c = 9.25, on the other hand, the shape of the bubble changes and the bubble velocity oscillates before reaching a steady value.

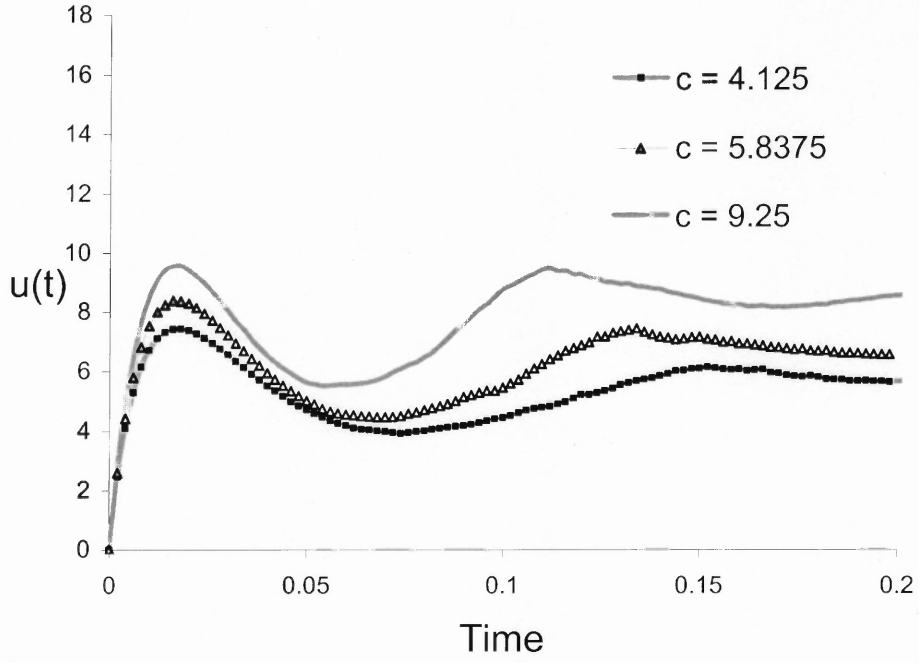

Figure 6.4 The bubble rise velocity is shown as a function of time for three different values of c; $a = 0.35$ cm, $\eta_o = 10.25$ Poise and $\lambda_r = 0.1$s.

6.2.2 Convergence of Transient Results at Large *c's*

In this section the numerical results obtained for relatively large values of c are shown to converge with increase in spatial resolution and decrease in time step. In Figure 6.5a–f, the rise velocity is plotted as a function of time for different resolutions and time steps. The results are identical for $t < 0.04$s, but deviate as t increases. The deviation at larger times is due to the fact that when the mesh is not sufficiently refined or when time step is not sufficiently small, the bubble volume decreases which in turn alters its rise velocity. However, we find that by increasing the resolution and reducing the time step, the

volume loss can be kept approximately constant. It is critical that the bubble volume does not change since it affects the buoyant lift, the drag, and thus also the rise velocity.

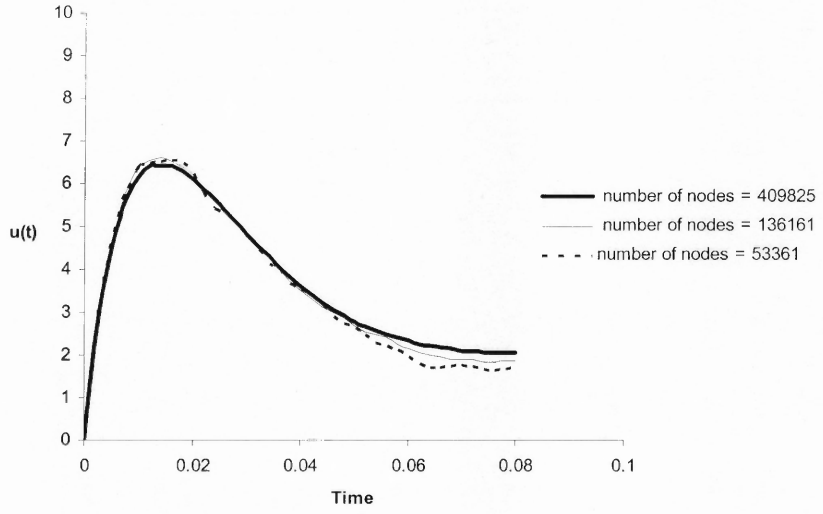

Figure 6.5a Convergence with resolution; η_o = 10.25 Poise, λ_r = 0.1s, c = 4.125 and a = 0.25cm.

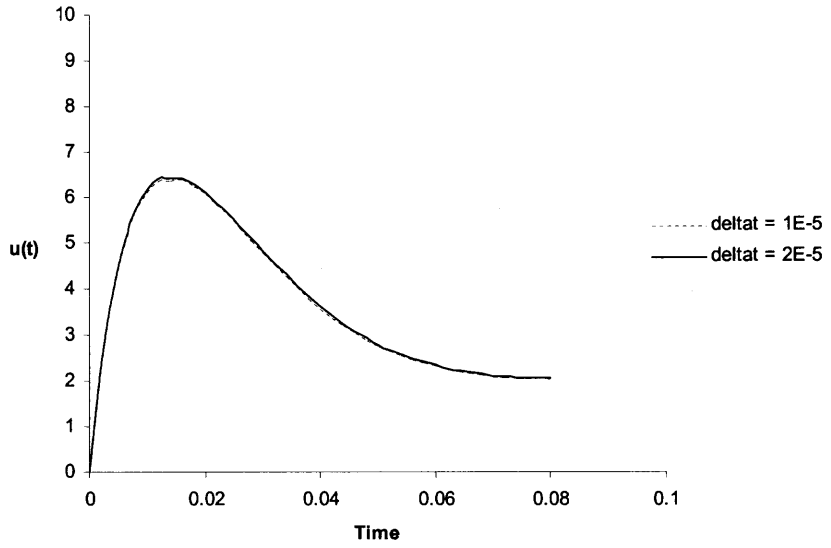

Figure 6.5b Convergence with time step; η_o = 10.25 Poise, λ_r = 0.1s, c = 4.125 and a = 0.25cm.

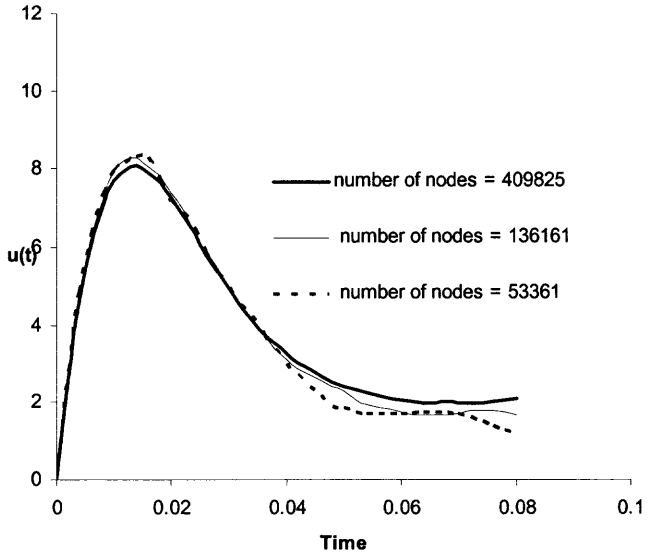

Figure 6.5c Convergence with resolution; η_o = 10.25 Poise, λ_r = 0.1s, c = 9.25 and a = 0.25cm.

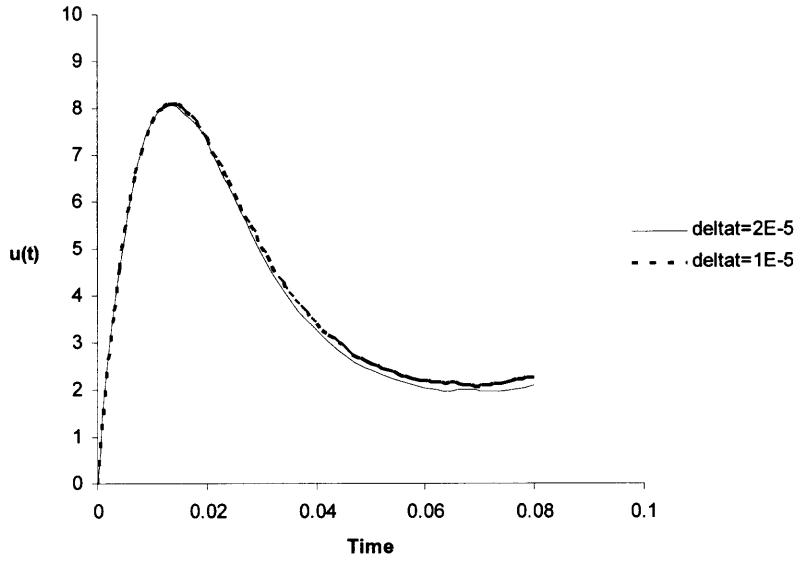

Figure 6.5d Convergence with time step; η_o = 10.25 Poise, λ_r = 0.1s, c = 9.25 and a = 0.25cm.

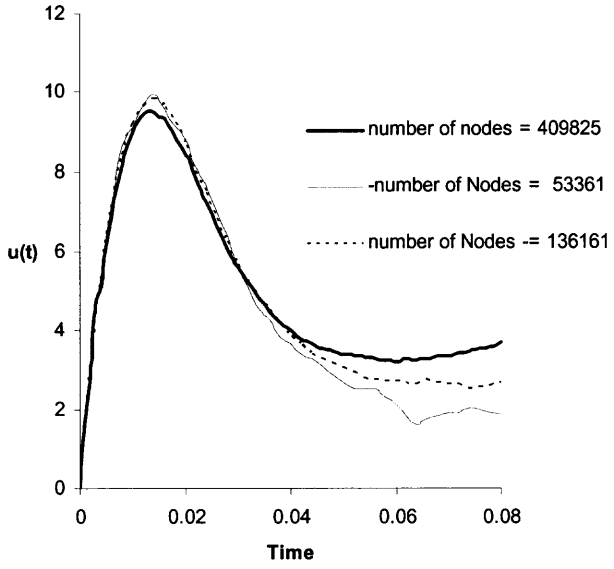

Figure 6.5e Convergence with resolution; η_o = 10.25 Poise, λ_r = 0.1s, c = 19.5 and a = 0.25cm. As c increases, the bubble with lower resolutions loose more volume than it would for a lower c

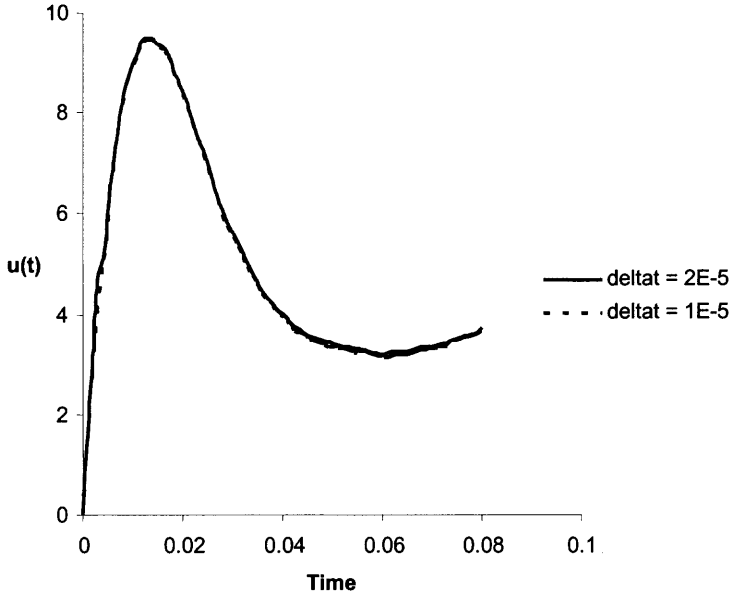

Figure 6.5f Convergence with time step refinement; η_o = 10.25 Poise, λ_r = 0.1s, c = 19.5 an$a$ = 0.25cm.

6.2.3 Transient Response as a Function of Relxation Time

The transient response of a rising bubble is analyzed as a function of λ_r. The values of c and a are held constant. The transient response of a bubble with a = 0.25 cm rising in a viscoelastic fluid with η_o = 10.25 and c = 19.5 for two values of λ_r are shown in Figure 6.6. The figure shows that both the overshoot in the bubble velocity and the steady state velocity are higher for the case with λ_r = 0.25s. Also notice that the peak value of overshoot occurs at a later time for λ_r = 0.25s.

As discussed in the previous sub-section, the overshoot occurs because the viscoelastic stresses take some time to build up and for the case with larger λ_r, the time required for build up is larger.

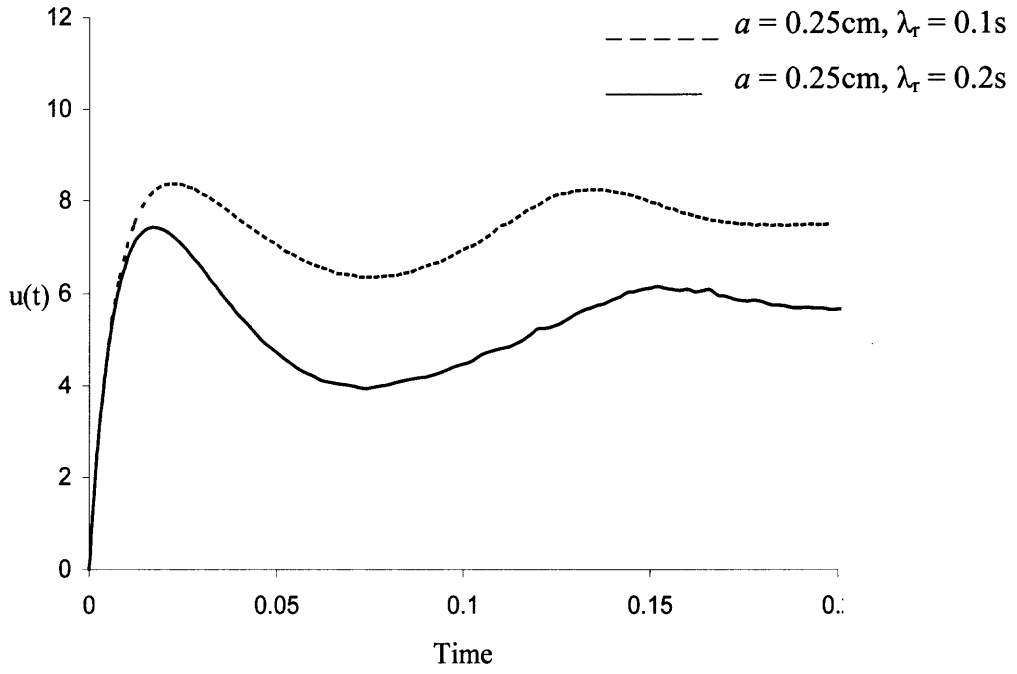

Figure 6.6 The rise velocity u(t) of a bubble a viscoelastic fluid with, $\eta_o = 10.25$ Poise, $c = 4.125$, $a = 0.25$cm for $\lambda_r = 0.1$s and 0.2s.

The above difference in the steady value of the bubble velocity is due to the viscoelastic stresses which are different for the two cases, and cause the shapes for the two cases to be different. As can be seen from Figure 6.7a and b, for $\lambda_r = 0.2$s, the trailing end of the bubble is pulled out further and the curvature of the bubble at the trailing end is reversed. As will be discussed later, the bubble shape is critical in determining its rise velocity.

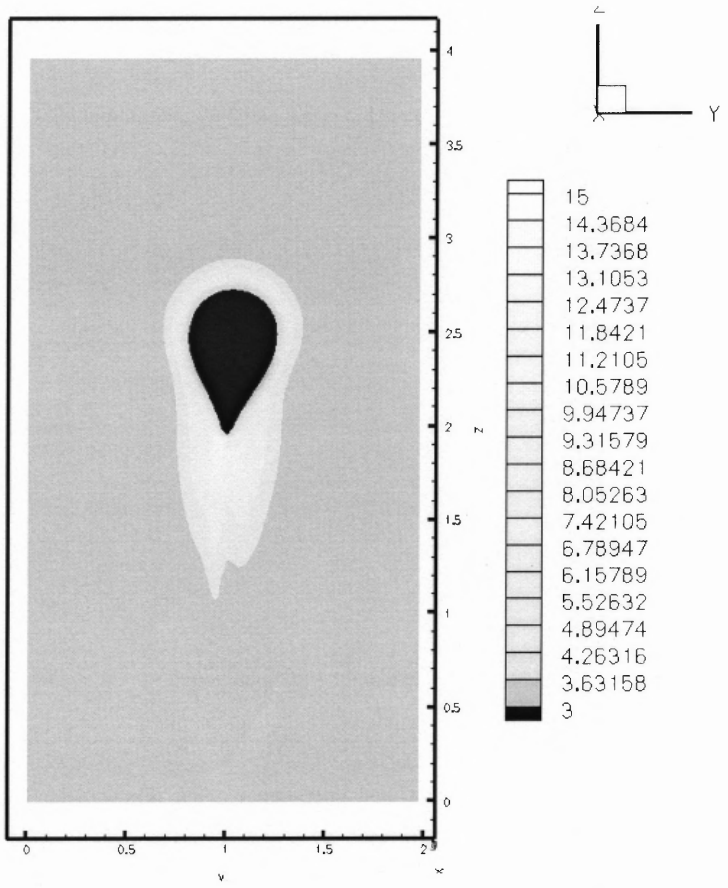

Figure 6.7a Isovalues of tr**A** at steady state for a bubble rising in a viscoelastic fluid with, η_o = 10.25 Poise, c = 4.125, a = 0.25cm and λ_r = 0.1s. Note that the maximum value of tr**A**, which occurs at the trailing end of the bubble, is ≈ 15.

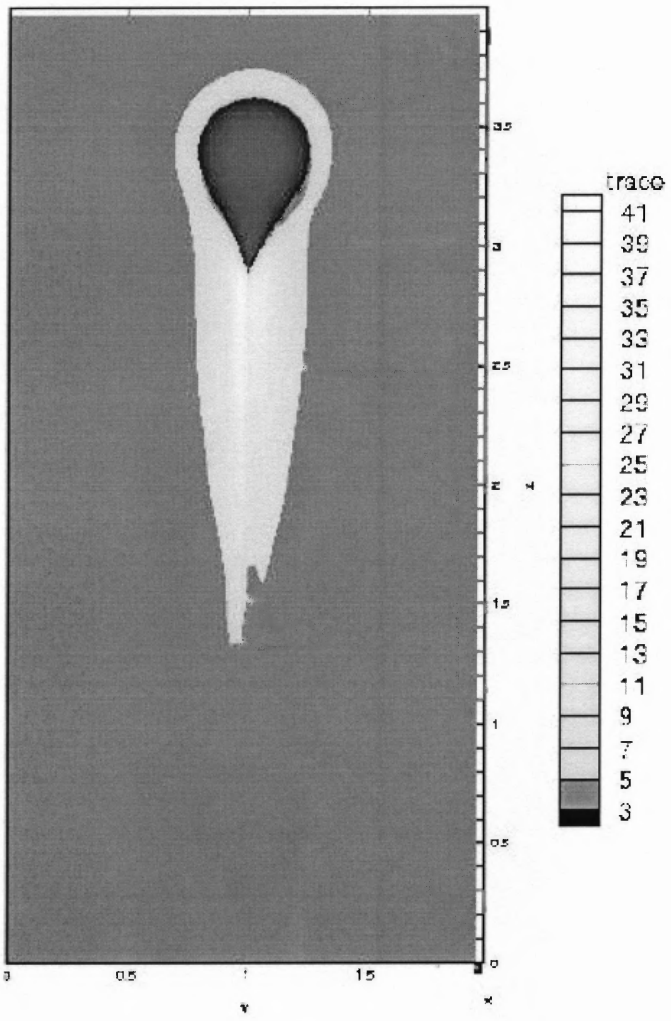

Figure 6.7b Isovalues of tr**A** at steady state for a bubble rising in a viscoelastic fluid with η_o = 10.25 Poise, c = 4.125, a = 0.25cm and λ_r = 0.2s. Note that the maximum value of tr**A**, which occurs at the trailing end of the bubble, is ≈ 40.

6.3 Sharp Change in Rise Velocity in the Velocity-Volume Plot

Another interesting aspect of the problem of a bubble rising in a viscoelastic fluid is the discontinuity or an abrupt change, in the terminal velocity of the bubble at a critical value of the bubble volume. It is worth noting that even for a bubble rising in a Newtonian fluid, the terminal velocity increases by a factor 1.5, which is the ratio of the drag

coefficients of a falling sphere and a rising bubble as discussed in Chapter 3. Many researchers have investigated the phenomenon of bubbles rising in viscoelastic liquids and observed that, as expected, the rise velocity of a bubble increases when its volume increases. In addition, it has been observed in experiments that in some viscoelastic liquids there is a critical bubble volume at which a tenfold increase in the rise velocity has been observed (Liu et al. [1995]).

The results of this simulation indicate that when the terminal velocity of rising bubbles is plotted against their volume, there is a small but finite volume range within which the terminal velocity increases very rapidly with increasing bubble volume. This steep increase has been analyzed below in terms of the transient behavior of bubbles, in and around this critical volume range.

Clearly, when the bubble volume is increased, the capillary number also increases, and thus larger bubbles are easier to deform. The viscoelastic stresses are also larger for larger sized bubbles as they have higher terminal velocities. Simulations show that the viscoelastic stresses are particularly large near the trailing ends of the bubbles and cause the bubbles trailing end to pull out. When the bubble volume is even larger, its trailing end assumes a two dimensional cusp-like shape.

In Figure 6.7 the transient velocities of the bubbles of three different radii rising in a viscoelastic fluid with c = 19.5 are shown. Notice that the overshoot is rather large for all three cases and that for a = 0.15 cm the bubble velocity, after the overshoot, undershoots and becomes negative. This phenomenon has been also observed for sphere falling in viscoelastic fluid (Zheng and Phan-Thien [1992]).

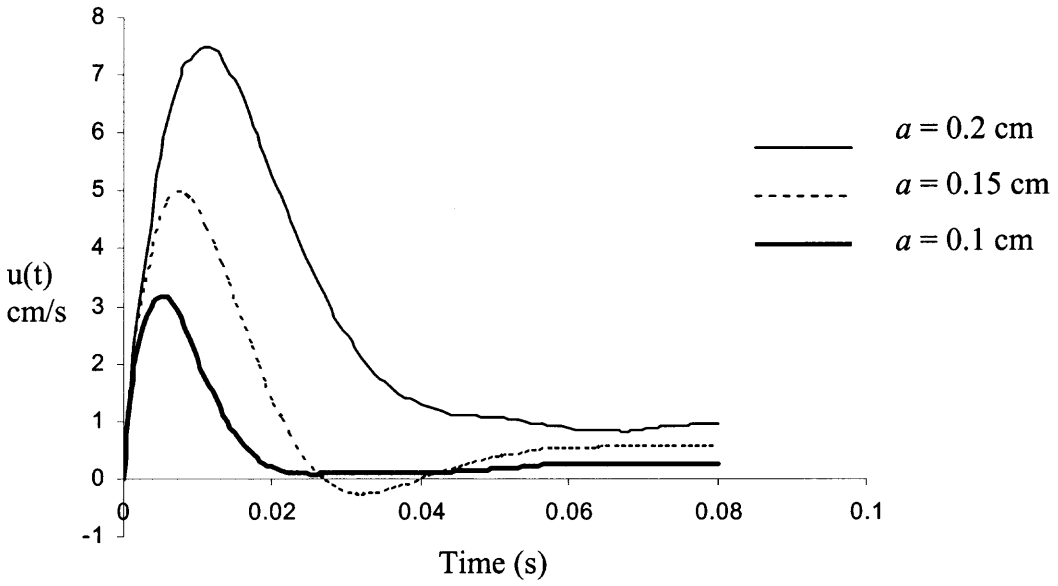

Figure 6.8 The rise velocity u(t) of a bubble rising in a viscoelastic fluid with, η_o = 10.25 Poise, λ_r = 0.1s, c = 19.5. For the case when a = 0.15cm the bubble reverses its direction and moves against the direction of buoyancy for a short time interval before the velocity becomes positive again.

The transient velocities of several bubbles with radius between 0.1 cm and 0.3 cm are shown in Figure 6.9. Note that the bottom three curves, which correspond to bubbles of radii 0.1 cm, 0.125 cm and 0.15 cm, respectively, attain steady state at the end of deceleration phase while the top three continue to accelerate. The velocities of the bubbles with $a \geq 0.2$ cm, continued to oscillate and did not reach steady state values before the bubbles reached the top of the domain. From Figure 6.10 in which the steady state velocity is plotted against the bubble volume on a log-log plot, one can notice that the terminal velocity of the bubble with a = 0.175 cm is 4.7 cm/s, which is approximately 6.5 times larger than the velocity of a bubble with a = 0.15 cm, which is 0.78 cm/s. Also notice that the velocities of bubbles with $a < 0.15$ cm, vary very little with change in radius. The six fold increase in terminal velocity occurs for a small change in volume when the bubble volume is approximately 0.015 cm^3.

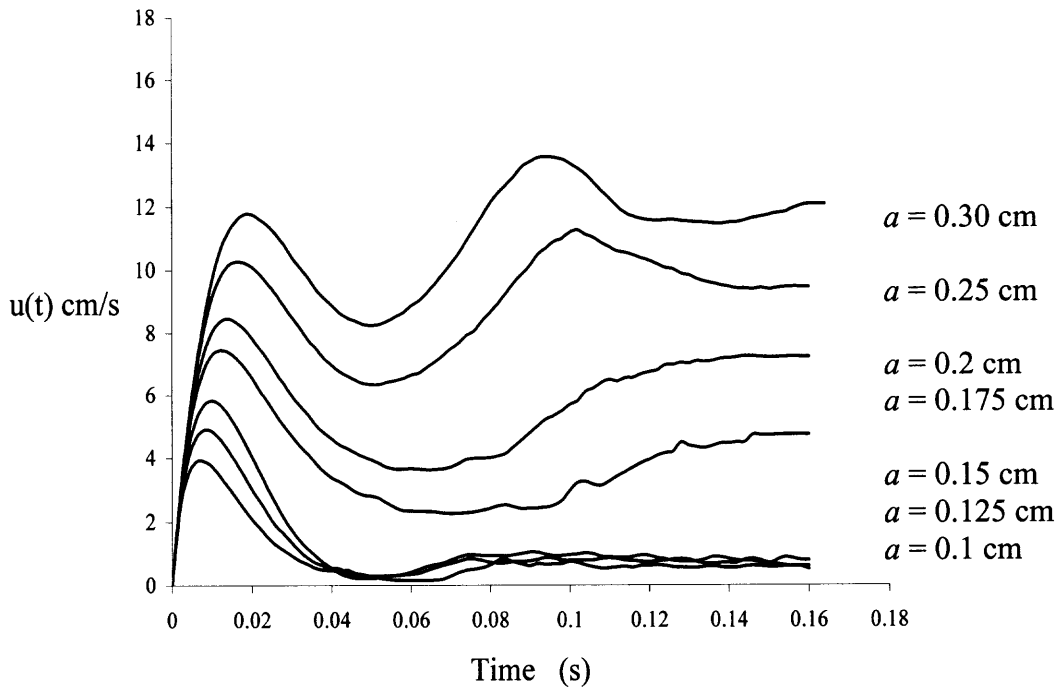

Figure 6.9 Transient velocity of bubbles, 0.1 cm $\leq$ radius $\leq$ 0.3 cm rising in a viscoelastic fluid; the zero-shear viscosity η_o = 10.25 Poise, c = 12.667, λ_r = 0.1s, γ = 10 dynes/cm.

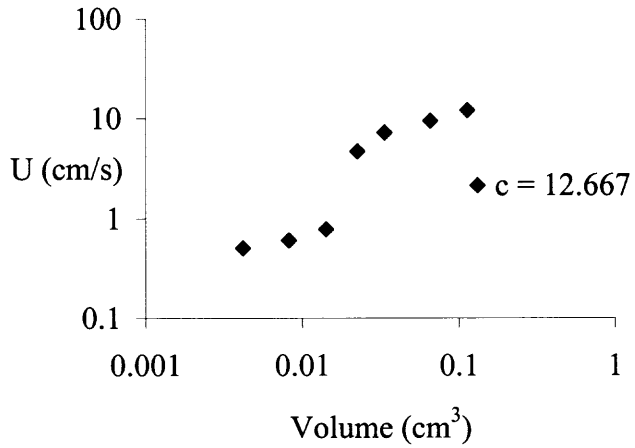

a (cm)	Volume (cm^3)	U (cm/s)
0.1	4.2E-03	0.51
0.125	8.2E-03	0.61
0.15	1.4E-02	0.78
0.175	2.2E-02	4.7
0.2	3.4E-02	7.22
0.25	6.5E-02	9.46
0.3	1.1E-01	12.07

Figure 6.10 Terminal velocity vs. volume on a log-log plot; 0.1cm< a < 0.35cm, η_o = 10.25 Poise, λ_r = 0.1s, c = 12.667 and γ = 10 dynes/cm. The terminal velocities of the bubble on either side of the sharp increase in the velocity-volume log-log plot are 0.78 cm/s and 4.7 cm/s. The terminal velocity increases by a factor of $\approx$ 6.5 when the bubble volume is increased by 1.5 times.

The simulation results indicate that bubbles for which the velocity oscillates after initial overshoot, the bubble shape changes from spherical to prolate with an extended or cusp like trailing end and for these bubbles the terminal velocity is relatively larger. This leads us to believe that the change in the bubble shape and rise velocity of the bubble are coupled. This in our opinion is the reason for the apparent sharp change in velocity at critical volume, i.e., bubbles with volumes on either side of the critical volume have markedly different transient behavior and a sizable difference in terminal velocities, as is evident from comparing the shapes of the bubble on either side of the sharp change in velocity-volume log-log plot (See Figure 6.3). We may therefore conclude that bubble shape plays a critical role in determining both the transient and terminal velocity of bubbles rising in viscoelastic fluids.

In analyzing the change in the transient behavior of a rising bubble as a function of c, it is readily apparent that terminal velocities are higher for larger c values. This corresponds to a steeper change in velocity at the critical volume at which the sharp change in the rise velocity occurs. From Figure 6.10 and Figure 6.11a-c, we note that the magnitude of velocity changes across either side of the critical range of volume at which the sharp increase in volume occurs increases with increase in c. As $c \rightarrow 0$, we expect that that the velocity-volume log-log plot will not have any apparent jump but instead have a 1.5 times increase in velocity as is observed for the Newtonian case.

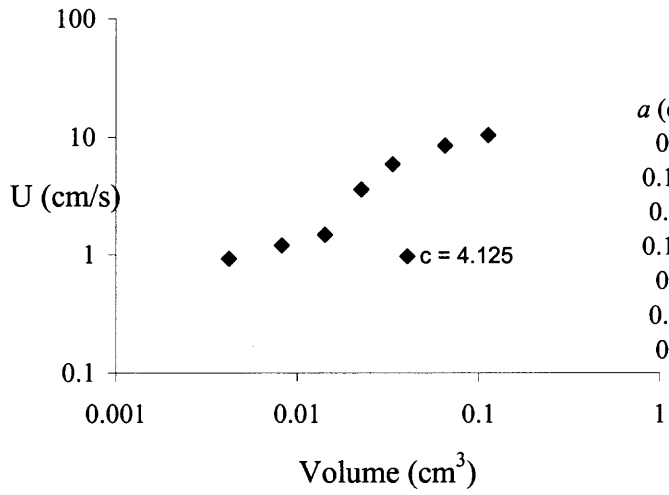

a (cm)	Volume (cm^3)	U (cm/s)
0.1	4.2E-03	0.61
0.125	8.2E-03	1.03
0.15	1.4E-02	1.45
0.175	2.2E-02	2.4
0.2	3.4E-02	3.99
0.25	6.5E-02	5.69
0.3	1.1E-01	7.44

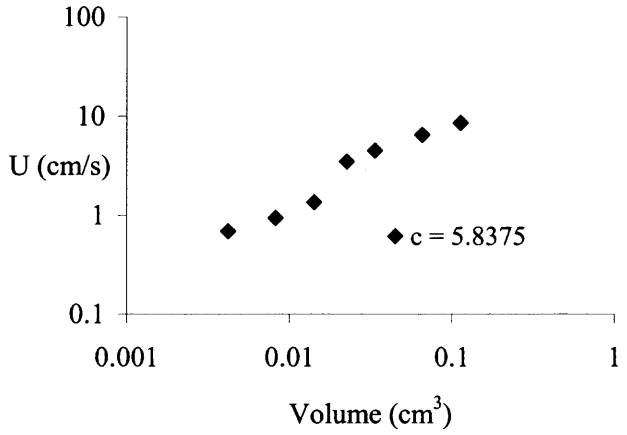

a (cm)	Volume (cm^3)	U (cm/s)
0.1	4.2E-03	0.69
0.125	8.2E-03	0.94
0.15	1.4E-02	1.35
0.175	2.2E-02	3.5
0.2	3.4E-02	4.5
0.25	6.5E-02	6.5
0.3	1.1E-01	8.6

Figure 6.11a-b Terminal velocity vs. volume on log-log plot; η_o = 10.25 Poise, λ_r = 0.1 s, 0.1cm < *a* < 0.35cm, *c* = 4.125, 5.8375. The magnitude of velocity changes across either side of the critical range of volume at which the sharp increase in volume occurs is much smaller for the above two cases than that for the case when *c* = 12.667 (See Figure 6.10).

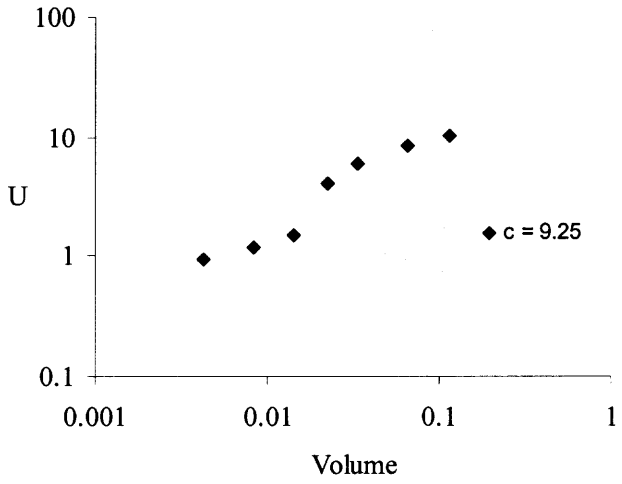

a (cm)	Volume (cm^3)	U (cm/s)
0.1	4.2E-03	0.92
0.125	8.2E-03	1.2
0.15	1.4E-02	1.51
0.175	2.2E-02	4.09
0.2	3.4E-02	5.92
0.25	6.5E-02	8.5
0.3	1.1E-01	10.4

Figure 6.11c Terminal velocity vs. volume log-log plot; η_o = 10.25 Poise, λ_r = 0.1s, 0.1cm < a < 0.35cm, c = 9.25.

6.4 Negative Wake and Recirculation Zones

The fluid velocity in the wake of a bubble rising in a viscoelastic fluid, very close to the trailing end, is in the direction of motion of the bubble. But, at a small distance from the trailing end, the velocity direction reverses (See Figure 6.14). For a bubble rising in a Newtonian liquid, the fluid velocity near the bubble is in the same direction as the motion of the bubble (See Figure 6.13).

The presence of a negative wake can also be seen more clearly in Figure 6.12 where the velocity vectors at a horizontal plane at a distance of 0.3 cm below the trailing end of the bubble are shown. Arrows indicate all vectors pointing out of the plane and dots indicate velocity vectors pointing into the plain. The vectors point downward in a circular region right below the trailing edge of the bubble and in the surrounding annular

region they point upward. Since the velocity vectors below the trailing end of the bubble point downward, the wake is considered to be negative.

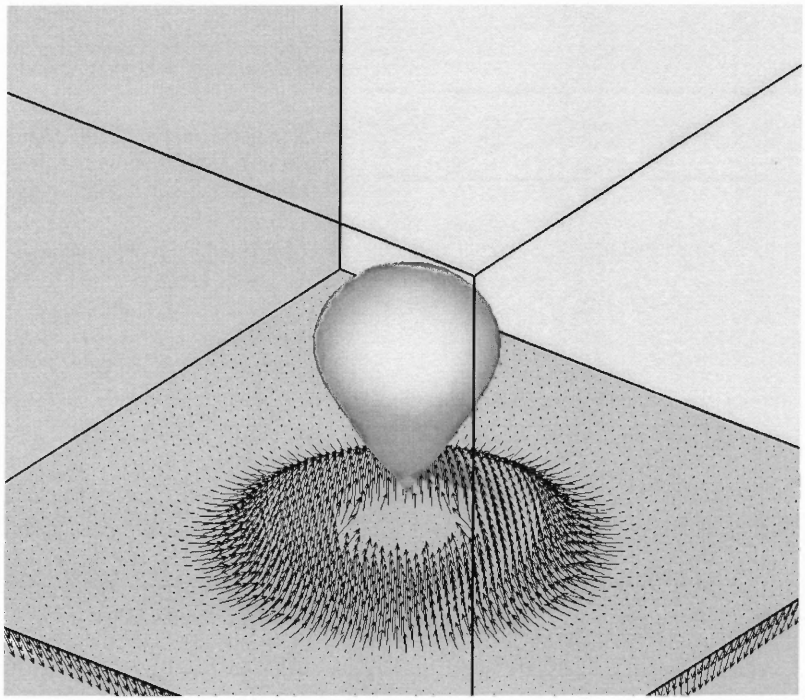

Figure 6.12 The velocity vectors on a plane at a distance of 0.3 cm from the trailing end of the bubble rising in a viscoelastic fluid; The parameters are η_o = 10.25 Poise, λ_r = 0.1s, a = 0.35cm and c = 19.5. In the circular region with dots, directly below the trailing end of the bubble, the velocity vectors point downwards, indicating that the fluid is moving away from the bubble. The wake is therefore negative.

Additionally, we also observe that apart from to the two recirculation zones at the equator of the bubble, which are also present for bubbles rising in Newtonian fluids (see Figure 6.13), there are two additional recirculation zones in the wake of a bubble (See Figure 6.14).

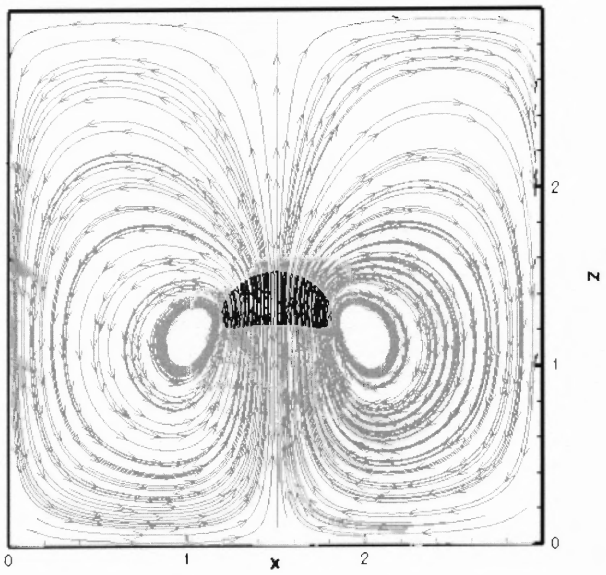

Figure 6.13 Stream traces on the domain mid-plane for a bubble rising in a Newtonian fluid with viscosity $\eta = 10.25$ Poise and $a = 0.3$cm. Notice that the velocity in the wake is in the upward direction, the direction of motion of the bubble.

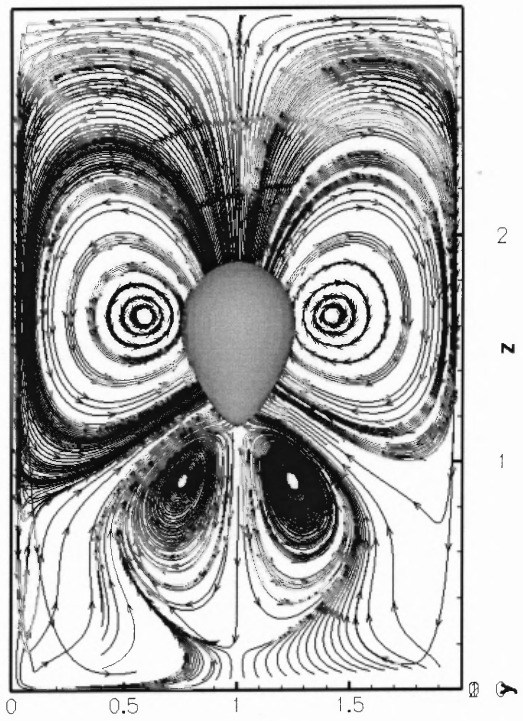

Figure 6.14 Stream traces on the domain mid-plane for a bubble rising in a viscoelastic fluid; $a = 0.35$, $c = 19.5$, $\eta o = 10.25$ Poise and $\lambda_r = 0.1$s. Notice that in addition to the two recirculation zones at the equator, there are two additional recirculation zones in the wake of the bubble.

It is quite interesting to see how the positions of the recirculation zones and the point of inflection, i.e., the point in the wake of the bubble where the velocity reverses direction, change as the c and λ_r are varied. The velocity vectors on a plane at the mid-section of the domain, with the recirculation zones indicated by black dots, are shown in Figure 6.15. Notice that as λ_r increases, the recirculation zone near the equator move away from the axis of the bubble, while the recirculation zones in the wake move closer to the axis of the bubble and the trailing edge (See Figure 6.15). On the other hand, when c increases, the recirculation zones in the wake move upward, closer to the trailing end, but do not move significantly in the horizontal direction (See Figure 6.16a-b), but the point of inflection (indicated by circle) moves upwards when c increases.

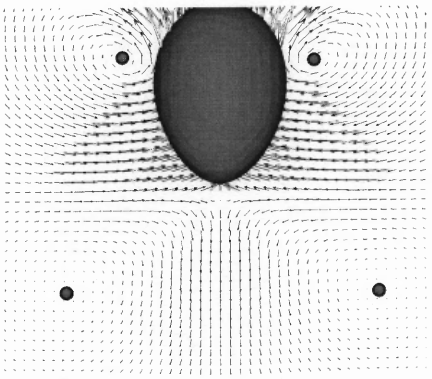

$\lambda_r = 0.1s$

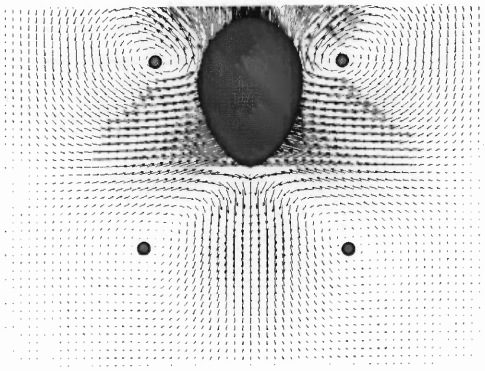

$\lambda_r = 0.125s$

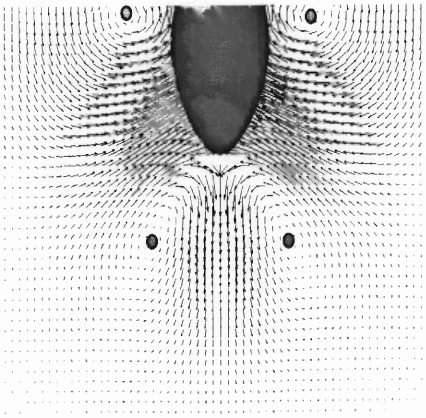

$\lambda_r = 0.15s$

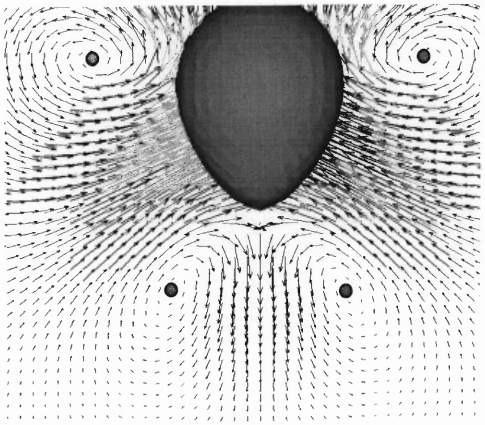

$\lambda_r = 0.175s$

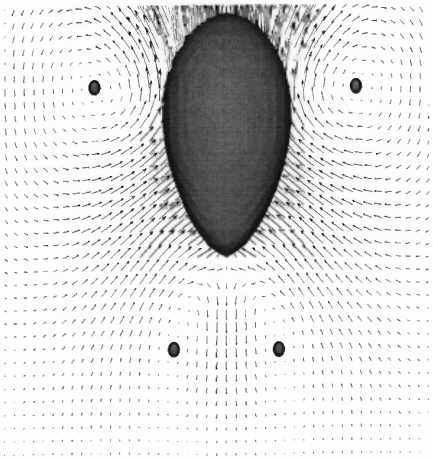

$\lambda_r = 0.2s$

Figure 6.15 The positions of the four recirculation zones for $0.1s < \lambda_r < 0.2s$, $c = 9.25$, $\eta_o = 10.25$ Poise and $a = 0.25cm$. Note that when λ_r is increased, the recirculation zones indicated by large black dots at the equator move away from the axis of the bubble, while the ones in the wake move closer to the vertical axis and to the trailing end of the rising bubble.

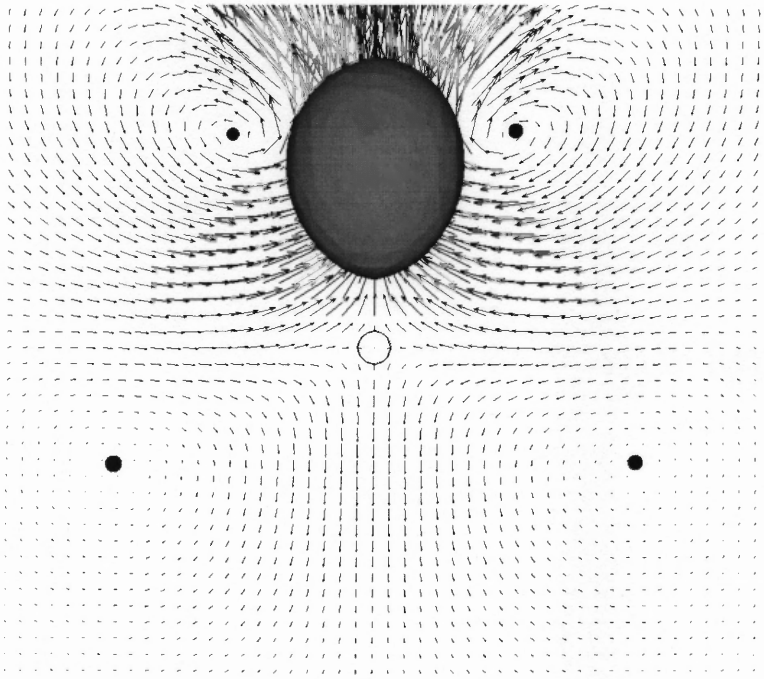

Figure 6.16a For $\lambda_r = 0.1$s, $c = 4.125$, $\eta_o = 10.25$ Poise and $a = 0.2$cm, the positions of the four recirculation zones are indicated by large black dots and the point of inflection in the wake of the bubble is indicated by a circle. The point of inflection is at a distance approximately equal to the radius of the undeformed bubble from the trailing end of the bubble.

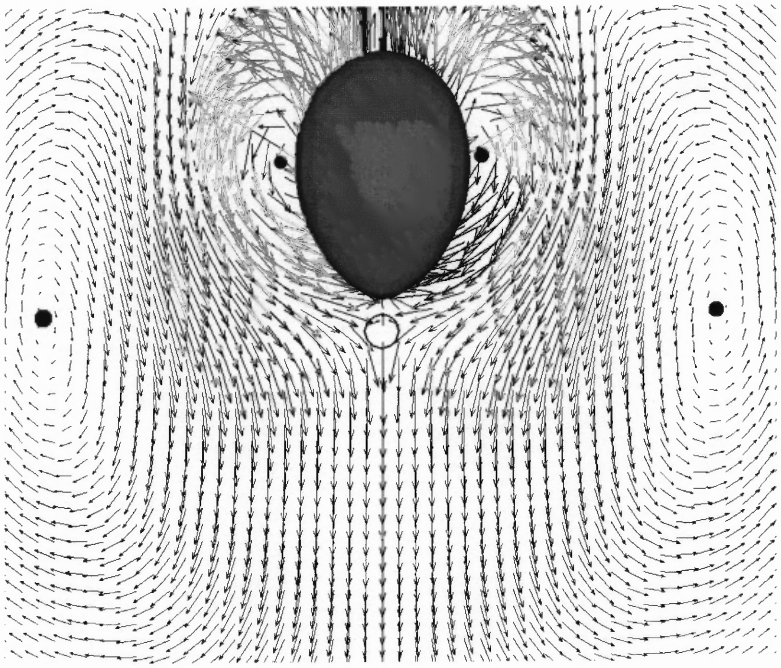

Figure 6.16b For λ_r = 0.2s, c = 4.125, η_o = 10.25 Poise and a = 0.2cm, notice in comparison with fig. 19a that the recirculation zones in the wake of the bubble are now approximately in line with the trailing end of the bubble while the recirculation zones at the equator have moved significantly closer to the bubble. Notice too that the position of the point of inflection is now much closer to the trailing end of the bubble.

From Figure 6.17, it can be noticed that the magnitude of maximum negative velocity in the wake of the bubble increases as the relaxation time of the ambient fluid is increased.

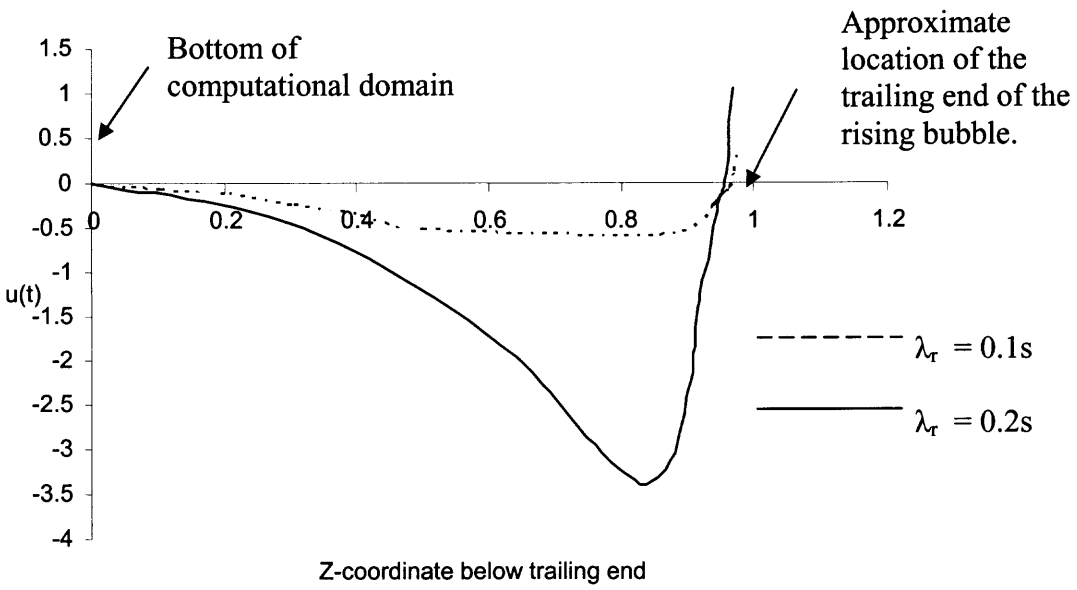

Figure 6.17 The velocity in the wake of a bubble, a = 0.25cm, rising in a viscoelastic fluids with η_o = 10.25 Poise, c = 9.25 and different values of relaxation time λ_r = 0.1s and λ_r = 0.2s.

It is worth noting that the result of numerical simulation indicates that negative wake was observed even for cases when the bubble reaches steady state shapes which were almost spherical, i.e. for volumes less than volume at which there is a steep rise in terminal velocity of the bubble. This result differs from those published by Hererra-Velarge et al. [2003] who observed a negative wake only when the bubble volume is greater than the critical volume at which a sharp change in velocity occurred. This apparent discrepancy is due to the fact that they investigated a different range of parameter space.

6.5 Two-Dimensional Cusp

Liu et al [1995] experimentally studied the rise of air bubbles in viscoelastic liquids inside channels with rectangular cross sections and found that the bubbles develop two-dimensional cusps with pointed trailing ends in one view and broad ends in an orthogonal view. Interestingly, in the narrow window the bubble appears to have a broad end, and in the broad window the bubble has a pointed end.

Unlike in the experiments conducted by Liu et al [1995] in which the shape of the trailing edge was different in the above two orthogonal views, we observed that due the square cross-section of our domain the bubble has a broad trailing edge in both orthogonal views (See Figure 6.18a-b). However, when viewed along the diagonal, the bubble had a pointed trailing end (See Figure 6.19).

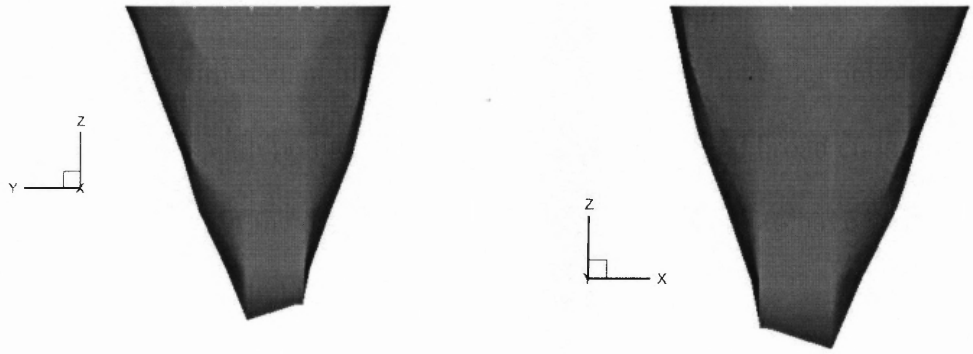

Figure 6.18 Magnified view of the trailing end of a bubble; a) Broad trailing end in the y-z plane and b) x-z plane for a bubble rising in a viscoelastic fluid in a domain with square cross section. The parameters are η_o = 10.25 Poise, c = 5.8375, a = 0.3, λ_r = 0.1s and γ = 10 dynes/cm.

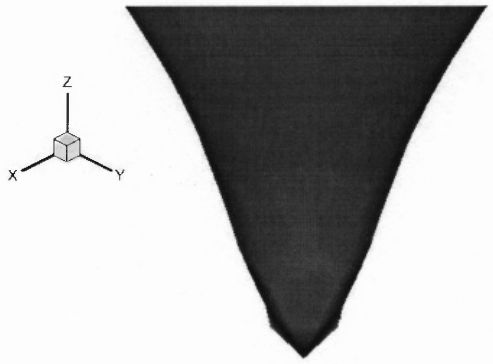

Figure 6.19 Pointed cusp-like trailing edge is seen when viewed along the cross-sectional diagonal of the computational domain, for the same parameters as above.

6.6 Analysis of Surface Tension Forces on Bubbles With Singular Surfaces

Let B be a bubble with a smooth (= C^2) closed surface S. The net surface force on the bubble assuming a constant surface tension coefficient γ is given as

$$\overline{\mathbf{F}} = \int_S 2\,H\,\gamma\,\hat{\mathbf{n}}\,dA \tag{6.1}$$

where, H is the mean curvature of S and $\hat{n}$ is the unit outer normal on S. It is known (see Blackmore and Ting [1985] and references therein) that $\overline{\mathbf{F}} = 0$. We shall show that for certain types of singularities in the surface at the trailing edge of the bubble, $\overline{\mathbf{F}}$ is no longer zero and there is a net upward force that accelerates the bubble. The smooth and the singular versions are illustrated below (See Figure 6.20a-b).

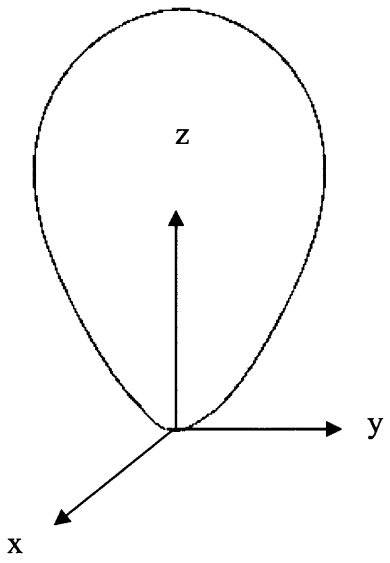

Figure 6.20a Smooth Bubble

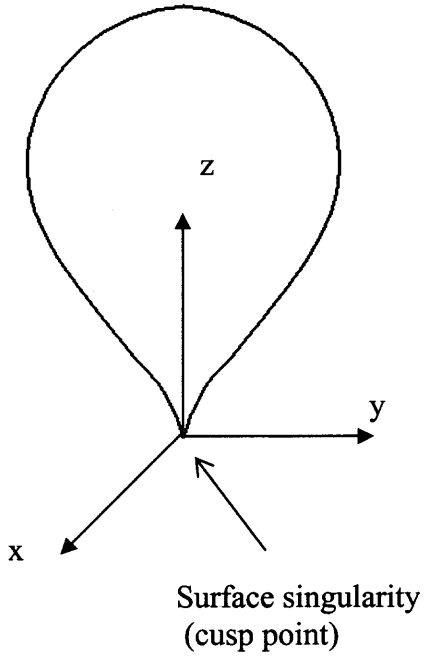

Figure 6.20b Singular bubble

6.6.1 Surface Forces

The most direct way of seeing that $\overline{\mathbf{F}} = 0$ when S is C^2 is to observe that the right hand side of Equation 6.1 can be written as the surface integral of a vector-valued two-form

$$2\gamma \int_S H\,\hat{\mathbf{n}}\,dA = 2\gamma \int_S \overline{\boldsymbol{\omega}} \tag{6.2}$$

where,

$$\overline{\boldsymbol{\omega}} = \omega_1\,\hat{\mathbf{i}} + \omega_2\,\hat{\mathbf{j}} + \omega_3\,\hat{\mathbf{k}} = H\,\hat{\mathbf{n}}\,dA, \tag{6.3}$$

and verify that the two-form $\overline{\boldsymbol{\omega}}$ is exact, namely, there exists a vector-valued one-form

$$\overline{\boldsymbol{\eta}} = \eta_1\,\hat{\mathbf{i}} + \eta_2\,\hat{\mathbf{j}} + \eta_3\,\hat{\mathbf{k}} \tag{6.4}$$

on S such that

$$d\bar{\eta} = d\eta_1 \hat{i} + d\eta_2 \hat{j} + d\eta_3 \hat{k} = \bar{\omega}. \tag{6.5}$$

Then a simple application of Stokes' theorem yields the derived result (Blackmore and Ting [1985])

$$\bar{F} = 2\gamma \int_S \bar{\omega} = 2\gamma \int_{\partial S} \bar{\eta} = 2\gamma \int_{\phi} \bar{\eta} = 0 \tag{6.6}$$

Blackmore and Ting [1] proved that the vector-valued one-form $\bar{\eta}$ is given as

$$\bar{\eta} = -\hat{n} \times d\bar{x} = \left(\langle \hat{n}, \hat{k} \rangle dy - \langle \hat{n}, \hat{j} \rangle dz\right)\hat{i} + \left(\langle \hat{n}, \hat{i} \rangle dz - \langle \hat{n}, \hat{k} \rangle dx\right)\hat{j} + \left(\langle \hat{n}, \hat{j} \rangle dx - \langle \hat{n}, \hat{i} \rangle dy\right)\hat{k} \tag{6.7}$$

where, $\bar{x} = (x,y,z) = x\hat{i} + y\hat{j} + z\hat{k}$, $\times$ denotes the usual vector cross-product in R^3, and $\langle \bullet, \bullet \rangle$ is the standard inner (dot) product of the vectors.

It is natural to ask if Equation 6.3 is still valid if the smoothness assumption on the surface S if the bubble is weakened. In particular, what happens if S has an isolated cusp or cone like pointing singularity or a line segment singularity? We shall show that Equation 6.3 holds for surfaces with isolated cusp-like or cone like singularities, but an additional nonzero upward force due to surface tension occurs for a trailing-edge singularity comprised of a line segment.

6.6.2 Cusp and Cone Point Singularities

Here we consider singularities at the trailing-edge of the bubble that can be modeled locally in the form (for $z \geq 0$) in a neighborhood of the region (trailing-point) in R^3:

$$z = \alpha r^q = \alpha (x^2 + y^2)^{q/2} \quad (\alpha > 0, \text{ q is a positive rational, } 0 < q \leq 1) \tag{6.8}$$

as illustrated in Figure 6.21a-b.

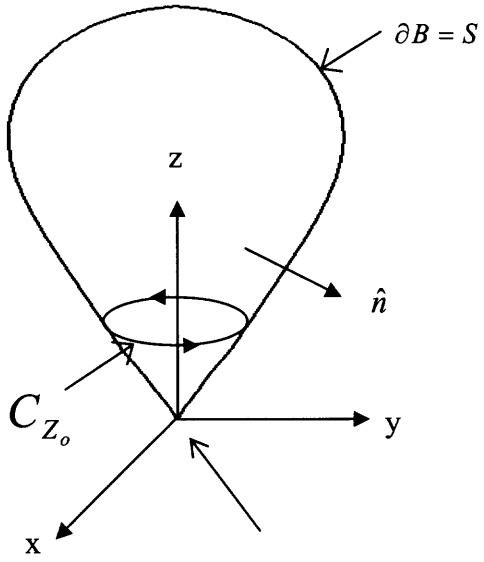

Isolated singular point

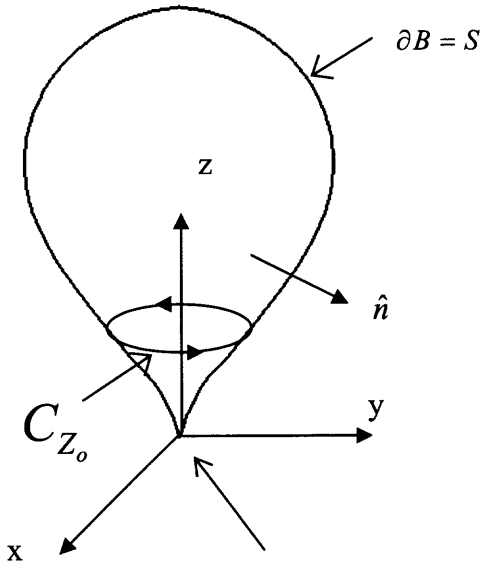

Isolated singular point

Figure 6.21a Cone point at origin (q = 1)

Figure 6.21b Cusp point at origin ($0 < q \leq 1$)

In the case under consideration the bubble surface is smooth except at the origin, so we can apply Stokes' theorem to the portion S_{z_o} of the surface S on or above the plane $z=z_o\,(Z_o > 0)$. If z_o is sufficiently small, it follows from Equation 6.8 that the plane $z=z_o$ intersects *S* in the planar curve

$$C_{z_o}: x=\left(\frac{z_o}{\alpha}\right)^{1/q}\cos\theta,\ y=\left(\frac{z_o}{\alpha}\right)^{1/q}\sin\theta,\ z=z_o \qquad (0\leq\theta\leq 2\pi) \qquad (6.9)$$

Note that we have chosen the orientation of C_{Z_o} to be consistent with the orientation of S_{Z_o}. From Equation 6.8 we compute that the unit outward normal to S in a small neighborhood of C_{Z_o} is

$$\hat{\mathbf{n}} = \left[x^2 + y^2 + \frac{1}{q^2 \alpha^{4/q}} z^{\frac{2(2-q)}{q}} \right]^{-1/2} \left(x\hat{\mathbf{i}} + y\hat{\mathbf{j}} - \frac{1}{q\alpha^{2/q}} z^{\frac{(2-q)}{q}} \hat{\mathbf{k}} \right) \tag{6.10}$$

now from Stokes theorem, Equations 6.7, 6.9 and 6.10, we compute that

$$\int_{S_{Z_o}} H\,\hat{n}\,dA = \int_{S_{Z_o}} \overline{\mathbf{w}} = \int_{C_{Z_o}} \overline{\mathbf{h}} = -\int_{C_{Z_o}} \hat{\mathbf{n}} \times d\overline{\mathbf{X}} \tag{6.11}$$

$$= \left(\frac{z_o}{a}\right)^{-1/q} \left[1 + \frac{1}{q^2 a^{2/q}} z_o^{\frac{2(1-q)}{q}} \right]^{-1/2} \int_0^{2p} \left\{ -\frac{2}{qa^{3/q}} z_o^{\frac{3-q}{q}} \cos q\,\hat{\mathbf{i}} - \frac{2}{qa^{3/q}} z_o^{\frac{3-q}{q}} \sin q\,\hat{\mathbf{j}} - \left(\frac{z_o}{a}\right)^{2/q} \hat{\mathbf{k}} \right\} dq$$

$$= -2\pi \left(\frac{z_o}{\alpha}\right)^{1/q} \left[1 + \frac{1}{q^2 \alpha^{2/q}} z_o^{\frac{2(1-q)}{q}} \right]^{-1/2} \to 0 \qquad \text{as } z_o \downarrow 0$$

accordingly Equation 6.6 also holds for a bubble having a cone or cusp point singularity on its trailing-edge.

6.6.3 Chisel Type Singularity

In this section we consider a bubble whose surface S has a whole line segment of singular points (chisel edge) on its trailing-edge as shown in Figure 6.22.

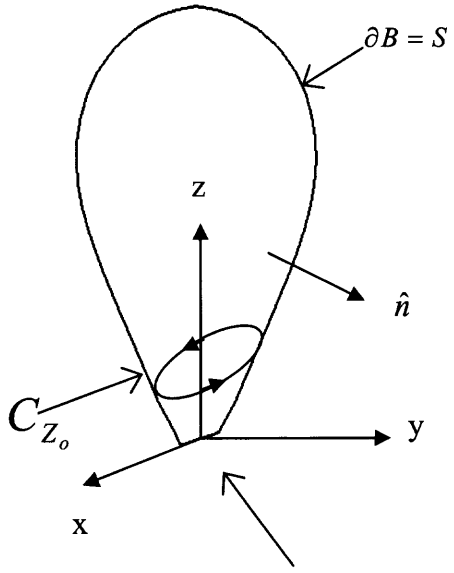

Figure 6.22 Chisel edge along x-axis

For sufficiently small z (> 0), such a chisel-edge can be represented as follows:

$$\left(\frac{x}{a+\beta z^{1/q}}\right)^2+\left(\frac{y}{\beta z^{1/q}}\right)^2=1, \tag{6.12}$$

where $\beta > 0$ and $0 < q \le 1$ is as in Equation 6.8. If $z_o > 0$ is small enough, it follows from Equation 6.12 that the plane $z = z_o$ intersects in the ellipse

$$C_{z_o}: x=\left(a+\beta z_o^{1/q}\right)\cos\theta, y=\beta z_o^{1/q}\sin\theta, z=z_o \qquad (0\le\theta\le 2\pi), \tag{6.13}$$

which has an orientation consistent with that of $S_{z_o} := SC\{(x,y,z): z^3 z_o\}$. Observe that when $z_o \downarrow 0$, the ellipse degenerates into a line segment $|x| \le a$ on the x-axis coinciding with the singular chisel-edge on the bubble surface. From Equation 6.12 we calculate the outward unit normal to S in a small neighborhood of the curve C_{z_o} to be

$$\mathbf{n}=\left\{\frac{x^2}{(a+\beta z^{1/q})^4}+\frac{y^2}{(\beta z^{1/q})^4}+\frac{\beta^2}{q^2}z^{\frac{2(1-q)}{q}}\left[\frac{x^2}{(a+\beta z^{1/q})^3}+\frac{y^2}{(\beta z^{1/q})^3}\right]^2\right\}^{-1/2}$$
$$\left\{\left(\frac{x}{(a+\beta z^{1/q})^2}\right)\hat{\mathbf{i}}+\left(\frac{y}{(\beta z^{1/q})^2}\right)\hat{\mathbf{j}}+\left(\frac{\beta}{q}z^{\frac{(1-q)}{q}}\left[\frac{x^2}{(a+\beta z^{1/q})^3}+\frac{y^2}{(\beta z^{1/q})^3}\right]\right)\hat{\mathbf{k}}\right\} \qquad (6.14)$$

Now, using Equations 6.12 – 6.14 and Stokes theorem, we readily compute that for small $z_o>0$, we have

$$\Phi(z_o):=\int_{S_{z_o}} H\hat{\mathbf{n}}\,dA=\int_{S_{z_o}}\bar{\omega}=\int_{C_{z_o}}\bar{\eta}=-\int_{C_{z_o}}\hat{\mathbf{n}}\times d\bar{\mathbf{X}}$$

$$=\left\{\frac{\cos^2\theta}{(a+\beta z_o^{1/q})^2}+\frac{\sin^2\theta}{(\beta z_o^{1/q})}+\frac{\beta^2}{q^2}z_o^{\frac{2(1-q)}{q}}\left[\frac{\cos^2\theta}{(a+\beta z_o^{1/q})}+\frac{\sin^2\theta}{(\beta z_o^{1/q})}\right]^2\right\}^{-1/2}$$
$$\int_0^{2\pi}\left\{-\frac{\beta}{q}z_o^{\frac{1-q}{q}}\left[\left(\frac{\beta z_o^{1/q}}{a+\beta z_o^{1/q}}\cos^3\theta+\sin^2\theta\cos\theta\right)\hat{\mathbf{i}}+\left(\cos^2\theta\sin\theta+\frac{a+\beta z_o^{1/q}}{\beta z_o^{1/q}}\sin^3\theta\right)\hat{\mathbf{j}}\right]-\right.$$
$$\left.\left[\left(\frac{a+\beta z_o^{1/q}}{\beta z_o^{1/q}}\right)\sin^2\theta+\left(\frac{\beta z_o^{1/q}}{a+\beta z_o^{1/q}}\right)\cos^2\theta\right]\hat{\mathbf{k}}\right\}d\theta \qquad (6.15)$$

We shall calculate $\lim_{z_o\to 0}\Phi(z_o)$ for two cases (i) $0<q<1$ and (ii) $q=1$. In case (i), it is straightforward to show that

$$\lim_{z_o\downarrow 0}\Phi(z_o)=-4a\hat{\mathbf{k}} \qquad (0<q<1) \qquad (6.16)$$

For $q=1$, calculating the limit is a bit more complicated, but it is still routing. We shall sketch the computation. If we intersect the bubble near $z=0$ with the plane $x=0$, we find from Equation 6.12.

$$\left(\frac{y}{\beta z}\right)^2=1 \quad\Rightarrow\quad y=\pm\beta z,$$

and therefore conclude that the chisel-edge is the edge of a symmetric wedge with sides defined by equations $y \pm \beta z = 0$ in R^3. Observe that the normal for the sides of the wedge are $(1+\beta^2)^{-1/2}(\hat{\mathbf{j}} - \beta\hat{\mathbf{k}})$ for $y - \beta z = 0$ and $(1+\beta^2)^{-1/2}(-\hat{\mathbf{j}} - \beta\hat{\mathbf{k}})$ for $y + \beta z = 0$. Observe that when $0 < q < 1$, the limiting normal directions are $\hat{\mathbf{j}}$ and $-\hat{\mathbf{j}}$ respectively. Consequently, in case (ii), we obtain

$$\lim_{z_o \downarrow 0} \Phi(z_o) = -\frac{4a}{\sqrt{1+\beta^2}}\hat{\mathbf{k}} \qquad (q = 1) \tag{6.17}$$

In either of the above two cases, we see that there is an unbalanced force on the singular bubble due to surface tension, which must be balances according to Newton's third law by an additional upward force on the bubble given by

$$\bar{\mathbf{F}}_+ = \begin{cases} 8\gamma a\hat{\mathbf{k}} & 0<q<1 \\ \dfrac{8\gamma a}{\sqrt{1+\beta^2}}\hat{\mathbf{k}} & q=1 \end{cases} \tag{6.18}$$

Therefore, the development of a chisel-edge singularity on the trailing-edge of the bubble should be accompanied by an increase in the upward force on the bubble that is proportional to the width of the singular edge.

CONCLUSIONS

In this thesis, the direct numerical simulation (DNS) approach is used to study two free surface problems. In the first problem, the role of viscoelasticity in deformation of neutrally buoyant drops subjected to simple shear flows is investigated, and in the second problem, the shape and the rise velocity of bubbles rising in viscoelastic fluids is analyzed.

Our results for the first problem, where the deformation of neutrally buoyant Newtonian drops in viscoelastic simple shear flows and viscoelastic drops in Newtonian simple shear flows is analyzed, indicate that the viscoelastic stresses near the principal axis of the deformed drop are extensional and near the equator they are tangential. Thus, viscoelastic stresses reduce drop deformation when the drop phase is viscoelastic and increase deformation when the matrix phase is viscoelastic. Additionally, when the outside fluid is viscoelastic, the drop develops pointed ends due to the extensional nature of viscoelastic stresses while in Newtonian fluids the ends are rounded.

In the second problem, simulations are used to study the following key issues for Newtonian bubbles rising due to buoyancy in viscoelastic fluids: the transient changes in bubble shape and velocity, and their role in the sharp increase in terminal velocity at a critical volume, the presence of negative wake and recirculation zones, and the asymmetry in the shape of a deformed bubble. These analysis were carried out as a function of the polymer concentration parameter c, relaxation time λ_r, and the bubble radius a, keeping other factors such as the interfacial tension, density ratio, viscosity ratio and the zero shear viscosity constant.

The DNS results indicate that the bubble accelerates rather quickly from rest, but start to decelerate once the elastic stresses develop. For a fixed value of λ_r and sufficiently small bubble volume, the bubble attains a steady shape and a constant rise velocity. This is however not the case for the larger sized bubbles, at least for the finite sized computational domains used here as the bubbles reached the top before reaching a steady state shape or velocity. Simulations also show that the viscoelastic stresses near the trailing end of the bubble are significant, and when the bubble volume is larger than a critical volume they cause the trailing end of the bubble to be pulled out. Results indicate that after the trailing end is pulled out the velocity of the bubble increases.

When terminal velocity is plotted as a function of the bubble volume, a steep increase in terminal velocity was observed over a very small range of volume. The increase in the rise velocity is more pronounced when c is larger.

The flow pattern in the wake of the bubble was analyzed and the presence of two recirculation zone in the wake of the bubble and their positions were found to depend on the parameter values. Upon increasing the relaxation time of the fluid, the recirculation zones moved closer to the axis of the bubble and closer to the trailing edge, and the bubble has a more pronounced tail compared to the shape of a bubble rising in a viscoelastic fluid with a smaller relaxation time.

REFERENCES

A. Acrivos and T. A. Lo, Deformation and breakup of a single slender drop in extensional flow, *J. Fluid Mech.*, **86**, 641 (1978).

M. T. Arigo and G. H. McKinley, An experimental investigation of negative wakes behind spheres settling in a shear-thinning viscoelastic fluid, *Rheol. Acta*, **37**(4), 307-327 (1998).

G. Astarita and G. Apuzzo, Motion of gas bubbles in Non-Newtonian liquids, *A.I.Ch.E. Journal*, **11 (5)**; 815-820 (1965).

S. M. Barnett, A. E. Humphrey and M. Litt, Bubble motion and mass transfer in non-Newtonian fluid, *A.I.Ch.E. Journal*, **Vol. 12(2)**; 253-259 (1966).

D. Barthes-Biesel, A. Acrivos, Deformation and burst of a liquid droplet freely suspended in a linear shear field, *J. Fluid Mech.*, **61**, 21 (1973a).

A. Belmonte, Self oscillations of a cusped bubble rising through a micellar solution, *Rheol. Acta*, **39**; 554-559 (2000).

R. B. Bird, R. C. Armstrong, O. Hassager, Dynamics of polymeric fluids Vol. 1, Sec. Ed., John Wiley and Sons (1987).

C. Bisgaard, Velocity fields around spheres and bubbles investigated by laser-Doppler anemometry, *J. Non-Newtonian Fluid Mech.*, **12**; 283-302 (1983).

D. Blackmore and L. Ting, Surface integral of its mean curvature vector, *SIAM Review*, **27-4**, (1985).

D. W. Bousfield, R. Keunings and M. M. Denn, Transient deformation of an inviscid inclusion in a viscoelastic extensional flow, *J. Non-Newtonian Fluid Mech.*, **27**, 205 (1988).

J. U. Brackbill, D. B. Kothe and C. Zemach, A continuum method for modeling surface tension, *J. Comput. Phys.*, **100**, 335 (1992).

M. O. Bristeau, R. Glowinski and J. Periaux, Numerical methods for Navier-Stokes equations. Application to the simulation of compressible and incompressible flows, *Computer Physics Reports* **6**, 73 (1987).

P. H. Calderbank, D. S. Johnson, J. Loudon, Velocity fields around spheres and bubbles investigated by laser-doppler anemometry, *Chem. Eng. Sci.*, **25**, 235 (1970).

Y. C. Chang, T. Y. Hou, B. Merriman, and S. Osher, A level set formulation of Eulerian interface capturing methods for incompressible fluid flows, *J. Comput. Phys.*, **124**, 449 (1996).

M. D. Chilcott, and J. M. Rallison, Creeping flow past dilute polymer solutions past cylinders and spheres, *J. Non-Newtonian Fluid Mech.*, **29**, 381 (1988).

R. A. De Bruijn, Ph.D. thesis, Deformation and break up of drops in simple shear flows, Eindhoven University Of Technology, Eindhoven, The Netherlands (1989).

R. A. De Bruijn, Tip Streaming of drops in simple shear flows, *Engineering Sci.*, **48(2)**, 227 (1993).

J. J. Elmendorp and R. J. Maalcke, A study on polymer blending micro rheology: Part 1, *Polym. Eng. Sci.*, **25**, 1041 (1985).

E. Fatemi and F. Odeh, Upwind finite difference solution of Boltzmann equation applied to electron transport in semiconductor devices, *J. Comput. Phys.*, **108**, 209 (1993).

R. W. Flumerfelt, Drop breakup in simple shear fields of viscoelastic fluids, *Ind. Eng. Chem. Fundam.*, **11**, 312 (1972).

D. Funfschilling and H. Z. Li, Flow of Non-Newtonian fluids around bubbles: PIV measurements and birefringence visualization, *Chem. Eng. Sci.*, **56**; 1137-1141 (2001).

G. H. McKinley, *Transport Processes in bubbles, drops and particles*, edited by R. P. Chhabra and D. DeKee, 2nd edition, Taylor Francis, London (2001).

R. Glowinski, P. Tallec, M. Ravachol and V. Tsikkinis, Chap. 7 in Finite Elements in Fluids, Vol 8, Ed. T.J. Chung, Hemisphere Publishing Corp., Washington DC (1992).

R. Glowinski and O. Pironneau, Finite element methods for Navier-Stokes equations, *Annu. Rev. Fluid Mech.*, **24**, 167 (1992).

R. Glowinski, T.W. Pan, T.I. Hesla and D.D. Joseph, A distributed Lagrange multiplier/fictitious domain method for particulate flows, *Int. J. Multiphase Flows* **25(5)**, 755 (1999).

H. P. Grace, Dispersion phenomeneon in high viscosity immiscible fluid systems and the application of static mixers as dispersion devices in such systems, *Eng. Found., Res. Conf. Mixing. 3rd, Andover, N.H.* (1971), Republished in *Chem Eng. Commum.*, Vol. **14**, 225 (1982).

S. Guido and M. Villone, Three dimensional shape of a drop under simple shear flow, *J. Rheol*, **42**, 395 (1998).

N. Z. Handzy, A. Belmonte, Oscillatory rise of bubbles in wormlike micellar fluids with different microstructures, *Physical Review Letters*, **92(12)**, 124501-1 (2004).

O. Hassager, Negative wake behind bubbles in non-Newtonian liquids, *Nature,* **Vol. 279**, 402 (1979).

E. J. Hinch and A. Acrivos, Steady long slender droplets in two-dimensional straining motion, *J. Fluid Mech.*, **91**, 401 (1979).

J. R. Hererra-Velarge, R. Zenit, D Chehata, B. Mena, The flow of non-Newtonian fluids around bubbles and its connection to the jump discontinuity, *J. Non-Newtonian Fluid Mech.*, **111,** 199 (2003).

E. J. Hinch and A. Acrivos, Long slender drops in simple shear flow, *J. Fluid Mech.*, **98**, 305 (1980).

C.W. Hirt and B.D. Nichols, Volume of fluid (VOF) methods for the dynamics of free boundaries, *J. Comput. Phys.*, **39**, 201 (1981).

A. Jayaraman and A. Belmonte, Oscillations of a solid sphere falling through a wormlike micellar fluid, *Phys. Rev. E* **67**, 65301 (2003).

D. D. Joseph and J. Feng, Negative wake in second-order fluid, *J. Non-Newtonian Fluid Mech.*, **57**, 313 (1995).

M. J. King and N. D. Walters The unsteady motion of a sphere in an elastico-viscous liquid, *J. Phys. D: Appl. Phys.*, **5,** 141 (1972).

R. C. King, R. C. Apelian, R. C. Armstrong and R. A. Brown, Numerically stable finite element techniques for viscoelastic calculations in smooth and singular geometries, *J. Non-Newtonian Fluid Mech.*, **29**, 147 (1988).

S. Kwak and C. Pozrikidis, Adaptive triangulation of evolving, closed or open surfaces by advancing-front method, *J. Comput. Phys.*, **145(1)**, 61 (1998).

L. G. Leal, Laminar flow and convective transport process, Butterworth-Heinemann (1992).

L. G. Leal, J. Skoog and A. Acrivos, On the motion of gas bubbles in a viscoelastic fluid, *The Can. J. Chem. Eng.*, **49**, 569-575 (1971).

L. Levitt and C. W. Macosko, Influence on Normal stress difference on polymer drop deformation, *Polym. Eng. Sci.*, **36 (12)**, 1647 (1996).

Y. J. Liu, T. Y. Liao and D. D. Joseph, A two-dimensional cusp at the trailing edge of an air bubble rising in a viscoelastic liquid, *J. Fluid Mech.*, **304,** 321 (1995).

J. Li, M. Renardy, Y. Y. Renandy and M. Renardy, Numerical simulation of breakup of a viscous drop in simple shear flow through a volume-of-fluid method, *Physics of Fluids*, **12(2)**, 59 (2000).

Y. Liao and J. B. McLaughlin, Bubble velocity profile and model of surfactant mass transfer to bubble surface, *Chem. Eng. Sci.*, **55(23)**, 5831 (2000).

J. M. Marchal and M. J. Crochet, Hermitian finite elements for calculating viscoelastic flows, *J. Non-Newtonian Fluid Mech.*, **20**, 187 (1986).

J. M. Marchal and M. J. Crochet, A new mixed finite element for calculating viscoelastic flow, *J. Non-Newtonian Fluid Mech.*, **26**, 77 (1987).

G. I. Marchuk, Splitting and alternate direction methods. In P. G. Ciarlet and J. L. Lions (Eds.), *Handbook of Numerical Analysis*, **Volume I**, 197-462. Amsterdam: North-Holland (1990).

F. Mighri and P. J. Carreau, Influence of elastic properties on drop deformation and breakup in shear flow, *J. Rheol.*, **42(6)**, 1477 (1998).

M. Wu and M. Gharib, Experimental studies on the shape and path of small air bubbles rising in clean water, *Physics of Fluids* **14(7),** L49 (2002).

D. S. Noh, I. S. Kang, and L. G. Leal, Numerical solutions for the deformation of a bubble rising in a dilute polymeric fluids, *Physics of Fluids* **5(6)**, 1315 (1993).

J. G. Oldroyd, Non-Newtonian effects in steady motion of some idealized elastico-viscous liquids, *Proc. R. Soc.* **A245**, 278 (1958).

S. Osher and J. A. Sethian, Fronts propagating with curvature-dependent speed: Algorithms based on Hamilton-Jacobi formulations, *J. Comput. Phys.*, **83**, 12 (1988).

S. B. Pillapakkam and P. Singh, A level set method for computing solutions to viscoelastic two-phase flow, *J. Comput. Phy.*, **174(2),** 552 (2001).

J. M. Rallison, The deformation of small viscous drops and bubbles in shear flows, *Ann. Rev. Fluid. Mech.,* **16**, 45 (1984).

S. Ramaswamy and L. G. Leal, The deformation of a viscoelastic drop subjected to steady uniaxial extensional flow of a Newtonian fluid, *J. Non-Newtonian Fluid Mech.*, **85**, 127 (1999).

S. Ramaswamy and L. G. Leal, The deformation of a Newtonian drop in the uniaxial extensional flow of a viscoelastic liquid, *J. Non-Newtonian Fluid Mech.*, **88**, 149 (1999).

M. Reiner, The Deborah Number, *Phys. Today*, **17**, 62 (1964).

D. Rodrigue, R. P. Chhabra, C. F. Chan Man Fong, An experimental study of the effect of surfactants on the free rise velocity of gas bubbles, *J. Non-Newtonian Fluid Mech.*, **66**, 213 (1996).

D. Rodrigue, R. P. Chhabra and C. F. Chan Man Fong, Bubble velocities: further developments on the jump and discontinuity, *J. Non-Newtonian Fluid Mech.*, **79**, 45 (1998).

F. D. Rumscheidt and S. G. Mason, Particle motions in sheared suspensions, *J. Colloid Sci.*, **16**, 238 (1961).

G. Ryskin and L. G. Leal, Numerical solution of free-boundary problems in fluid mechanics. Part 1. The finite-difference technique, *J. Fluid Mech.*, **148**, 1 (1984).

P. Singh and L. G. Leal, Finite element simulation of the start-up problem for a viscoelastic fluid in an eccentric rotating cylinder geometry using a third-order accurate upwind scheme, *Theor. Comput. Fluid Mech.*, **5**, 107 (1993).

P. Singh, D .D. Joseph, T. I. Hesla, R. Glowinski and T. W. Pan, A distributed Lagrange multiplier/fictitious domain method for viscoelastic particulate flows, *J. Non-Newtonian Fluid Mech.*, **91**, 165 (2000).

H. A. Stone, Dynamics of drop deformation and breakup in viscous fluids, *Ann. Rev. Fluid. Mech.*, **26**, 65 (1994).

M. Sussman, E. Fatemi, P. Smereka and S. Osher, An improved level set method for incompressible two-phase flows, *Computers and fluids*, **27**, 663 (1998).

M. Sussman, P. Smereka and S. Osher, A level set approach for computing solutions to incompressible two-phase flow, *J. comput. Phys.*, **114**, 146 (1994).

M. Sussman and P. Smereka, Axisymmetric free boundary problems, *J. Fluid Mech.*, **341**, 269 (1997).

A. J. Szeri, S. Wiggins, L. G. Leal, On the dynamics of suspended microstructure in unsteady, spatially inhomogeneous, two-dimensional fluid flows, *J. Fluid Mech.*, **228,** 207 (1991).

G. I. Taylor, The formation of emulsions in definable fields of flow, *Proc. R. Soc. Lond.* A **146**, 501 (1934).

G. I. Taylor, Conical free surfaces and fluid interfaces, *Proc. 11th Int. Cong. Appl. Mech.*, Munich (1964).

T. Tavgac, Ph.D. thesis, Drop deformation and break up in simple shear fields, (Chemical Engineering) Univ. of Houston, Houston, Texas (1972).

G. Tiefenbruck, and L.G. Leal, A numerical study of the motion of a viscoelastic fluid past rigid spheres and spherical bubbles, *J. Non-Newtonian Fluid Mech.*, **10**, 115 (1982).

V. T. Tsakalos, P. Navard, E. Peuvrel-Disdier, Deformation and breakup mechanisms of single drops during shear, *J. Rheol.*, **42(6)**, 1403 (1998).

S. O. Unverdi and G. Tryggvason, A front-tracking method for viscous, incompressible, multi-fluid flows, *J. Comput. Phys.*, **100**, 25 (1992).

P. P. Varanasi, M. E. Ryan, P. Stroeve, Experimental study on the break up of Model Viscoelastic drops in uniform shear flow, *Ind. Eng. Chem. Res.*, **33**, 1858 (1994).

A. J. Wagner, L. Giraud, and C. E. Scott, Simulations of a cusped bubble rising in a viscoelastic fluid with a new numerical method, *Comp. Phys. Comm.*, **129**, 227 (2000).

B. Yang, A. Prosperetti, and S. Takagi, The transient rise of a bubble subject to shape or volume changes, *Phys. Fluids*, **15(9),** 2640 (2003).

R. Zheng and N. Pan-Thien , A boundary element simulation of the unsteady motion of a sphere in a cylindrical tube containing a viscoelastic fluid. Rheol. Acta, **3**, 323 (1992).